EFFECT OF A LOCALIZED VELOCITY INCREASE ON OVERALL POWER CONSUMPTION AND FLOW CHARACTERISTICS IN PNEUMATIC CONVEYING SYSTEMS

A Thesis Submitted to
the College of Graduate and Postdoctoral Studies
In Partial Fulfillment of the Requirements
For the Degree of Master of Science
In the Department of Chemical and Biological Engineering
University of Saskatchewan
Saskatoon, Saskatchewan

By
Tyrone Randal Keep

PERMISSION TO USE

In presenting this thesis/dissertation in partial fulfillment of the requirements for a Postgraduate degree from the University of Saskatchewan, I agree that the Libraries of this University may make it freely available for inspection. I further agree that permission for copying of this thesis/dissertation in any manner, in whole or in part, for scholarly purposes may be granted by the professor or professors who supervised my thesis/dissertation work or, in their absence, by the Head of the Department or the Dean of the College in which my thesis work was done. It is understood that any copying or publication or use of this thesis/dissertation or parts thereof for financial gain shall not be allowed without my written permission. It is also understood that due recognition shall be given to me and to the University of Saskatchewan in any scholarly use which may be made of any material in my thesis/dissertation. Reference in this thesis/dissertation to any specific commercial products, process, or service by trade name, trademark, manufacturer, or otherwise, does not constitute or imply its endorsement, recommendation, or favouring by the University of Saskatchewan. The views and opinions of the author expressed herein do not state or reflect those of the University of Saskatchewan, and shall not be used for advertising or product endorsement purposes.

Requests for permission to copy or to make other use of material in this thesis in whole or part should be addressed to:

Head of the Department of Chemical and Biological Engineering

University of Saskatchewan

57 Campus Drive

Saskatoon, Saskatchewan, Canada

S7N 5A9

ABSTRACT

Pneumatic conveying is widely used in the agricultural industry for seed and fertilizer conveying during seeding operations. Dilute phase conveying is used as it inherently has a disperse particle flow that is leveraged to promote uniform division of the flow. Due to the higher power required per unit mass for dilute phase conveying, research was undertaken to better understand the role of entrainment and conveying velocity on the particles' behavior, entrainment level, and the power required to convey them.

The two hypotheses that guided this thesis were that an increased velocity in the entrainment zone, relative to the downstream conveying zone would (1) increase the entrainment level of the product and (2) decrease overall power required for conveying.

To test these hypotheses, the following were completed:

- A non-invasive method to quantify the entrainment level of the particles was developed;
- A lab-scale pneumatic conveying system was designed and built that allowed for testing the effect of independently varying the entrainment and conveying velocities;
- These systems were used to explore product entrainment levels in the form of a probability distribution map of the products location in the conveying pipe; and
- The relationship of entrainment velocity and conveying velocity on the pressure drop and energy required to convey was explored.

An optical flow profiling imaging apparatus was designed and built that allowed for non-invasive imaging of the product flow behavior. A laser was used to illuminate a cross-section of the conveying line. Successive images of this illuminated section were acquired and then processed to give a probability distribution map of the particles' location within the pipe. The centroid of this distribution was used as a proxy for the entrainment level of the product within the pipeline.

To enable conveying at two different velocities in a single system, a gas extraction system was designed and constructed. This system allowed for a higher velocity during product entrainment and after a certain distance downstream air volume is bled off which in turn lowers the conveying velocity. This system was used in conjunction with the flow profiler to give a quantitative measure of the effect of gas extraction on the entrainment level of the product as defined by the centroid of the probability distribution map. The profiles taken indicated that the entrainment velocity had a significant effect on the entrainment level of the product in the downstream section.

In addition to the entrainment level of the product, velocity and pressure data were acquired to explore the energy needed to convey varying mass flow rates. Specific pressure drop (ratio of air and product pressure drop to the air only pressure drop) was plotted against the mass loading ratio (ratio of the mass flow rate of the solid to the mass flow rate of the fluid) and grouped by the velocity ratio (conveying velocity over the entrainment velocity). When the velocity ratio was one the slope was positive with an intercept of approximately one. The data agreed with previously published results. As the velocity ratio was lowered the slope was reduced as well. At velocity ratios of 0.6-0.7 the slope of the relationship was approximately zero. This indicated that entraining at the higher velocity and then conveying at a lower velocity at this ratio required no additional pressure drop for conveying compared to the air only pressure drop. In addition, the specific energy required to convey the product was calculated. At the aforementioned velocity ratios there was an 8-16% energy savings compared to conveying at the same entrainment and downstream velocity. There will be an efficiency cost to accelerating the product in the entrainment zone, however if a system could be designed such that the efficiency gains of low-speed conveying are greater than the extra energy required in the entrainment region, a net energy savings can result.

ACKNOWLEDGEMENTS

I would like to express utmost thanks to my supervisor Dr. Scott Noble. He was always available for a quick chat, project guidance, and deeper discussion. Most importantly we shared an affinity for strong and black coffee, which at least briefly clarified all things.

Funding from CNH Saskatoon is gratefully acknowledged as it enabled me to acquire a Natural Science and Engineering Research Council's (NSERC) Industrial Postgraduate Scholarship. Additionally, they facilitated equipment donations, instrument purchases, prototyping, and technical support. Mr. Jim Henry and Mr. Joel Gervais from CNH Saskatoon specifically were instrumental for their guidance and support especially in the early stages of the project.

The assistance of B. Lozinsky and S. Gregoire in the preliminary design of the optical flow profiling apparatus is gratefully acknowledged. I would like to thank the staff of Engineering Shops for the initial build of the imager and for rapid-prototyping parts on the gas extraction system. I would also like to thank Lean Machine for manufacturing the final iteration of the optical imaging apparatus.

DEDICATION

For my family and friends. You were always there for me and eventually came to understand (or at least got good at pretending) a little about what I did on a day to day basis.

TABLE OF CONTENTS

LIST OF TABLES

LIST OF APPENDIX TABLES

LIST OF FIGURES

LIST OF APPENDIX FIGURES

NOMENCLATURE

ENGLISH SYMBOLS

Symbol	Description	Unit
A^*	Projected area normal to flow	[m^2]
C	Sutherland's constant	-
C_D	Drag Coefficient	-
C_T	Turbulent drag factor	-
CP	Coordinates of the centre pixel of the image	-
$C.o.M.$	Centre of mass of the particle probability distribution	[mm]
c	Average particle velocity	[m/s]
c_{ls}	Saffman lift coefficient	-
D	Pipe inner diameter	[m]
D_T	Rate of deformation tensor	
$E_{specific}$	Specific energy	[J/kg m]
d	Particle diameter	[m]
d_a	Arithmetic mean particle diameter	[m]
d_g	Geometric mean particle diameter	[m]
F_D	Drag force on a particle	[N]
I	Test image	-
i	Horizontal pixel location	-
j	Vertical pixel location	-
K	Slope of the linear relationship between α and ϕ	-
L	Pipe length	[m]
l_{max}	Particle maximum length	[m]
l_{int}	Particle intermediate length	[m]
l_{min}	Particle minimum length	[m]
$\dot{m}_f$	Mass flow rate of the fluid	[kg/s]
$\dot{m}_g$	Mass flow rate of the gas (air)	[kg/s]
$\dot{m}_p$	Mass flow rate of the particles/solid	[kg/s]
m	Image width	[pixels]

N	Number of test images	-
n	Image height	[pixels]
p_d	Pressure of dry air	[Pa]
Δp	Pressure drop	[Pa]
Δp_g	Pressure drop of the gas phase	[Pa]
Δp_{s+g}	Pressure drop of the solid and gas phases	[Pa]
PDM	Particle occurrence probability density map	-
p_v	Pressure of water vapour	[Pa]
R	Reference image	-
R_d	Specific gas constant for dry air, 287.058 J/kgK	[J/kgK]
Re	Reynolds number	-
Re_p	Reynolds number of the particle	-
R_v	Specific gas constant for water vapour, 461.495 J/kgK	[J/kgK]
S	Air resistance coefficient across an object's surface	-
T	Temperature	[K]
T_0	Reference Temperature	[K]
u_g	Gas velocity	[m/s]
u_p	Particle velocity	[m/s]
u_r	Relative fluid velocity	[m/s]
u_s	Superficial fluid velocity	[m/s]
V	Pipe volume	[m^3]
$\dot{V}$	Volumetric flow rate	[m^3/s]
v	Fluid velocity	[m/s]
v_e	Gas velocity between particles	[m/s]
V_s	Enclosed solids volume	[m^3]
w_s	Slip Velocity (Relative velocity between the gas and solid)	[m/s]
x_{max}	Maximum x coordinate of conveying line in the image	-
x_{min}	Minimum x coordinate of conveying line in the image	-
y_{max}	Maximum y coordinate of conveying line in the image	-
y_{min}	Minimum y coordinate of conveying line in the image	-

GREEK SYMBOLS

Symbol	Description	Unit
α	Specific pressure drop	-
δ	Ratio of upstream to downstream velocity	-
ε	Void ratio	-
ρ	Fluid density	[kg/m^3]
ρ^*	Apparent bulk density	[kg/m^3]
ρ_{humid}	Density of humid air	[kg/m^3]
ρ_p	Particle density	[kg/m^3]
λ_L	Darcy pipe friction factor	-
μ	Dynamic viscosity	[Pa s]
μ_0	Reference viscosity	[Pa s]
ϕ	Mass loading ratio $\frac{\dot{m}_p}{\dot{m}_f}$	-
ω_r	Angular velocity of the particle	[rad/s]
ψ	Sphericity of a particle	-

CHAPTER 1: INTRODUCTION

Agricultural producers in Western Canada use pneumatic conveying systems to transport seed and fertilizer from one or more large mobile tanks (the air cart) to the seeding implement (air hoe drill). A Case New Holland (CNH) air seeding system is shown in Figure 1.1. Variations of pneumatic conveying methods are used by all major manufacturers of seeding systems. The product is incorporated into many separate airstreams created by one or more fans (used as a single source) mounted on the air cart. These primary air lines carry seed and granular fertilizer to the seeding implement. The air and product are then separated into secondary runs that deposit seed into individual rows. The pneumatic system is operated in the dilute phase of solid-gas flow to facilitate seed separation at the seeding implement. Dilute phase flow is defined as a flow regime that uses a large volume of gas at high velocity (above the saltation velocity) to convey discrete particles (Klinzing, Rizk et al. 2010).

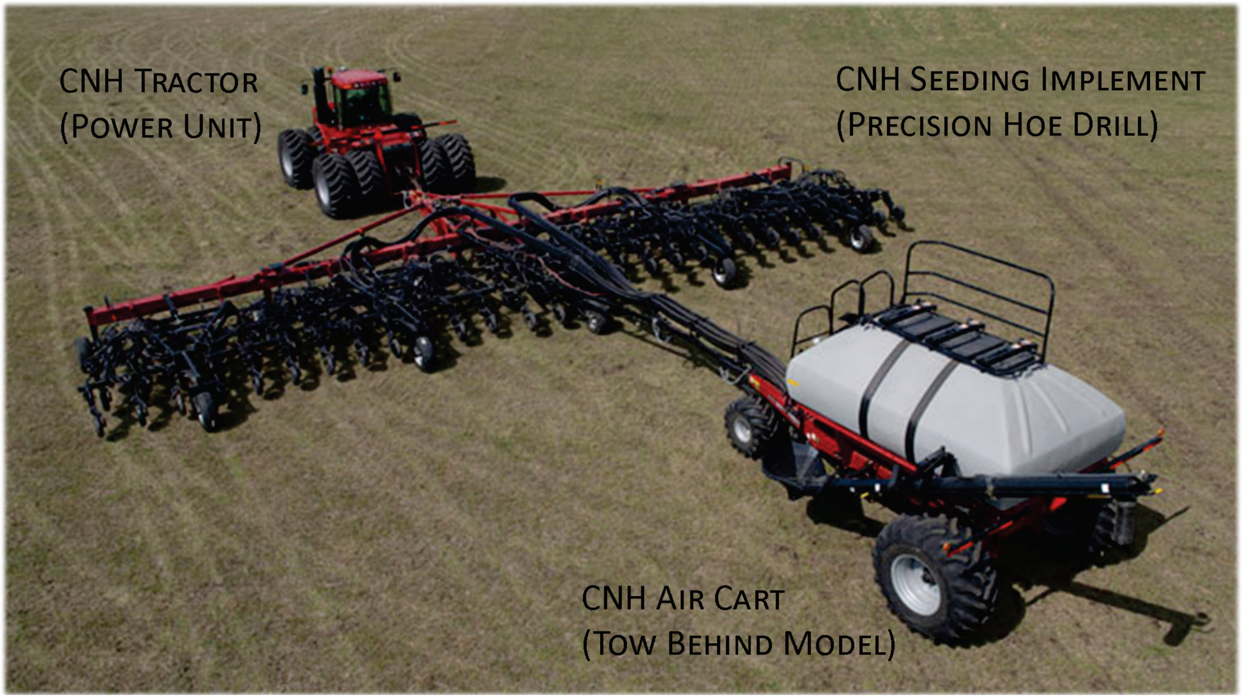

Figure 1.1: CNH seeding implement with tractor, Precision Hoe Drill, and air-cart. Adapted from Case IH 2012 with permission. (Case IH 2012)

Dilute phase flow is widely used for agricultural pneumatic conveying but it has disadvantages when compared to dense phase conveying, such as using more power per unit mass conveyed and the greater tendency to cause pipe wear and seed damage (Barbosa and Seleghim Jr. 2003).

Conveying power required is directly related to the velocity cubed, while pipe wear and seed damage are also exponentially related to the conveying velocity (Klinzing, Rizk et al. 2010). Reducing the conveying velocity can therefore significantly reduce costs associated with equipment maintenance and operation for the end user.

As the agriculture industry, particularly in Western Canada, Australia, and Eastern Europe, shifts to larger equipment there is a need for more efficient seed delivery and air handling systems. The desired efficiency gains are driven by market demands and physical limitations with current fan designs. Any power savings that can be easily implemented into current air carts or designed into future iterations would be an advantage in the marketplace. Entrainment systems or methods that allow for power reduction and/or reduced product velocity are desirable. Lowering the carrying velocity has the additional benefit of reducing seed coat damage (increases germination) and minimizing fertilizer shattering (reduces dust which leads to uneven application).

1.1 RESEARCH OBJECTIVES

The overarching theme for this research was to explore the effect of entrainment and conveying velocity on the efficiency of dilute phase agricultural pneumatic conveying systems. While other industries utilize similar conveying schemes, the impetus for this work comes from the agriculture-sector and therefore agricultural materials, such as wheat, were used.

1.1.1 Hypothesis

Higher gas velocity in the entrainment zone, relative to the downstream conveying gas velocity, was proposed to have the following effects:

1) Increased entrainment level of the product and
2) Reduced overall power required for conveying by enabling a lower downstream conveying velocity.

1.1.2 Specific goals of project

The following were the specific objectives of the research:

1. Develop a method to non-invasively quantify the entrainment level of conveyed particles.
2. Design and build a lab scale pneumatic conveying system that allows the effect of independently varying entrainment velocity and conveying velocity to be tested.

3. Explore the product entrainment level at various conveying velocities and its relationship, if any, to conveying efficiency.
4. Characterize the relationship of entrainment velocity, conveying velocity, and the energy required to convey a given mass flow rate of product.

1.2 OVERVIEW OF THESIS

General background on agricultural pneumatic conveying, particle characteristics, particle entrainment, and forces on a particle will be outlined in Chapter 2. A novel method for non-invasive monitoring and quantification of the entrainment level will be discussed in Chapter 3. The design and implementation of a gas extraction velocity reduction system will be discussed in Chapter 4. Finally, the effect of gas extraction that enables different entrainment and conveying velocities on the specific pressure drop and power characteristics of wheat will be explored in Chapter 5.

CHAPTER 2: BACKGROUND AND LITERATURE REVIEW

A general overview of pneumatic conveying systems and methods along with factors affecting particle conveyance will be discussed in the following sections. A more specific background is located in each following chapter with information that pertains specifically to the information given in that chapter.

2.1 PNEUMATIC CONVEYING SYSTEMS IN AGRICULTURE

Pneumatic conveying can be described as the transportation of powders and granular materials in either a positive or negative pressure gas stream (Klinzing, Rizk et al. 2010). Pressurized gas is used to achieve work on the bulk material to be delivered from one location to another.

Positive pressure systems are used to transport particles from one common location to one or more destinations. The particles are metered from a storage tank into a fluid stream contained in some form of piping. At the destination particles are generally removed from the airstream using a cyclone, with the gas being vented to atmosphere or filtered to remove dust (Klinzing, Rizk et al. 2010). The conveying gauge pressures commonly found in pneumatic conveying are high pressure (310 kPa-891 kPa), medium pressure (103 kPa-310 kPa), and low pressure (less than 103 kPa) (Shamlou 1988).

Negative pressure pneumatic conveying is used to convey particles from multiple pickup or insertion points to a common destination. The most common use in agriculture would be grain vacuum systems used for unloading or cleaning dry bulk materials from bins, boats, trucks, or trains (Shamlou 1988).

The third major type of pneumatic conveying system is a combination of positive and negative pressure. This hybrid combines the most useful features of both systems, namely the ability to convey materials from multiple pick up points to multiple discharge or collection locations (Klinzing, Rizk et al. 2010). The negative pressure portion of the system picks up the particles which are then transferred to the positive pressure side for distribution.

2.1.1 Air Cart

The air cart is an integral component of an air seeding or planting system. It functions as a mobile granular storage tank and the central distribution point with attached metering system as shown in Figure 2.1. An air cart consists of one or more product tanks to allow for the distribution of both seed and fertilizer, known in the industry as a double shoot system.

To aid in seed and fertilizer separation in the seed row, air carts employ double shoot distribution systems. Air carts designed for granular fertilizer applications as well as seeding will have separate, parallel conveying lines to place the fertilizer at a safe distance from the seed to minimize nitrogen burning. Both single and double shoot systems will have multiple primary conveying lines that are then split using manifolds into secondary conveying lines using the single air source. This method of conveying makes system balancing difficult and generally results in a higher conveying velocity being used than actually required for distribution.

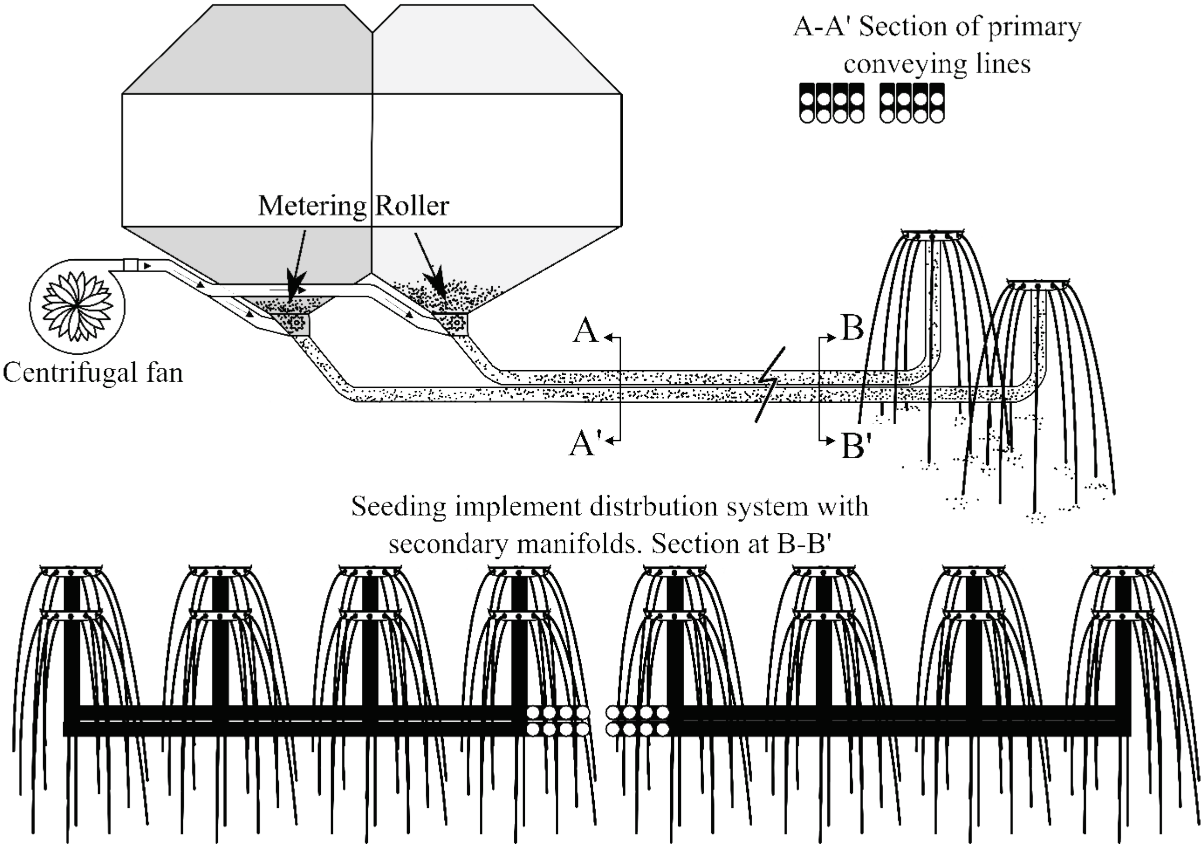

Figure 2.1: Schematic of the pneumatic distribution system for an air-seeding-cart. Adapted from Flexi-Coil 20 Series Seed Cart Operator's Manual (Flexi-Coil 1997)

Positive pressure air carts employ a centrifugal fan to provide the pneumatic system with its conveying gas. These fans provide high volume and velocity flow at low pressures. The air flow is routed down past the meter roller in Figure 2.3 in a downdraft configuration but most other manufacturers use a Venturi section to assist in product entrainment.

2.1.2 Metering Device

Product metering on an air-cart is typically accomplished through the use of an auguring system or fluted rollers which rotate to deliver the required mass flow rate into the airstream. Systems of this type are able to meter a wide range of products and mass flow rates while minimizing product damage and meter blockages (Kraus 1991).

A more detailed cross section of air-cart tank system and a cross-section of the metering box are shown in Figure 2.2 and Figure 2.3 respectively. A double-shoot tank configuration is shown with the air-flow flowing down through the meter box and accelerating the particles into the airstream.

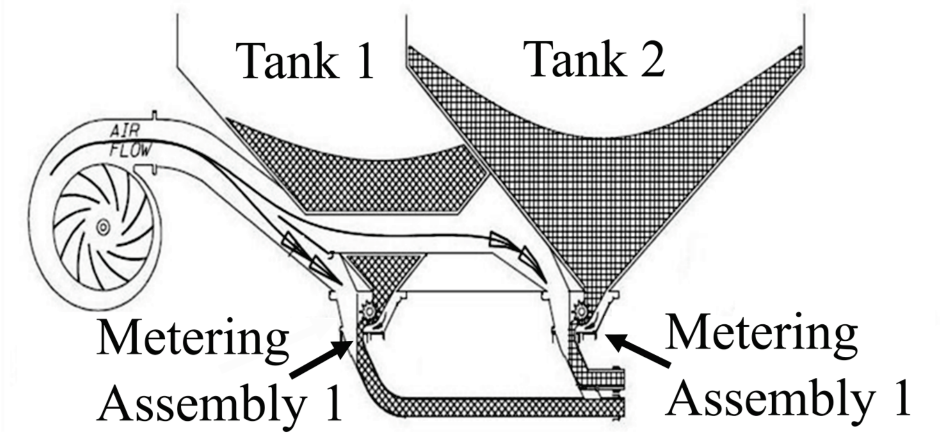

Figure 2.2: Double-shoot tank configuration. Adapted from Flexi-Coil 20 Series Seed Cart Operator's Manual (Flexi-Coil 1997)

The cross-section in Figure 2.3 shows the path of both the conveying gas and the product to be conveyed. The meter rotates clockwise to dispense product at the desired rate into the air stream. The particles are initially accelerated down until the conveying line changes direction. The particles then have to undergo another acceleration phase horizontally in the direction of travel.

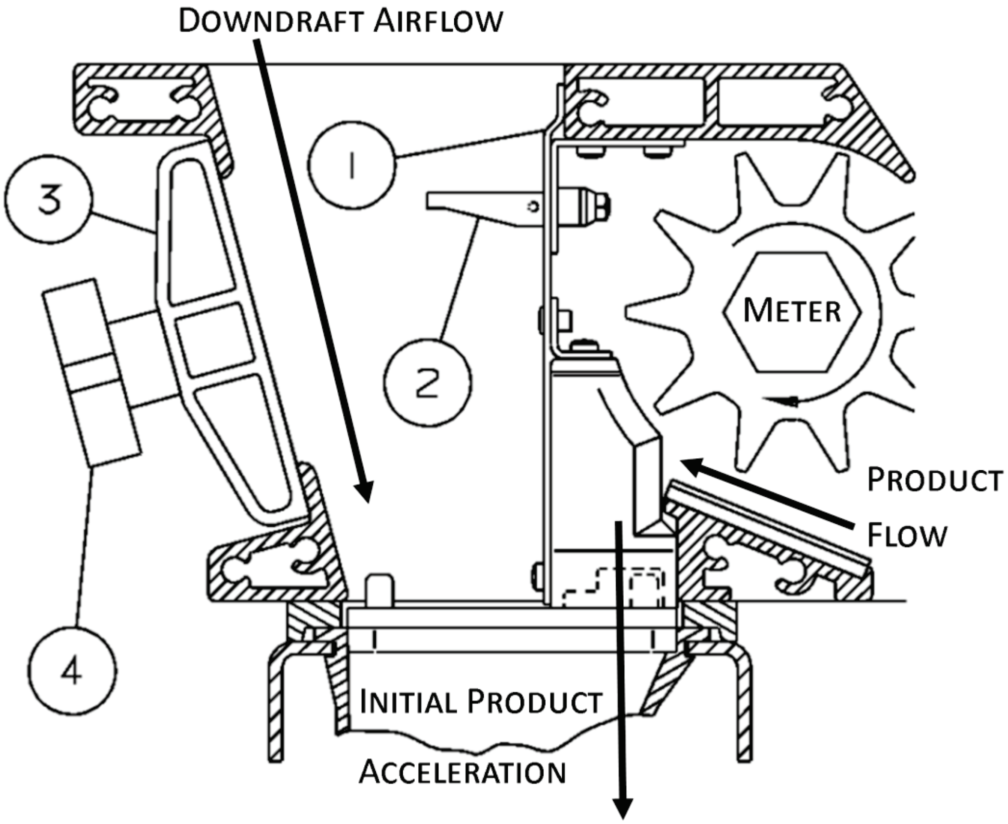

Figure 2.3: Cross-section of a CNH meter box (1. Baffle Panel 2. Retainer latch 3. Inspection cover 4. Fastener knobs). Adapted from the Flexi-Coil air-cart assembly instructions (Flexi-Coil 2011)

2.1.3 Seeding Implement

The seeding implement is the tool that physically places the seed and fertilizer into evenly spaced rows. There are many variations of implements such as: precision planters, which use a vacuum plate to precisely meter seed into downspouts; air-disc drills, which use the conventional air carts to deliver seed to the rows created by disc openers; and air hoe-drills, which also use the conventional carts with a hoe, shovel, or knife opener to create the seed rows. A typical hoe-drill shank and packer arm is shown in Figure 2.4. This arm is used on the CNH Precision Hoe Air Drill and is equipped for placing both seed and fertilizer into a single row. The parallel linkage enables a consistent depth to be maintained between the bottom of the packer wheel and the tip of the knife. This allows for a consistent seed depth and fertilizer placement across the drill in varying ground conditions and elevations.

Figure 2.4: CNH Precision Air-Hoe Drill Shank Assembly (Case IH 2012).

2.2 PARTICLE CHARACTERISTICS

Wheat will be used for all example calculations, as it has the most readily available data in the literature for the agricultural products of interest. Unless otherwise stated, the properties of wheat were collected from product that was used during testing. A few additional values were obtained from Güner (2007). These properties are shown in Table 2.1.

Table 2.1: Mean and standard errors of selected physical properties of the wheat used. Unless indicated, all values were obtained from the actual product used during testing.

Property	Wheat
Geldart Classification	Group D
Length [mm]	6.04 ± 0.34
Width [mm]	3.22 ± 0.20
Thickness [mm]	2.79 ± 0.26
Geometric mean diameter [mm]	3.86 ± 0.34
Equivelant Spherical Diameter [mm] *	3.657 ± 0.001
Sphericity [%]	60 ± 3
Thousand seed mass [g]	36.47 ± 0.1
Bulk density [kg/m^3]	812 ± 3
Particle density [kg/m^3] *	1423.8 ± 0.7
Projected area [mm^2]	23 ± 2
Porosity [%] **	38.49 ± 1.36
Terminal velocity [m/s] **	9.86 ± 0.45 – 10.27 ± 0.52
Drag coefficient **	0.49 ± 0.05 – 0.53 ± 0.06

* Particle Density and Equivalent Diameter were calculated from the average kernel volume determined using a gas pycnometer.

** Güner (2007).

The particle characteristics greatly affect the conveying and entrainment of solids in a gas flow. The following properties will be explored separately as they are particle properties and are independent of the conveying fluid but will be utilized in many of the equations and parameters that will be discussed in Section 2.3.

2.2.1 Shape and Size

The geometric properties of the particles in a gas-solid flow have a large effect on the conveying characteristics (Fan and Zhu 2005). These properties include size, shape, overall size distribution, and family of shape. Agricultural particles are generally non-spherical and irregular; this can limit the application of findings from much published research, as plastic or glass spheres are generally used to simplify modelling. Even products considered spherical can be fairly irregular when it comes to size and shape, especially if they are a biological material.

Shapes are generally described by equivalent diameters which are based on volumes, terminal velocities or other properties that can be measured (Fan and Zhu 2005). There can be many equivalent diameters describing the size of an irregular particle depending on the application. A few common terms to describe a particle are displayed in Figure 2.5.

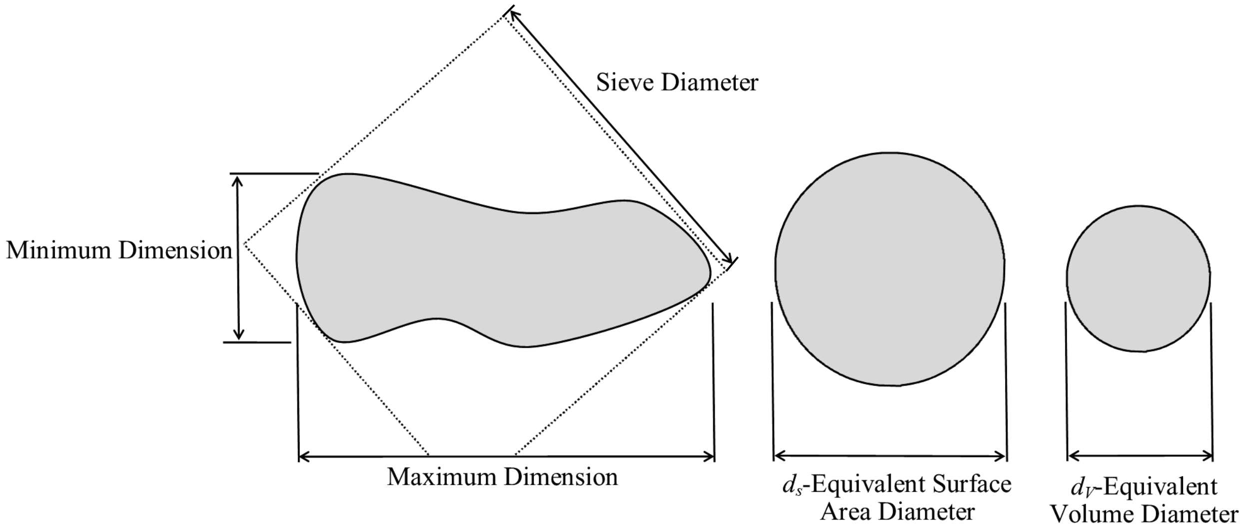

Figure 2.5: Schematic of a particle and its equivalent Sieve, Area, and Volume Diameter (Adapted from Fan and Zhu (2005)).

Fan and Zhu (2005) describe the surface area diameter, volume diameter, and sieve diameter as the following. The equivalent surface diameter d_s, is defined as the diameter of a sphere that has the same surface area as the irregular particle. Similarly, the equivalent volume diameter, d_v, is the diameter of a sphere with equal volume to the particle, V_p.

$$d_e = \left[\frac{6(V_p)}{\pi}\right]^{\frac{1}{3}} \tag{2.1}$$

The sieve diameter is the smallest square opening the particle will fall through during sieving. To estimate the diameter of a particle using sieves a standard is to be followed. Two examples are the Tyler and the ASTM standard test methods for sieve analysis. The ASTM standard describes the range and size of sieve openings (ASTM 2006).

Additionally, the size characteristics can be measured by the following methods: microscopy, gas absorption, diffraction, laser Doppler phase shift, and impaction (Fan and Zhu 2005). The details of these methods will not be reviewed here, but the wide range of methods and complexity of testing suggest that determining the shape properties of a particle is not always a straightforward process.

Two other diameters common in the literature are the geometric mean diameter (d_g) and arithmetic mean diameter (d_a). The geometric mean diameter is the cube root of the product of the maximum, intermediate, and minimum diameter. Whereas the arithmetic mean diameter is the mean diameter of all the particles (Güner 2007). These diameters can be calculated using the following two equations given by Güner and measuring the maximum (l_{max}), intermediate (l_{int}), and minimum (l_{min}) dimension of the particle.

$$d_g = [(l_{max})(l_{int})(l_{min})]^{\frac{1}{3}} \tag{2.2}$$

$$d_a = \frac{l_{max} + l_{int} + l_{min}}{3} \tag{2.3}$$

Whereas the sphericity of a particle, ψ, is calculated using the following equation.

$$\psi = \frac{[(l_{max})(l_{int})(l_{min})]^{\frac{1}{3}}}{l_{max}} \tag{2.4}$$

2.2.2 Particle Density

The density of both the solid and the fluid phase of the pneumatic conveying system are very important quantities for calculating velocities, Reynolds numbers, and other properties. The solid bulk density (ρ_b) and particle density (ρ_p) are generally given in literature and are required for further calculations. The bulk density is calculated by simply taking the mass of a known volume of either freely settled or tapped (must be stated) particles to obtain the density (Fan and Zhu 2005). This density takes into account the volume of the solid fraction, the inter-particle void fraction, and the internal voids. The particle density can be measured using a gas pycnometer to determine the volume of the solid fraction (including internal voids). The mass of the particles is then divided by the volume of the solids fraction to give ρ_p.

2.3 FACTORS AFFECTING FLOW AND PARTICLE ENTRAINMENT

The factors that affect a particle's flow characteristics and its initial entrainment will be discussed in the following sections. These major factors are the fluid density, fluid viscosity, void-solids concentration, slip velocity, fluid Reynolds number, particle Reynolds number, drag force, friction forces, collision forces, and gravitational forces. Additionally, a few other effects that are hypothesised to come into play during testing for this project are shear-induced turbulent flow, Saffman force, Venturi effect, and turbulence suppression.

2.3.1 Dilute Phase Flow

The fluid flow condition most commonly encountered in agricultural pneumatic conveying is dilute two-phase flow. This flow regime is simply described as having a large conveying gas to solids ratio while being operated at relatively high velocities (Klinzing, Rizk et al. 2010). Generally the conveying gas will have a velocity in the range of 12 m/s for a very fine powder, 16 m/s for a fine granular material, to greater than 25-30 m/s for large particles (Mills 2004). A dilute phase system will also have a solids to gas mass flow ratio of less than 15 (Klinzing, Rizk et al. 2010)

Consistent dilute phase flow is necessary for accurate product splitting and delivery to seeding implements. If the flow is in transition between dilute and dense phase flow, pulsing (slug flow) of the product will occur, causing uneven seed spacing and potential plugging. Unique challenges of dilute phase conveying include using higher power per unit mass conveyed than other pneumatic systems (Barbosa and Seleghim Jr. 2003) and causing pipe wear and product damage due to higher conveying velocities (Klinzing, Rizk et al. 2010).

2.3.2 Pressure Drop

As an initial starting point in determining the pressure loss of a pneumatic conveying system the general pressure drop equation due to friction as developed by Darcy can be used:

$$\Delta p = \frac{\lambda_L \rho L v^2}{2D} \tag{2.5}$$

where

λ_L is the pipe friction factor,

ρ is the fluid density,

L is the pipe length,

v is the superficial fluid velocity, and

D is the pipe inner diameter.

This equation will give an estimate of the pressure loss due to the conveying pipe but does not take into account the particle acceleration or fitting pressure losses.

2.3.3 Conveying Fluid Density

The fluid density is calculated knowing the barometric pressure, relative humidity, saturation pressure, and the operating temperature as shown in the following equation. While calculating the density of dry air is quite straightforward, humid air requires the use of partial pressure formulas. The saturation pressure (p_{sat}) of air can be found by taking a regression of steam tables at the operating temperature. Knowing the saturation pressure, the vapour pressure can be found by simply multiplying p_{sat} by the relative humidity. The difference between the barometric pressure and the vapour pressure is therefore the pressure of dry air using the principal of partial pressures. The density of humid air is then calculated as a mixture of ideal gases as follows:

$$p_v = R.H. * p_{SAT} \tag{2.6}$$

$$\rho_{Humid\ Air} = \frac{p_d}{R_d T} + \frac{p_v}{R_v T} \tag{2.7}$$

where

$\rho_{Humid\ Air}$ is the density of humid air [kg/m^3],

p_d is the pressure of dry air [Pa],

p_v is the pressure of water vapour [Pa],

R_d is the specific gas constant for dry air, 287.058 [J/kg K],

R_v is the specific gas constant for water vapour, 461.495 [J/kg K], and

T is the temperature in degrees Kelvin.

At a station barometric pressure of 720 mmHg or 95.99 kPa, 50% R.H. and 20 ºC the density of humid air was calculated to be 1.135 kg/m^3.[1]

2.3.4 Dynamic Viscosity

Dynamic viscosity is another important parameter that is needed to calculate the Reynolds number of the conveying fluid. The main influence on the viscosity of a fluid is the temperature, which for conveying is the operating temperature of the gas. The dynamic viscosity based on temperature effects can be found using Sutherland's formula as described by Smits and Dussauge (2005):

$$\eta = \eta_0 \frac{T_0 + C}{T + C}\left(\frac{T}{T_0}\right)^{\frac{3}{2}} \qquad 2.8$$

where

η is the dynamic viscosity at input temperature [Pa s],

η_0 is the reference viscosity at T_0 [Pa s] (18.97 μPa s for air),

T is the input temperature [K],

T_0 is the reference temperature [K] (291.15 K for air), and

C is Sutherland's constant for the gas (C=120 for air).

For moderate pressures (less than 35 atm), the temperature effect on viscosity of the gas is not influenced by more than 10% (Klinzing, Rizk et al. 2010). For the operating conditions typically found in the lab conveying system (~25 ºC), the dynamic viscosity is calculated using Equation 2.8 to obtain 1.93 x 10^{-5} Pa s. There is less than a 2% difference between this and the reference viscosity which indicates that while temperature does have an effect on viscosity, it is small at these operating conditions.

---

[1] Typical station barometric pressure (station is at an elevation of 504 m and values were not corrected to sea level), R.H. and temperature measured in the laboratory.

2.3.5 Void-Solid Concentration and Slip Velocity

Two important factors in the modeling and prediction of gas-solid flow are the voidage (void-solid ratio) and the slip velocity. Pahk and Klinzing (2010) describe the void-solid ratio as the volume between particles containing the carrier fluid in a given control volume. The voidage can be used to better understand plug characteristics, the pressure drop between two points, particle velocity and the friction factor (Pahk and Klinzing 2010):

$$\varepsilon = \frac{V - V_S}{V} = 1 - \mu \frac{\rho}{\rho_p} \frac{v_\varepsilon}{v_p} = \frac{1 - \rho^*}{\rho_p} \qquad 2.9$$

where

ε is the void ratio,

V is the pipe volume [m^3],

V_S is the enclosed solids volume [m^3],

ϕ is the mass loading ratio,

ρ^* is the apparent bulk density [kg/m^3],

ρ_p is the particle density,

v is the superficial gas velocity,

v_ε is the voidage or the average fluid velocity between particles, and

v_p is the average particle velocity.

If the superficial gas velocity is a known quantity the voidage, V_e can be given as:

$$v_\varepsilon = \frac{v}{\varepsilon} \qquad 2.10$$

Therefore, if the voidage, density, and mass flow rate are known, the particle and/or the fluid velocity between particles can be found (Klinzing, Rizk et al. 2010). Similarly, the slip velocity (w_s) is the difference between the conveying gas and the particle velocities.

$$w_s = v_\varepsilon - v_p = \frac{v}{\varepsilon} - v_p \qquad 2.11$$

2.3.6 Conveying Fluid Reynolds Number

The flow regime of a fluid is described by its Reynolds number, Re, a dimensionless unit that compares the inertial forces to viscous forces during flow (Fan and Zhu 2005):

$$Re = \frac{\rho D v}{\mu} \tag{2.12}$$

where

Re is the Reynolds number of the conveying fluid,

ρ is the density of the conveying fluid [kg/m3],

D is the inner diameter of the pipe [m],

v is the velocity of the conveying fluid [m/s], and

μ is the dynamic viscosity of the fluid [kg/ (m s)].

Pipe flow is considered laminar if the Reynolds number is lower than 2300 for a given pipe inner diameter. Laminar flow is characterized by concentric flow layers, with the highest fluid velocity in the center of the pipe. The fluid velocity drops quickly close to the pipe wall or boundary layer (Klinzing, Rizk et al. 2010). Turbulent flow occurs in flows with a Reynolds number of greater than 4000 and is characterized by random fluid movement and a much flatter velocity profile. Transition flows occur between $2300<Re<4000$ where properties of either regime can be noticed, depending on factors such as wall roughness and flow development.

The temperature directly affects the dynamic viscosity as shown in Equation 2.8 which in turn has a linear effect on the Reynolds number as shown in Equation 2.12 that is more pronounced as the velocity increases. Typical values for conveying agricultural materials range from 2.0×10^4 to 1.5×10^5.

2.3.7 Particle Reynolds Number

The Reynolds number of a single particle is necessary for calculating the drag coefficient of a particle, which in turn is required for calculating the drag force. The formula is shown below and is nearly identical to the Reynolds number for pipe flow except the diameter is of the particle and w_s is the slip velocity between the superficial gas velocity and the particle's velocity.

$$Re_p = \frac{\rho D_p w_s}{\mu} \qquad 2.13$$

Where:

Re_p is the Reynolds number of the particle,

ρ is the density of the conveying fluid [kg/m3],

D_p is the diameter of the particle [m],

w_s is the slip velocity (v_ε-v_p) [m/s], and

μ is the dynamic viscosity of the fluid [kg/ (m s)].

A typical Re_p range for wheat is 4 x 10^3 to 8 x 10^3. Canola has a Re_p of less than 2 x 10^3 at typical conveying velocities while chickpeas can have a Re_p of up to 1.6 x 10^4 due to their large diameter.

2.3.8 Minimum Conveying Velocity

The minimum conveying velocity refers to lowest conveying gas velocity that a system can operate at without behaving erratically or plugging. There are many terms in the literature for this velocity, some of which include the saltation velocity, pick-up velocity, critical velocity, initial mixing velocity, or the velocity at the minimum pressure drop (Hubert and Kalman 2003). For dilute phase conveying, the saltation velocity will be 2-2.5 times lower than the pickup velocity for a single particle and nearly equal for a layer of particles (Hubert and Kalman 2004). For purposes of this work, the saltation velocity will be defined as the minimum conveying velocity of the system.

Figure 2.6 shows the predicted relationship between the mass loading ratio, ϕ, which is defined as the mass flow rate of the particles ($\dot{m}_p$) divided by the mass flow rate of the conveying gas ($\dot{m}_g$) and saltation velocity u, using the estimation developed by Cabrejos and Klinzing (1994). This formula tends to overestimate the saltation velocity for very dilute flows according to Hubert and Kalman (2003)

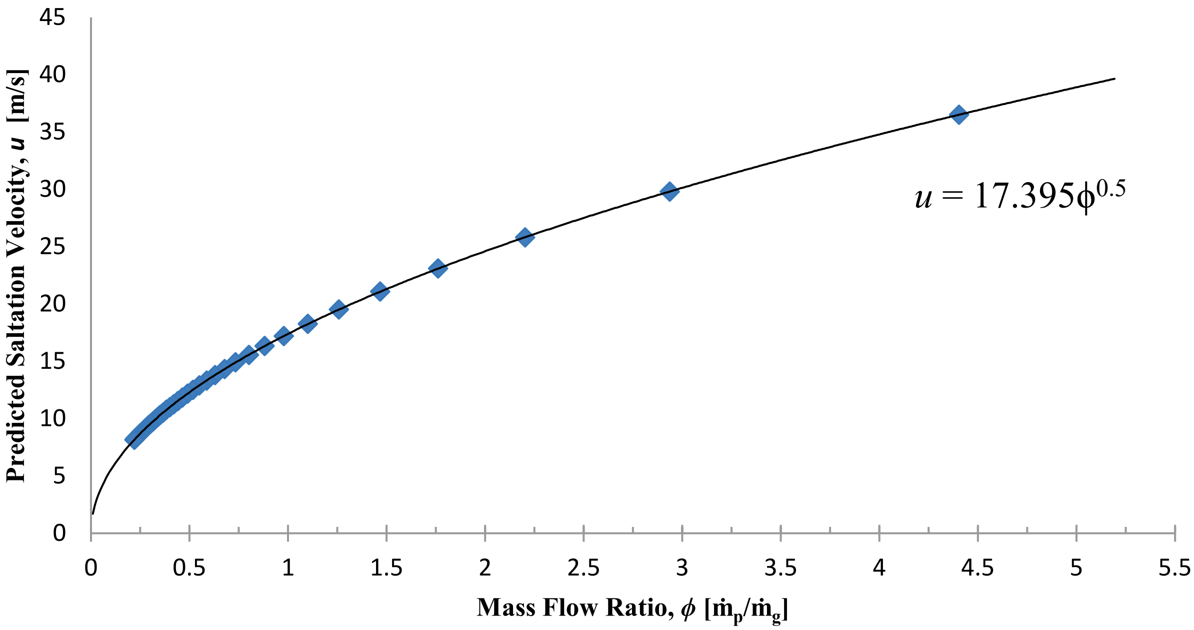

Figure 2.6: Saltation Velocity vs. Mass Flow Ratio of wheat at a particle density of 1460 kg/m^3 using the estimation developed by Cabrejos and Klinzing (1994)

2.4 FORCES ON A PARTICLE

The following sections outline the forces that act on a particle. The drag force provides the positive acceleration while the other forces either act to suspend, settle, or slow down the particles.

2.4.1 Drag Force

One of the most important quantities in pneumatic conveying and entrainment of particles is the drag force. The drag force accelerates the particle in the direction of fluid flow. The difference between the gas velocity and the particle velocity provides for this acceleration.

The drag coefficient is related to the Reynolds number of the particle (which is directly related to the particle diameter) and can be found from a standard drag coefficient curve (Klinzing, Rizk et al. 2010) or through empirical equations such as the one developed by Turton and Levenspiel (1986):

$$C_D = \frac{24}{Re_p}\left(1 + 0.173 * \left(Re_p\right)^{0.657}\right) + \frac{0.413}{1 + 16300 * \left(Re_p\right)^{-1.09}} \qquad 2.14$$

The drag force is useful in analyzing the force on a particle. This along with the acceleration force, the force due to gravity, and friction forces need to be overcome by the drag force to convey a particle. The drag force is shown in Equation 2.15,

$$F_D = C_T(w_s)^2, \qquad 2.15$$

where:

C_T is the turbulent drag factor and

w_s is the slip velocity [m/s], u_g-u_p.

Substituting Equation 2.16 into Equation 2.15 $\mathrm{F_{DRAG}}$ can be simplified into Equation 2.17,

$$C_T = \frac{1}{2} C_D \rho A^* \qquad 2.16$$

$$F_D = \frac{C_D \rho {w_s}^2 A^*}{2}, \qquad 2.17$$

where:

A^* is the projected area [m^3]

C_D is the drag coefficient,

ρ is the density of conveying fluid (air) [kg/m^3], and

${w_s}^2$ is the slip velocity [m/s], $\left(u_g - u_p\right)^2$.

The drag force on a particle is calculated using the simplified Equation 2.17 as described by Klinzing, Rizk et al. (2010). Because the drag force is directly related to particle diameter, the method of measuring the diameter becomes important for accurate predictions.

An estimation of the power required to convey the particles is given by the following equation. Due to the cubed relationship with velocity, the conveying power is greatly affected by changes to the conveying velocity.

$$P = F_D * v = \frac{C_D \rho v^3 A^*}{2} \qquad 2.18$$

2.4.2 Other Lift Forces

Small particles in a shear field will encounter a lift force perpendicular to the direction of fluid flow. This force was first described by Saffman (1965) for small particles in very viscous flows. The shear lift force is given in Equation 2.19 which is a generalization of Saffman's one dimensional form given by Drew (1976).

$$F_{ls} = 6.46 c_{ls} r^2 \sqrt{\rho\mu} \frac{u_r D_T}{\sqrt{D_T}} \qquad 2.19$$

Where:

c_{ls} is the Saffman lift coefficient,

r is the particle radius [m]

ρ is the fluid density [kg/m^3],

μ is the viscosity of the fluid [Pa s],

u_r is the relative fluid velocity [m/s], and

D_T is the rate of deformation tensor.

The other relevant lift force is the rotational or Magnus lift force which is given in equation 2.20. This force acts perpendicular to the plane created by the velocity and the spin vector of the object (Mehta 1985).

$$F_{lm} = S(\omega_r \times u_r) \qquad 2.20$$

Where:

S is the air resistance coefficient across the objects surface,

u_r is the fluid velocity [m/s], and

ω_r is the angular velocity [m/s] of the particle.

2.4.3 Gravitational Force

The force due to gravity acts to pull particles to the bottom wall in a horizontal conveying system. This force must be balanced or overcome by other lift forces in order to achieve fully entrained dilute phase flow. The gravitational force acting on a particle is given in the following equation.

$$F_g = [m_p - m_f]g \qquad 2.21$$

Where:

m_p is the mass of the particle with diameter d [kg],

m_f is the mass of fluid displaced by the particle with diameter d [kg], and

g is the acceleration due to gravity [m/s^2].

2.4.4 Electrostatic Force

Another general force that acts counter to both drag and lift forces is the electrostatic force. Particles in motion can experience significant electrostatic forces due to their induced charge. This effect is especially noticeable with small particles in ungrounded or plastic conveying lines and when the conveying air is dry (Klinzing, Rizk et al. 2010).

$$F_e = \left[E_x \left(\frac{q}{m_p}\right) m_p\right] \qquad 2.22$$

Where:

E_x is the electric field [N/C],

m_p is the mass of the particle with diameter d [kg], and

q is the charge [C].

2.5 VISUALIZATION OF FORCES ACTING ON A SINGLE PARTICLE

The factors outlined previously all play a role in the basic mechanics of conveying a single particle (i.e. assumed no interaction with other particles for simplification). A force analysis will be completed to illustrate the basic underlying relationships to achieve pneumatic conveying.

The major forces on a single particle are shown with a Free Body Diagram (FBD) in Figure 2.7. The forces for a single particle that is fully entrained are: drag force in the x-direction, drag force in the y-direction (due to turbulent eddies), electrostatic forces, and the force due to gravity. These forces will be described individually along with other forces not included in this analysis but important in pneumatic conveying.

Not shown are friction forces from contact with the wall or other particles as this was an assumed single particle model. These forces would cause a deceleration of the particle which would then need to be re-accelerated by the drag force.

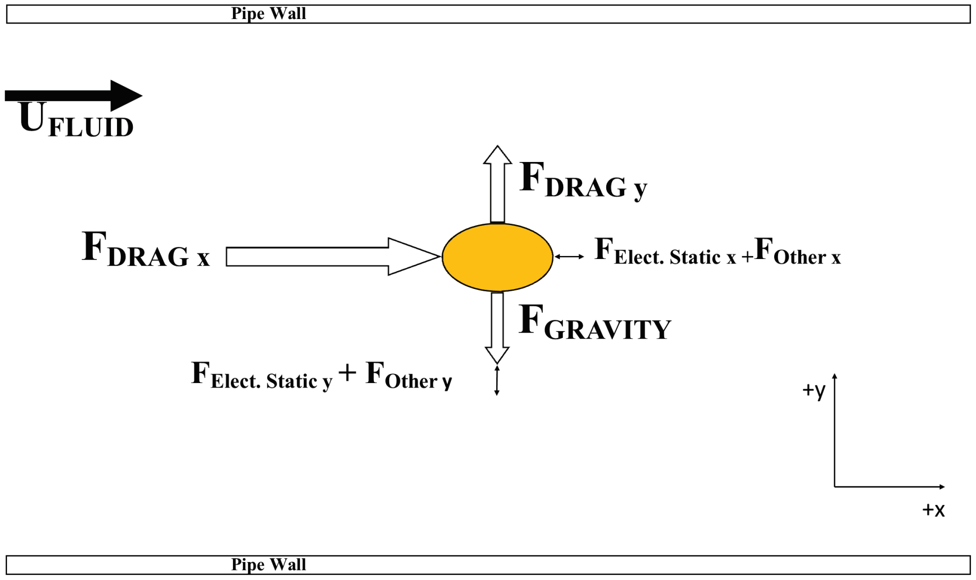

Figure 2.7: Simple free body diagram showing the main forces acting on a single particle fully entrained (i.e. no collision or friction forces).

The drag force is required for motion and can be generalized as the force caused by a velocity difference between the conveying fluid and the particle. Equations 2.15, 2.16, and 2.17 describe the drag force. The force balances are shown in Equation 2.23 and 2.24 for the generic case of multiple particles with collision terms (particle-wall and particle-particle interaction) shown but not discussed in this analysis due to the limited scope of this paper.

$$F_{NET_x} = F_{DRAG_x} + F_{ELECTROSTATIC_x} + F_{COLLISIONS_x} + F_{OTHER_x} \qquad 2.23$$

The net force in the x-direction must be positive for particle acceleration, theoretically zero to maintain conveying velocity, and negative if the particles are being decelerated. The $\mathrm{F_{DRAG_x}}$ must be large enough at the conveying slip velocity to overcome the negative forces caused by electrostatic forces, friction forces, and energy loss due to collisions.

$$F_{NET_y} = F_{DRAG_y} + F_{GRAVITY_y} + F_{ELECTROSTATIC_y} + F_{COLLISIONS_y} + F_{OTHER_Y} \qquad 2.24$$

A generally positive or zero net force in the y-direction must be maintained in order to have dilute and fully entrained conveying. The drag force in the y-direction is due to velocity caused by eddies, Saffman and Magnus lift forces, and randomness in the turbulent fluid flow. Due to this turbulence and random motion, the $\mathrm{F_{DRAG_y}}$ may alternately act in the positive or negative y-direction, but will on average be positive to overcome the force due to gravity and keep the particles suspended (a net force of generally zero).

CHAPTER 3: OPTICAL FLOW PROFILING METHOD USED FOR VISUALIZATION AND EVALUATION OF FLOW DISTURBANCES IN AGRICULTURAL PNEUMATIC CONVEYANCE SYSTEMS

An optical flow profiling method and apparatus was designed and built to aid in quantifying the entrainment level of agricultural products in pneumatic conveying systems. This system consists of two major components: the optical imager and the positioning system. The imaging system uses a red laser to illuminate a cross section of fluid flow which is imaged using machine vision cameras to produce plots that represent the time averaged location of particles in the pipe. The positioning apparatus is used to place the imager in various orientations for different conveying systems in addition to moving along the conveying pipe.

This paper was co-authored by Dr. Scott D. Noble and published in Computers and Electronics in Agriculture in October 2015:

Keep T, Noble SD (2015) Optical flow profiling method for visualization and evaluation of flow disturbances in agricultural pneumatic conveyance systems Computers and Electronics in Agriculture 118:159-166 doi:10.1016/j.compag.2015.08.029

Fabrication of the optical imager was mainly completed by the author of this thesis in consultation with Dr. Scott Noble. Preliminary design of the imager stand was completed by B. Lozinsky and S. Gregoire in the course of their ABE 495 capstone design while Dr. Noble designed the optical platform. The machining of the optical platform and components was done in house at the College of Engineering Shops, University of Saskatchewan. The imager stand and positioning system was contracted out to Lean Machine Fabrication for final design and fabrication which I oversaw. Apparatus calibration, construction, and testing was performed by Mr. Keep along with data collection and analysis. I wrote the manuscript while Dr. Noble provided guidance, revisions, and editing.

The manuscript is formatted to fit this thesis with minor edits for flow, formatting, and numbering. A brief discussion of an alternative method of profiling the flow was added, along with comments on why it was not used.

OPTICAL FLOW PROFILING METHOD USED FOR VISUALIZATION AND EVALUATION OF FLOW DISTURBANCES IN AGRICULTURAL PNEUMATIC CONVEYANCE SYSTEMS

Tyrone Keep and Scott D. Noble

Department of Mechanical Engineering, University of Saskatchewan, Saskatoon, Saskatchewan, Canada S7N 5A9

e-mail: tyrone.keep@usask.ca, scott.noble@usask.ca

ABSTRACT

Pneumatic conveying is widely used for transporting granular materials and agricultural products. Traditional flow visualization methods are used extensively in experimental fluid dynamics but have not been commonly used with agricultural products as the flow seeding particles. A flow visualization method was developed to aid in understanding physical design changes made to agricultural pneumatic conveying systems. This optical flow profiling method is demonstrated by providing qualitative flow images and quantitative values to describe the behaviour of the particle flow, both upstream and downstream of a 25 mm spherical obstruction. The sphere was attached to the bottom of an acrylic conveying line that was conveying wheat particles [equivalent diameter: 3.66 mm] at an air speed of 20 m/s and a mass flow rate of approximately 5 kg/min. Probability density maps of particle occurrence were developed to describe the chance of a wheat particle being present in a particular location of the conveying line. The data contained in these maps were used to determine the centroid of the distribution and to plot the change in the cross-sections over the test area of the pneumatic conveying system.

Keywords: air seeder; pneumatic conveying; imaging; laser illumination; seed transport; dilute phase flow.

3.1 INTRODUCTION

Pneumatic conveying is an important and widely used method of handling agricultural materials. Specifically, air seeders employ dilute-phase pneumatic conveying for transporting seed and granular materials from the air cart (a mobile storage tank that dispenses seed and granular fertilizer) to the seeding implement (air hoe-drill or disc-drill). This method of seeding is popular for planting wheat and other small and medium grains in large fields in western Canada, the U.S. Midwest, Australia, Ukraine and Russia. As these implements have increased in size (the largest have planting widths in excess of 30 m wide) more attention is being paid to the nature of particle flow in the conveying line.

The fluid flow condition most commonly encountered in agricultural pneumatic conveying is dilute two-phase flow. Dilute phase flow is necessary for accurate product splitting and delivery to seeding implements, but it has some disadvantages. It utilizes higher power per unit mass conveyed than other pneumatic systems (Barbosa and Seleghim Jr. 2003) and can cause pipe wear and product damage due to higher conveying velocities (Klinzing, Rizk et al. 2010).

If the particle location through flow obstructions (elevation changes or bends) is better understood, conveying power can be potentially reduced while minimizing damage to the particles conveyed. This is of great interest in air seeder design and development, among other applications. Therefore, the objective of this study was to develop and test an optical system to image cross-sections of a laboratory-based conveying line to aid in understanding particle behaviour, and the cross-sectional location in particular. The system will need to incrementally obtain cross-sectional images upstream, adjacent to, and downstream of the obstruction to visualize the flow behaviour over the region of interest.

The main alternative method to an optical imaging system for flow profiling consists of physically sampling the flow. Various methods could be employed but a system that is similar to the work of Santos, Tambourgi et al. (2011) would be simplest to implement. The termination of the conveying line consisted of 9 square tubes that were made to fit into the pipe. The ends of these tubes were fitted with nylon bags to collect the particles that were located in that section of pipe and then the mass fraction per unit area was calculated. While this method is much simpler to execute it has some major disadvantages such as: being intrusive, lack of flexibility in the imaging location (must be at the end of the conveying line), and the grid spacing (and therefore profile resolution) is limited by the pipe and particle diameter.

The concept of using a laser to illuminate a thin sheet of a fluid flow is not new (Adrian and Yao 1985, Maas, Gruen et al. 1993, Westerweel 1997, Yan and Rinoshika 2011). Laser light sheet flow visualization has been around in many forms since the 1980's and has been used to visualize the behavior of fluid flows seeded with small particles that are assumed to mimic the fluid's behavior (Adrian 1991). Other methods such as Particle Imaging Velocimetry (PIV), Stereo PIV, and Particle Tracking Velocimetry (PTV) use and have expanded on many of the same principles of visualizing a flow using laser light and tracer particles (Adrian and Westerweel 2011).

While these are all well understood techniques in experimental fluid mechanics for flows seeded with very small particles, they are not as widespread in pneumatic conveying systems that are designed to convey larger particles. Giddings, Azzopardi et al. (2011) used PIV to image the fluid behavior in a Venturi section of a coal conveying system. This study also included a brief description of laser sheet illuminated cross-sectional distributions of coal particles with a size range up to 140 µm. These images were used to visually describe the system but were minimally processed and were not the focus of the research. Yan and Rinoshika (2013) undertook a similar study using high-speed PIV to image large scale particles (≈2 mm). The main focus of these studies and others like them was to determine the velocity of the particles, not the probability of occurrence in a cross-sectional location.

3.2 METHODS AND MATERIALS

The optical flow profiling method that was developed to explore the location of product flow has two main subsystems: imaging and mechanical. The imaging portion of the apparatus was developed in order to quantify the flow behaviour of large agricultural particles being conveyed, while the mechanical system is used to position, align, and allow for movement along the conveying line.

3.2.1 Optical System

Selective illumination of a thin cross-section of the conveying line is achieved through the use of a red laser and a line generating optic. This creates a thin sheet of laser light perpendicular to the conveying line and the nominal direction of flow. As particles travel through the sheet of light they are illuminated. An image of this laser sheet and any particles that happen to be passing through it is captured with a machine vision camera and mirror. Subsequent images are taken and together they are used to develop a probability density map (PDM). The intensity of each pixel in the map indicates the probability of a particle travelling through that pixel location within the conveying line.

Figure 3.1 shows a schematic version of the optical system with the major components labeled. These include a 5 mW-635 nm laser and a Prosilica GC 1290 machine vision camera (Allied Vision Technologies GmbH, Stadtroda, Germany). The camera has a resolution of 1280 by 960 pixels and was operated at 15 frames per second with an exposure time of 0.05 seconds. This relatively long exposure was chosen as a compromise between available light, particle blur, and frame rate. The images of the cross section are captured through the use of a mirror and a band-pass interference filter that allows only light with the same wavelength as the laser to reach the camera sensor. This helps to remove noise due to extraneous lab lighting and enables future work with different laser wavelengths in the same enclosure. The laser sheet is created by a 635 nm red laser that is shaped using a cylindrical line generating lens, with a 30° spread with a Gaussian intensity profile. The optical system is mounted on an optics bread board attached to linear bearings and bearing rails. This and the rest of the mechanical system will be discussed in greater detail in the following section.

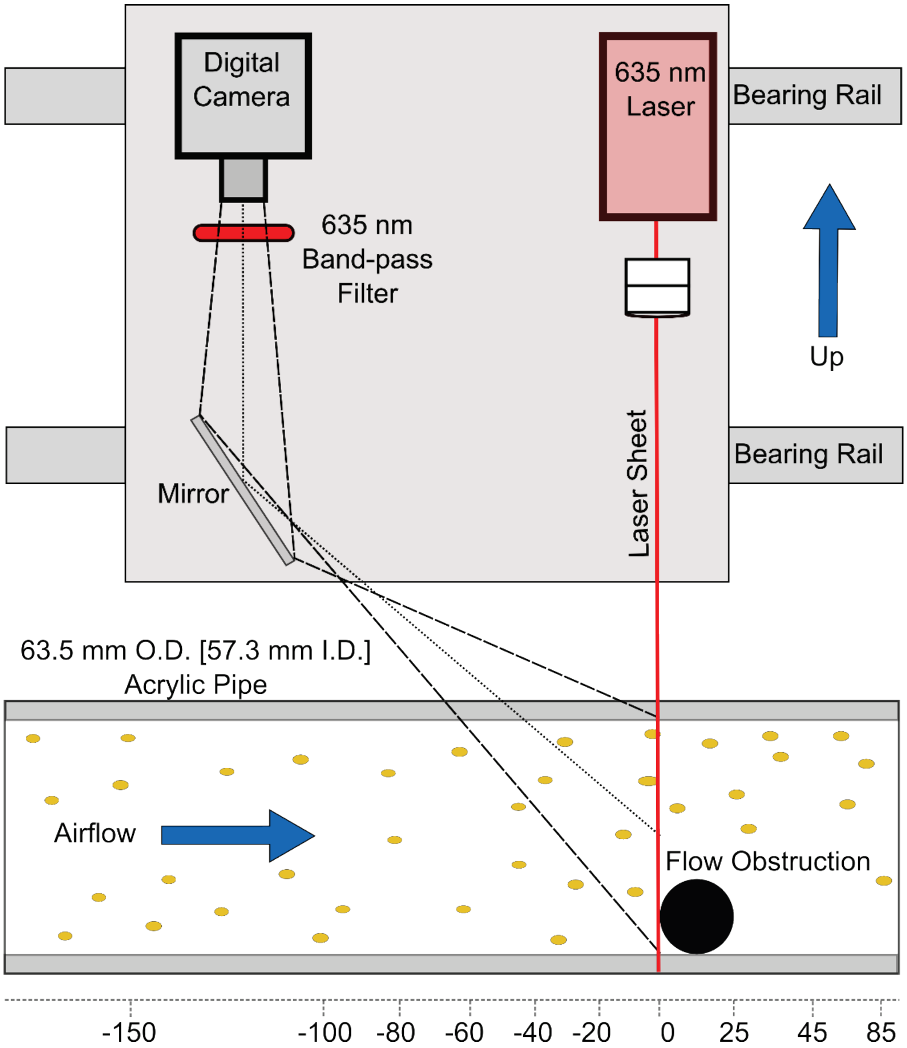

Figure 3.1: Schematic of the optical flow profiling apparatus. Distances not to scale but indicate test locations in mm. Red laser sheet illuminates a plane perpendicular to the product flow. Single images are taken, compiled, and averaged to give a map of the probability of a product being located at a given pixel.

The optical flow profiling apparatus was tested by affixing a 25 mm diameter sphere to the bottom of a clear acrylic section of the pneumatic conveying line (63.5 mm outer diameter, 57.3 mm inner diameter). This disturbance created a very noticeable change in the flow path of the conveyed product that illustrated the applicability of this two-phase flow visualization method. The apparatus was moved along the bearing rails to obtain incremental cross-sections upstream, adjacent to, and downstream of the sphere.

Wheat seed with properties as shown in Table 3.1 was metered at an approximate rate of 5 kg/min into a 20 m/s airflow [$Re_{air\ only} \approx 7.1x10^4$, $Re_{particle} \leq 4.8x10^3$ depending on superficial air velocity]. The wheat was dispensed from a lab-scale air cart using a meter roller controlled by a stepper motor. Conveying air was supplied by an electrically-controlled centrifugal fan with feedback loop to maintain a stable velocity.

Table 3.1: Average properties of the wheat used

1000 Seed Count Mass (g)	36.47
Bulk Density (kg/m^3)	812
Particle Density (kg/m^3) *	1424
Equivalent Spherical Diameter (mm) *	3.7

** Particle Density and Equivalent Diameter were calculated from the average kernel volume determined using a gas pycnometer.*

Cross-sectional probability density maps for particles were obtained by acquiring and processing successive images of the laser sheet and particles passing through it. An example of a single frame (captured with a different camera) taken at the mid-plane of the sphere (position 12.5 mm in Figure 3.1) is shown in Figure. 3.2.

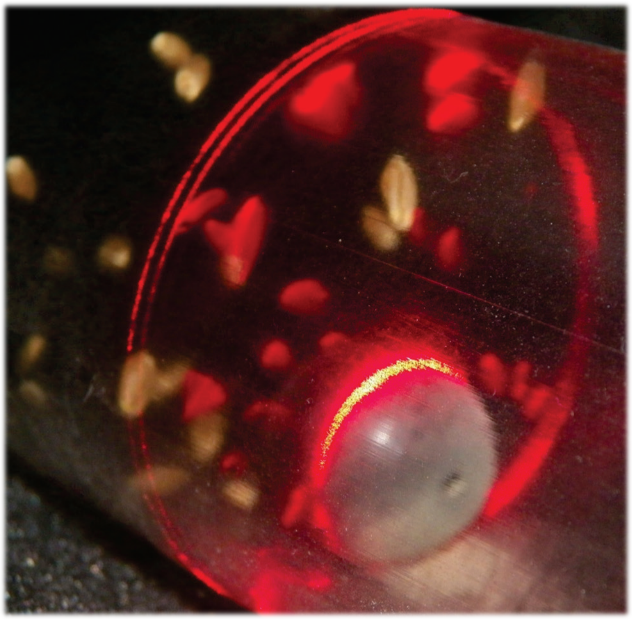

Figure**.** 3.2: Cross-section at mid-plane of sphere. Only particles directly in the laser sheet are illuminated and imaged with the machine vision camera. The double-ring artifact from the inner and outer surfaces of the tube are also visible. This image was taken with a handheld camera as an example of the particle behaviour.

In addition to particles reflecting light, the tube wall also intercepts and scatters part of the laser sheet to the camera. This artifact needed to be removed from the images as the intense ring of light would oversaturate the compiled image and wash out the much fainter reflections from the particles. The first step in this process was to develop an average reference frame without product flow. The average reference frame was then subtracted from the test images to minimize the artifacts caused due to the scattering of the laser sheet by the acrylic tubing. It was assumed that this tube wall interference was relatively consistent throughout the test. The proof of concept test was completed using Equation 3.1 with 50 reference frames collected, averaged and then subtracted from each of 1000 test frames with product flowing. A generalized schematic of this process is found in Figure 3.3.

$$PDM(i,j)=\sum_{k=1}^{N}\left(\frac{I_k(i,j)-R(i,j)}{\sum_{i=1}^{m}\sum_{j=1}^{n}\left(I_k(i,j)-R(i,j)\right)}\right)\left(\frac{1}{N}\right), \qquad 3.1$$

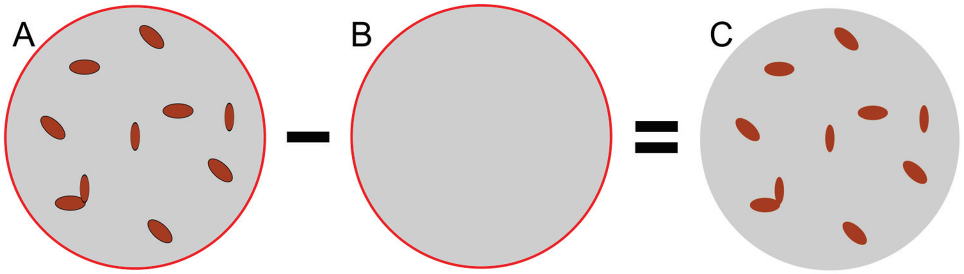

Figure 3.3: Schematic of the artifact removal process. An average reference image was compiled from 50 successive images with no product flow. This reference was then subtracted from each test image (with product flow) to obtain 1000 individual modified test images. This operation removes the majority of the static laser artifacts around the edge of the images.

Artifact removal was completed on-the-fly as each image was collected using National Instruments LabVIEW data acquisition software with the NI Vision module (National Instruments, Austin, TX.). After artifact removal an average of the images was calculated, as shown in Figure 3.4, to obtain a raw probability density map of the particle location within the conveying line.

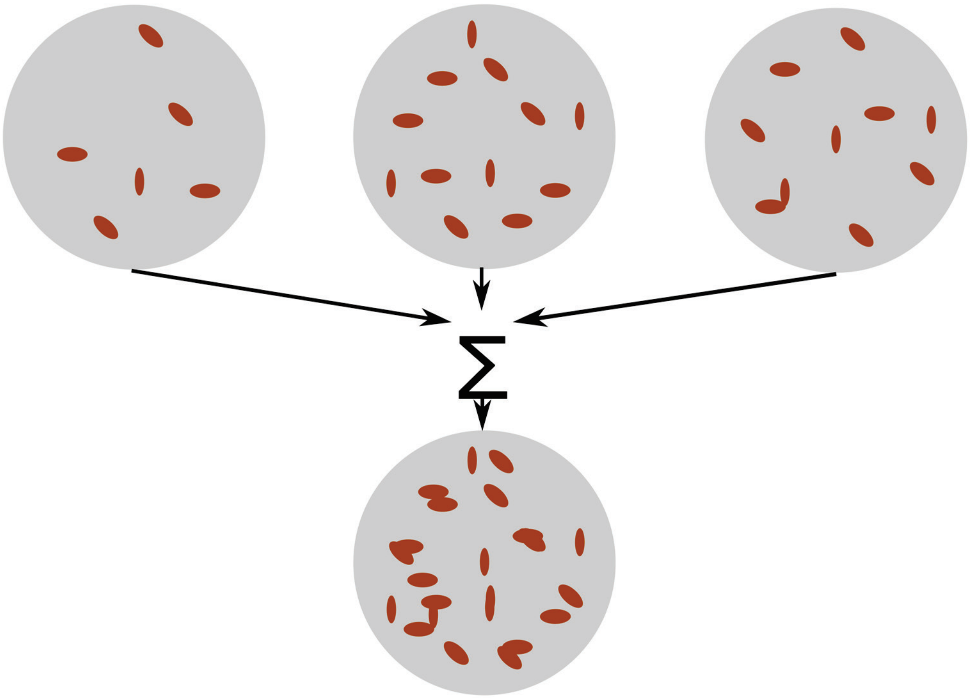

Figure 3.4**:** Generalized method to create an averaged and normalized image. Successive images are added together, the intensity of the pixels are summed, and then normalized by the number of total images.

The normalized cross-section of each location was post-processed using ENVI+IDL image analysis software (Exelis Visual Information Solutions, Boulder, CO.) to develop the probability density maps and to determine the location of the centroid of these maps. An example of an unprocessed image is shown in Figure 3.5. The top of the conveying line is to the right of the image.

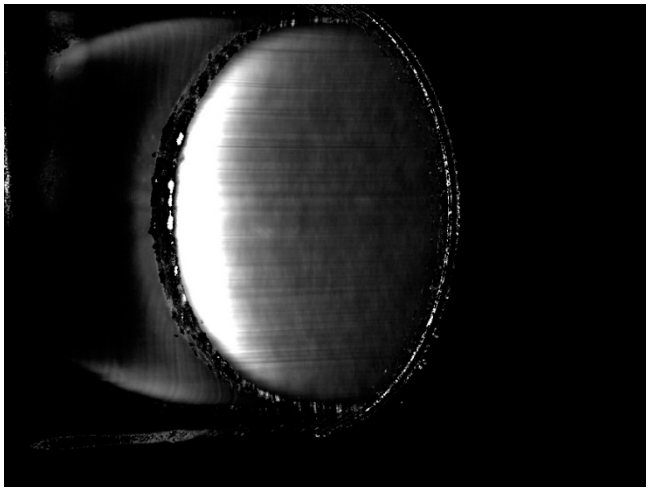

Figure 3.5**:** Example of an unprocessed output from LabVIEW and NI Vision Acquisition Software. The majority of laser artifacts were removed using the air only reference image but some residual light sheet interaction with the tube wall remains. This will be cropped in post-processing along with rotation and scaling operations.

The cross-sections were manually evaluated to determine the centre coordinates of the image, as minor variations were observed between imaging locations. The x and y coordinates of the pipe edge were determined and the centre point was calculated using Equation 3.2. The centre positions were used to align images prior to resizing and applying a rough crop of unwanted data.

$$CP = \left\{ \left(\frac{x_{\max} - x_{\min}}{2} + x_{\min} \right), \left(\frac{y_{\max} - y_{\min}}{2} + y_{\min} \right) \right\} \qquad 3.2$$

The image was then resized by applying a stretch factor based on the ratios of the ranges of maximum and minimum *x* and *y* values. The stretch was applied in the x-axis to correct for perspective distortion (Figure 3.6-A) and then rotated counter clockwise around the centre point to adjust for camera position with respect to true vertical (Figure 3.6-B). To evenly remove unnecessary data (any part of the image outside of the pipeline) a mask was manually applied in ENVI to remove as many laser artifacts as possible (Figure 3.6-C). This mask was then applied as the cropping boundary for all successive images to minimize any human application error.

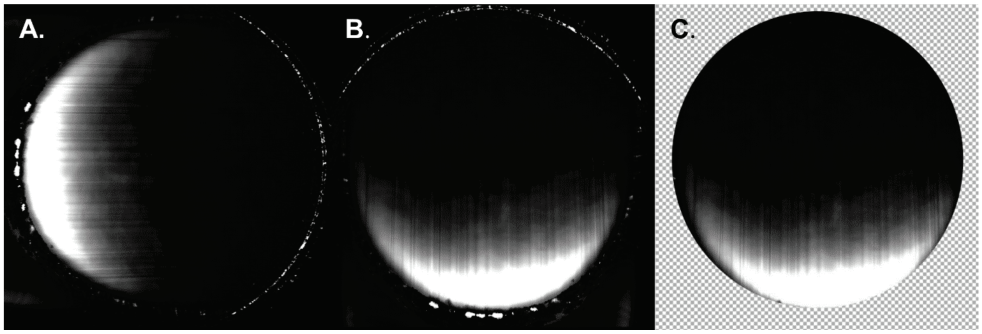

Figure 3.6: Sequence of post-processing steps performed on the unprocessed image shown in Figure 3.5. Panel A: image is resized to account for perspective distortion and rough cropped. Panel B: image is rotated counter clockwise 90 degrees. Panel C: mask is applied to remove remaining wall effects.

The processed images were then used to calculate the probability density maps and the vertical centroid of the distribution for each map. This was calculated by multiplying the individual pixel intensity by the vertical location of each pixel. This value was then divided by the overall intensity as shown in Equation 3.3.

$$Vertical\ Centroid\ of\ PDM = \frac{1}{\sum_{i=1}^{m}\sum_{j=1}^{n} PDM(i,j)} \sum_{j=1}^{n}\sum_{i=1}^{m}\left(PDM(i,j)(j)\right) \tag{3.3}$$

3.2.2 Mechanical System

The mechanical system gives the optical flow profiling apparatus the ability to image particles in many orientations and in differing styles of pneumatic conveying systems Figure 3.7. The structural stand supports the imager itself and provides both coarse and fine height adjustment using a series of threaded rods, winch and cable, and safety pins. A sliding carriage is attached to the main upright and contains the height adjustment mechanism and serves as an attachment point for the rotation hub. This hub enables the imaging system to rotate from horizontal to a vertical position in either direction.

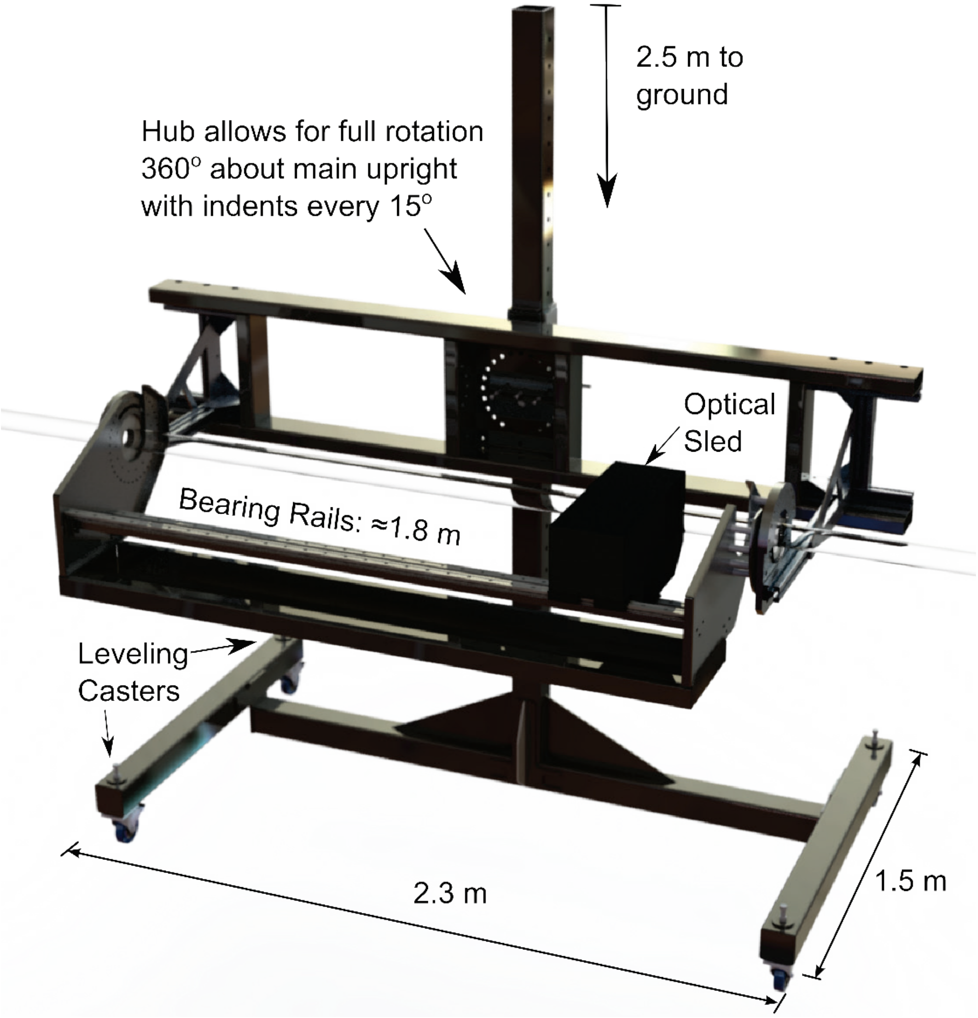

Figure 3.7: CAD model of Optical Flow Profiler and stand. Major components are labeled with a brief description and approximate overall dimensions are listed.

Attached to the rotation hub and carriage is the imaging platform. This is shown in Figure 3.8 and includes the optical flow profiling sled, bearing rails, cable tray, and rotating end mounts. The sled contains an optical bread board on which the laser, camera, and other optical components are mounted. This is contained in a housing painted flat black to minimize laser reflection and reduce stray light affecting the image.

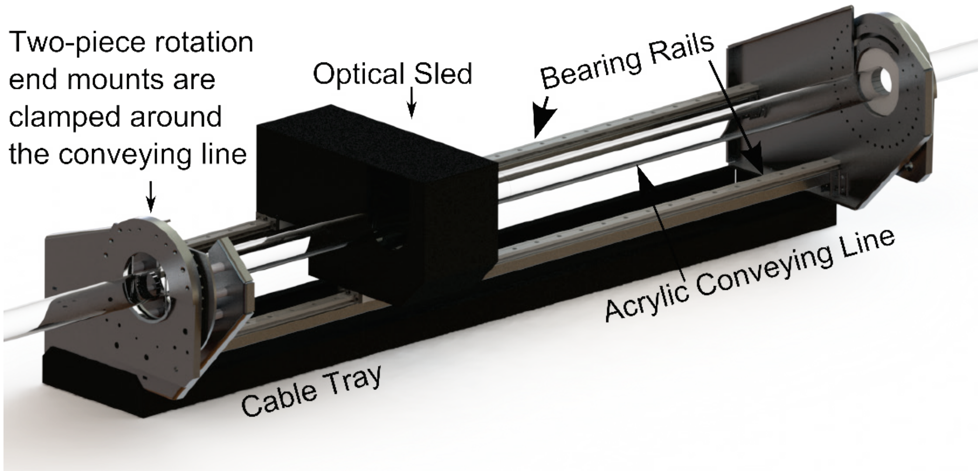

Figure 3.8: Imaging platform: optical sled can slide along pipeline on the bearing rails and two-piece end mounts allow for rotation around the acrylic conveying line.

A key innovation in the mechanical platform was in the design of the end mounts. These serve to maintain alignment of the imaging systems with the conveying line, and facilitate rotation of the imaging system around the conveying line. The mounts were designed so that the imager can rotate 360° around the conveying line, giving flexibility in positioning the laser plane source with respect to the conveying line. The end mounts and rotational guide track also allow the imager to be inserted around the conveying line, instead of having to disconnect the conveying line and threading it through the end mounts. In this application, the ability to position the imager around different sections of conveying line without having to disturb the line is advantageous. As illustrated in Figure 3.9, the top piece of the end mount is removable to allow the imaging platform to be positioned on a section of conveying line as shown. The clamping collar can be replaced to image pipe up to 18 cm in diameter.

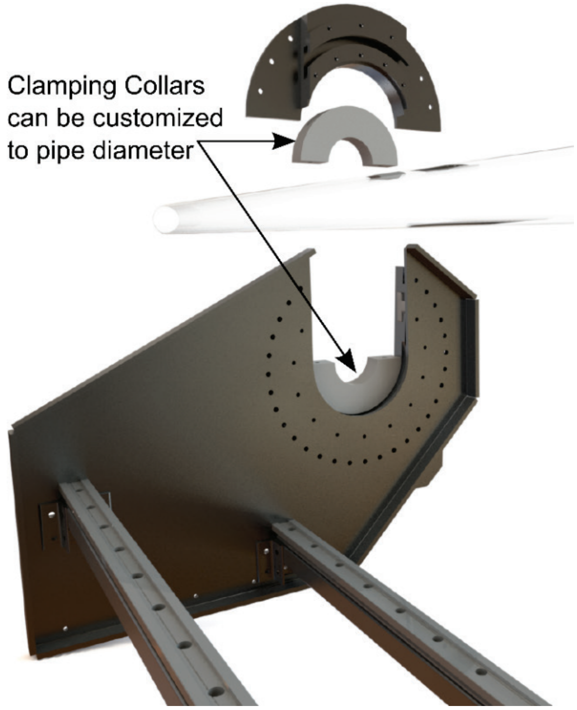

Figure 3.9: Exploded view of imager endmount. In the neutral position (as shown) the top section can be removed to allow for insertion of the conveying line.

The design of the optical flow profiler attempted to prevent or minimize alignment errors wherever possible but some cautions must be taken. Positional variation between successive images is on the order of 0.1 to 1 millimetre, while repositioning the mechanical system can shift the framing of the pipeline within the image by upwards of a centimetre. Manual determination of the centre point of each averaged image was implemented as described previously in Equation 3.2 to overcome this error

3.3 RESULTS AND DISCUSSION

The probability density maps of the particle occurrence and the resulting centroids were developed upon completion of the testing. From the following results, the particle behavior due to the effect of the obstruction can clearly be determined.

3.3.1 Particle Occurrence Probability Density Maps

Nine of the most descriptive cross-sections are shown in Figure 3.10. These cross-sections are grouped by location: upstream of the sphere's leading edge, around the sphere, and downstream of the sphere's leading edge. Wheat was conveyed into a 20 m/s airstream at 5 kg/s. One thousand test frames were taken at each of the nine locations and then processed as described previously. The location of each cross-section is indicated in the figure with respect to the leading edge of the sphere (the point on the sphere furthest upstream). The striations noticeable in the figure are due to the manufacturing process of the acrylic tube (extrusion marks) which could not be masked from the image as they are caused by reflection off the particles. While they are very noticeable in the final images, they do not affect the conclusions drawn from the data.

The upstream particle occurrence maps (Figure 3.10-A) indicate a higher probability that a particle would be located in the lower third of the conveying line. A change in the distribution can be seen 20 mm upstream of the leading edge with a tendency for the product to begin moving to the upper portion of the air line. This trend is reinforced in the cross-sections around the sphere. A small arc of high probability is noticeable at the very top of the pipe which is attributed to reflection off the pipe wall. The use of reference frames was intended to minimize this effect but not all artifacts were removed completely in every image.

Figure 3.10-B describes the three cross sections in the immediate vicinity of the sphere. The leading edge cross section has a high probability that a particle would be located at the very bottom of the conveying line. This trend is due to the particles being slowed down by the proximity of the sphere and influencing the intensity of the laser light reflected. A rapid upwards shift of particles begins at the centre image, with a high probability of particles being slowed down around the edge of the sphere. The majority of particles are located in the upper portion of the conveying line at the trailing edge.

The downstream cross-sections (Figure 3.10-C) indicate a very high probability that a particle would be located in the upper third of the acrylic tube with a low probability of particles present in the wake of the sphere. The distribution of particles slowly descends to resemble the upstream distributions as shown in the cross-section taken at 525 mm downstream of the leading edge.

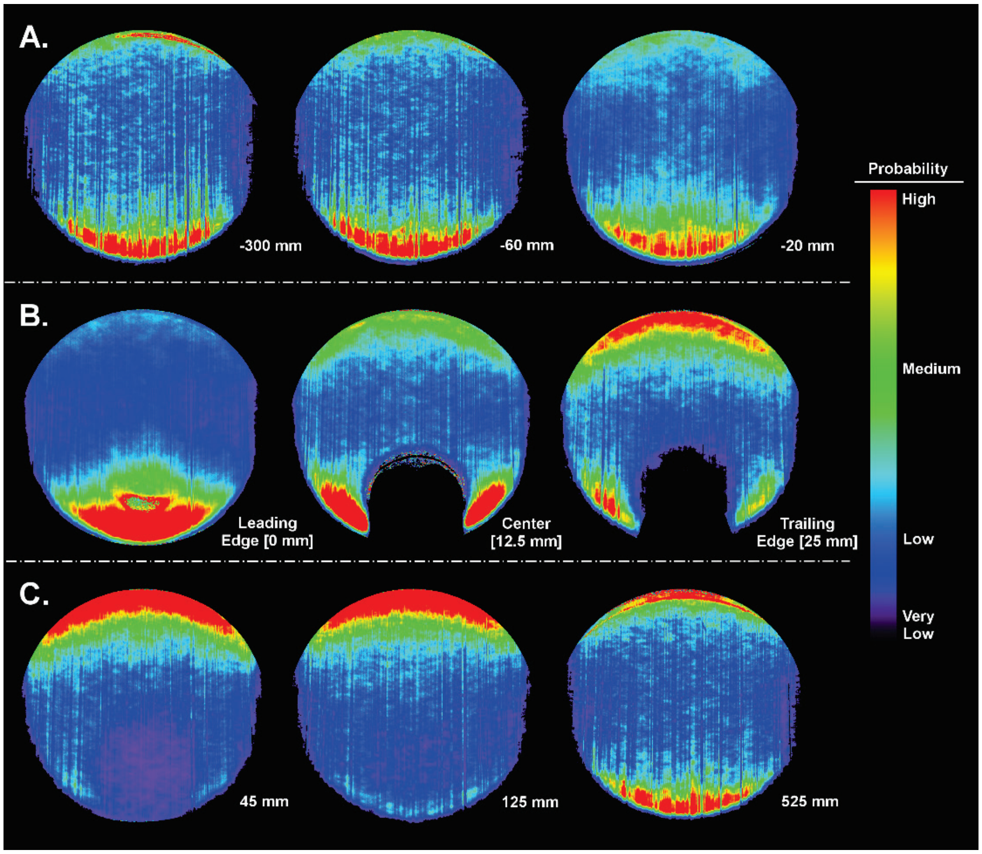

Figure 3.10: Particle Occurrence Probability Density Maps. (A) Cross-sections upstream of the sphere's leading edge; (B) Cross-sections around the sphere; (C) Cross-sections downstream of the sphere's trailing edge.

3.3.2 Centroid of the Particle Occurrence Probability Density Maps

The previously acquired maps provide a qualitative visual interpretation of the flow characteristics. Additionally, the data contained in the maps was used to perform a quantitative analysis of the occurrence of wheat particles. The centroid of the particle occurrence probability density map was calculated using Equation 3.3 for each location. The resulting pixel location of the centroid was converted into a distance in millimeters from the bottom of the conveying tube as shown in Figure 3.11. The axial profile shows the average distribution of the particles at each test location along the conveying line. It can be seen that the upstream cross-sections have a centroid that is below the centre line of the conveying pipe. The sphere causes a quick drop in the vertical centroid due to stagnant particles being trapped against the sphere. For the rest of the cross-sections, the sphere causes a noticeable vertical increase in the centroid location. This slowly returns to within 3 mm of the starting value 525 mm downstream of the leading edge.

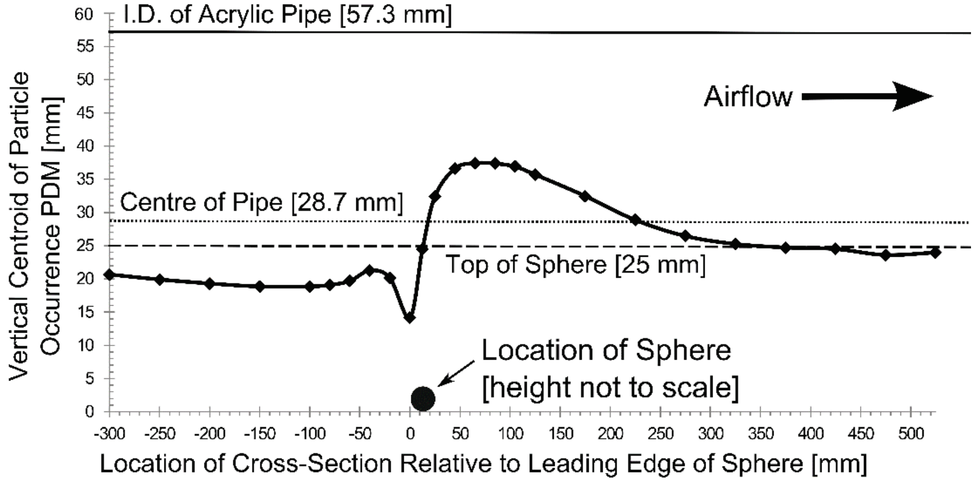

Figure 3.11: Vertical centroids of particle occurrence PDM at varying cross-section locations. Negative horizontal distances indicate a location ahead of obstruction.

3.4 CONCLUSIONS

An optical flow profiling method and associated apparatus were developed and tested for exploring the effect of obstructions or modifiers on pneumatic conveying system behavior. The specific test case was wheat particles in a conveying system similar to that used in commercial air seeders. The flow profiles were qualitatively useful in assessing the flow behavior in addition to being quantitatively used to determine the Centroid of the Particle Occurrence PDM which enabled the visualization of the flow's axial profile.

It was concluded that the addition of a noticeable flow obstruction could be fully explored and visualized. This method will be used for future pneumatic conveying research in tandem with more conventional pressure and velocity measurements.

After successfully designing, building and implementing an optical flow profiling system the following recommendations are put forward for future work.

- Develop and implement a traditional Particle Tracking Velocimetry system using the mechanical and imaging platforms developed in this work. This would provide additional data that will be useful in further studies.
- Continue to work on quantifying and improving the positional accuracy of the imaging system.

CHAPTER 4: GAS EXTRACTION FOR ENABLING DIFFERENT ENTRAINMENT AND CONVEYING VELOCITIES IN A PNEUMATIC CONVEYING SYSTEM

Using the optical flow profiling method that was outlined in the previous chapter a gas extraction system was explored. To enable flexible conveying at two separate velocities (entrainment and conveying) a gas extraction velocity reducer was designed, built, and tested.

This paper was co-authored by Dr. Scott D. Noble.

Design, preliminary analysis, and construction of the gas extraction system was undertaken by the author of this thesis under Dr. Noble's guidance. The body of the apparatus as well as the butterfly valve was 3D printed in College of Engineering shops while I fabricated the other components. I preformed all data collection and analysis and wrote the manuscript. Dr. Noble proposed revisions and edited the manuscript. This chapter is not currently being submitted to any journal but the original proof of concept method was published in the proceedings of the 24th Canadian Congress of Applied Mechanics, CANCAM 2013.

Keep, T. and Noble, SD. 2013. Exploration of Product Flow Behavior and Entrainment through Downstream Velocity Reduction. Proceedings of CANCAM 2013-the 24th Canadian Congress of Applied Mechanics. Saskatoon, Saskatchewan.

GAS EXTRACTION FOR ENABLING DIFFERENT ENTRAINMENT AND CONVEYING VELOCITIES IN A PNEUMATIC CONVEYING SYSTEM

Tyrone Keep and Scott D. Noble

Department of Mechanical Engineering, University of Saskatchewan, Saskatoon, Saskatchewan, Canada S7N 5A9

e-mail: tyrone.keep@usask.ca, scott.noble@usask.ca

ABSTRACT

Agricultural products are commonly conveyed in pneumatic, dilute phase systems. While there are power and product quality drawbacks, dilute phase conveying systems are required for many applications. The velocity of the conveying fluid plays has a negative role in both of these effects and as such, methods for reliably conveying a given mass of product at a lower velocity are desired. One such method to explore the effect of entraining wheat seeds at a high initial velocity and enabling the reduction of the conveying velocity downstream was developed and tested. This method required a set amount of air volume to be vented and measured, which in turn reduced the air velocity downstream of the device. Additionally, a flow visualization method was used to determine the centre of mass of the conveyed particles at varying locations to quantify the effect of the velocity changes on the entrainment of the particle.

It was determined that reducing the downstream velocity had a negligible effect on the centre of mass directly downstream of the velocity reducer for many operation conditions but had a larger effect further downstream. This implies that once the particles were fully entrained at a higher upstream velocity, they can be conveyed at a lower velocity for short distances. Also, an increase in the particles' entrainment level occurred due to the insertion of the velocity reducer which indicates that the effect of this method is not negligible and will need to be accounted for in future work.

Keywords: air seeder; pneumatic conveying; imaging; seed transport; dilute phase flow; gas extraction; conveying velocity; minimum conveying velocity; entrainment;

4.1 INTRODUCTION

Dilute-phase pneumatic conveying of granular materials is commonly used in the agricultural industry. Seeding equipment and grain vacuums are examples of this, where the flexibility of positioning and inlet/outlet combination are key advantages of the approach.

The disadvantages of conveying in the dilute flow regime include higher power per unit mass conveyed (Barbosa and Seleghim Jr. 2003), accelerated pipe wear, and product damage due to the higher conveying velocities (Klinzing, Rizk et al. 2010).

Despite wide usage of dilute-phase pneumatic conveying in industry, agricultural product entrainment and conveying is not well understood or documented. This is particularly true of cases where fully developed flow cannot be assumed. To explore the conveying characteristics of agricultural products, the minimum conveying velocity, also referred to as the saltation velocity, needs to be known. While there are ample data in the literature (Cabrejos and Klinzing 1994, Hubert and Kalman 2003, Hubert and Kalman 2004, Kalman, Satran et al. 2005) for materials such as glass, plastic, and metal spheres, little information has been published on the types of biological materials that pertain to this project. Specifically, the interaction between conveying velocity, product flow rate, and entrainment is of interest for agricultural particles which have a large Stokes number.

There are two common methods for determining the minimum conveying air velocity. The first method consists of metering a constant mass flow rate of product into an initially high-velocity air stream, and gradually reducing the overall system velocity until saltation occurs (Cabrejos and Klinzing 1994, Cabrejos and Klinzing 1994). The second method meters product into an air stream below the minimum conveying velocity and the distance the product travels from the feed point until they fall out of suspension and become stationary is measured (Hubert and Kalman 2003). This is repeated at various carrying velocities and a saltation length vs. gas velocity curve is developed, where the saltation length becomes asymptotic at the minimum conveying velocity. While these methods accurately describe the minimum conveying velocity in their respective systems, the same method might not directly apply to agricultural conveying systems where steady state conveying is typically not reached due to short straight runs, use of flexible hose, and lower operating pressures.

Rinoshika and Suzuki (2010) explored the use of a dune-shaped flow modification device that was inserted after product induction that reduced the minimum conveying velocity and the conveying power. While the exact reason the device worked was not fully explored, it was hypothesized to alter the particles entrainment level through a localized velocity increase, particle impact, and/or an increase in mixing forces. To further investigate the operating parameters and the entrainment characteristics of agricultural products in this work, the role of velocity needed to be explored. Therefore, it was hypothesised that the initial upstream velocity has no impact on downstream conveying and particle entrainment levels when operated at another, lower, velocity.

To test the hypothesis, the system must be able to operate at two separate velocities. A higher velocity entrainment zone (upstream) with the ability to operate the rest of the system or conveying zone (downstream) at the same or lower velocity.

There are two options to achieve this that often appear in literature: a stepped diameter conveying line, or air extraction. A stepped pipe configuration is commonly used in industrial conveying to maintain a constant velocity over long distances. If the diameter of the pipe was not periodically increased, the gas velocity would constantly increase due to gas expansion (Marjanovic, Levy et al. 1999, Wypych 1999). Maintaining a constant, minimal velocity is critical in reducing pipe wear, minimizing product damage, and sustaining a constant mass flow ratio of product at the receiving end of the system (Mills 2004, Klinzing, Rizk et al. 2010). Air extraction accomplishes the same end goal but instead of increasing the area of the conveying line, air volume is directly bled off, which causes a proportional decrease in superficial conveying velocity (Link, Jama et al. 2000, Mills 2006). This method is proposed as an alternative to stepped pipe installations for experimental purposes with benefits that include: flexibility in choosing downstream velocity, ease of measurement of downstream velocity by calculating volume of gas extracted, simplified system design, and the ease of retrofitting existing systems (Klinzing and Dhodapkar 1993, Link, Jama et al. 2000).

A method of gas extraction for reducing air velocity downstream of product entrainment was developed for use in testing the hypothesis and exploring the entrainment level of the particles (Keep and Noble 2013). This velocity reducer was used to bleed off a measured flow rate of air from the conveying line, thereby lowering the conveying air velocity while keeping the products in suspension in the main conveying line. This paper will briefly describe the preliminary testing of the velocity reducer before focusing on the final implementation and its effect on the entrainment of conveyed particles.

4.2 METHODS AND MATERIALS

A velocity reducing apparatus was designed and prototyped for use in exploring the effect of varying the upstream and downstream velocities on the conveying quality and entrainment level of agricultural materials.

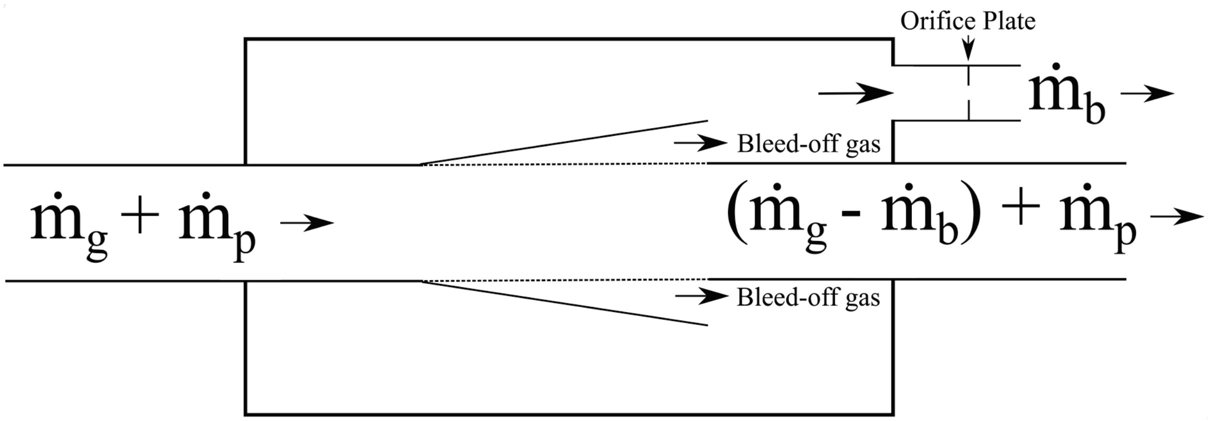

Figure 4.1: Velocity reducer schematic. Air is bled off from the screened section and is measured with a calibrated orifice plate and then vented to atmosphere. Where $\dot{m}_g$=gas mass flow rate, $\dot{m}_p$=particle mass flow rate, and $\dot{m}_b$=bleed-off gas mass flow rate.

A schematic of the velocity reducer is shown in Figure 4.1. The mass flow rate of the conveying gas and the particles being conveyed enter from the left (indicated by $\dot{m}_g$ and $\dot{m}_p$ respectively) and a portion of the conveying gas is bled off in a screened section ($\dot{m}_b$) and rerouted vertically in this image to be measured by an orifice plate. The remaining air and all the particles exit on the left.

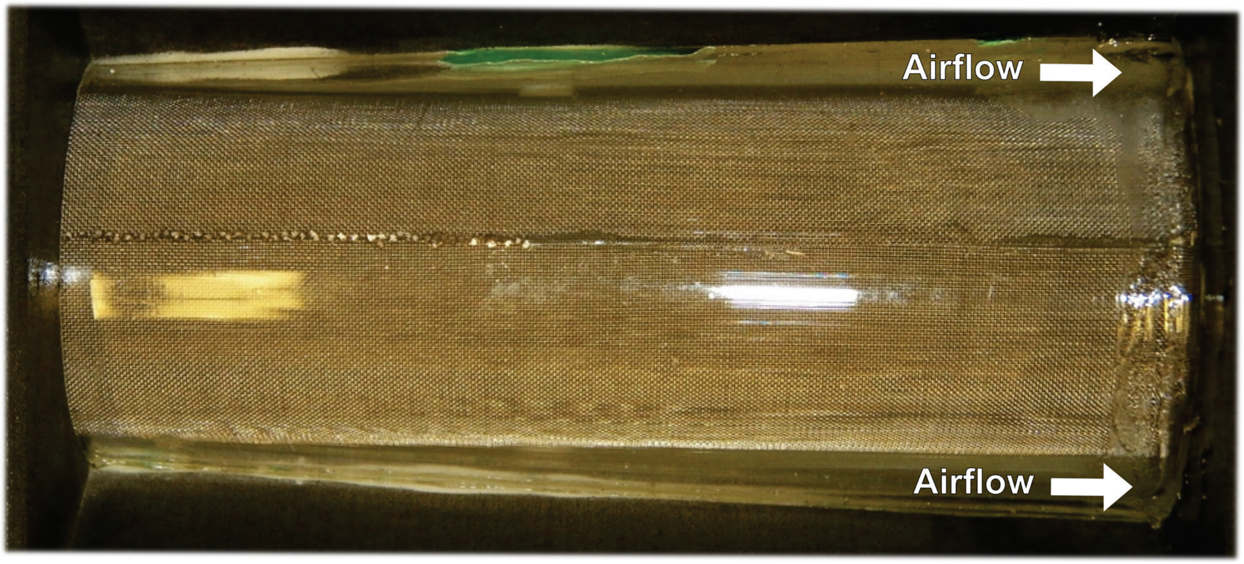

Figure 4.2: Close up of the window in the Velocity Reducer with the rolled screen in the background. Note gap between the screen and the reducer wall for bleed-off air.

A rolled mesh screen (Figure 4.2) was inserted into the centre section to retain the particles in the main conveying line. The top piece has a cut-out into which an acrylic window was fitted to allow for particle observation. Conveying air is bled off over the length of this screened section and then rerouted through the outer wings on the way to the wye collector and exhaust pipe (Figure 4.3).

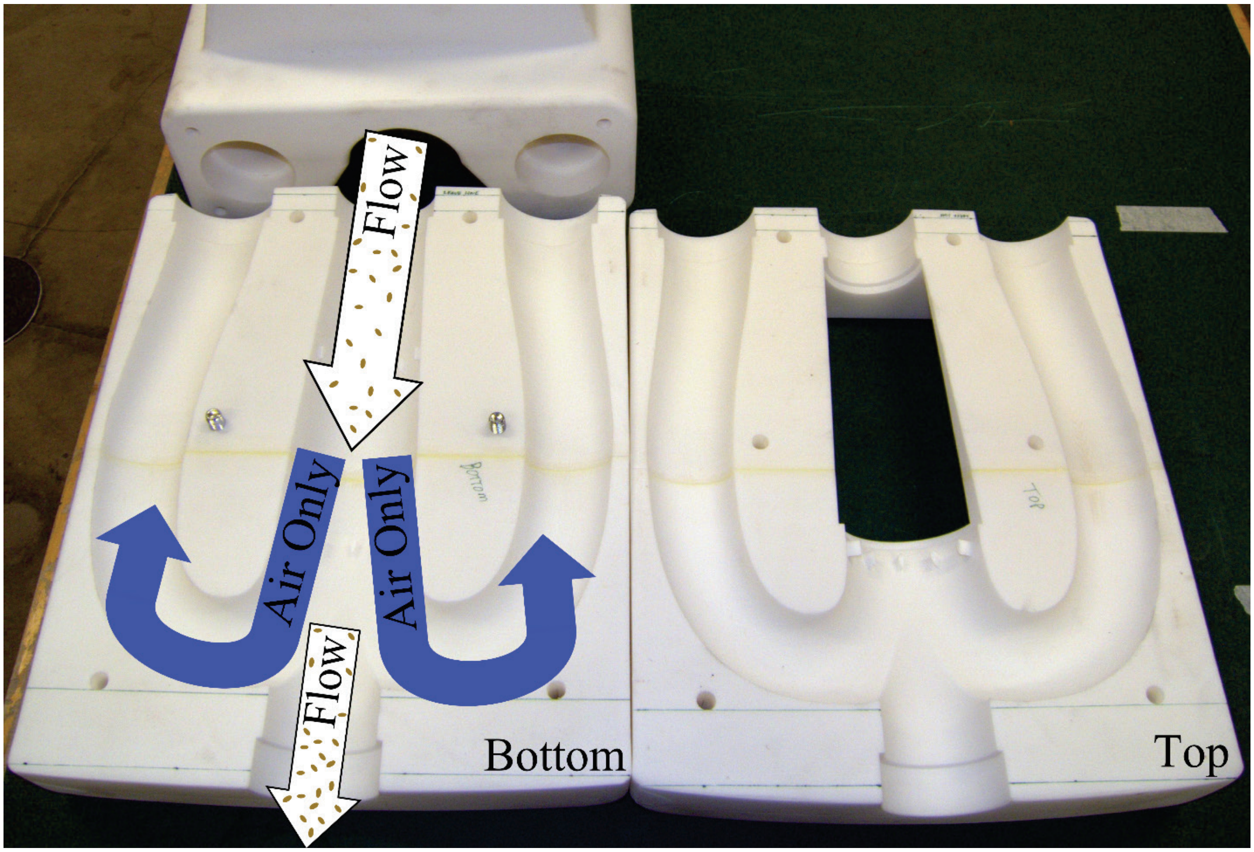

Figure 4.3: Velocity Reducer before assembly and insertion of screen/viewing window. Air is bled off around the outer two wings and is combined in the wye collector (chimney at rear of image) where it is routed to the orifice plate to measure the air flow.

The downstream portion of the initial implementation of the velocity reducer is shown in Figure 4.4. This includes the exhaust piping, bleed-air orifice plate, preliminary velocity reducer assembly, and the first iteration of the optical flow profiling apparatus for studying entrainment is in the foreground. This configuration was used as a proof of concept test for gas. The flow rate of exhausted air was measured through the use of a calibrated orifice plate and pressure transducers. The change in pressure was less than 10 kPa over the system and the air is assumed to behave as an ideal gas due to very low air velocities (≈Mach 0.09). This volume was then used in conjunction with the measured upstream velocity to calculate the remaining air velocity in the downstream conveying line.

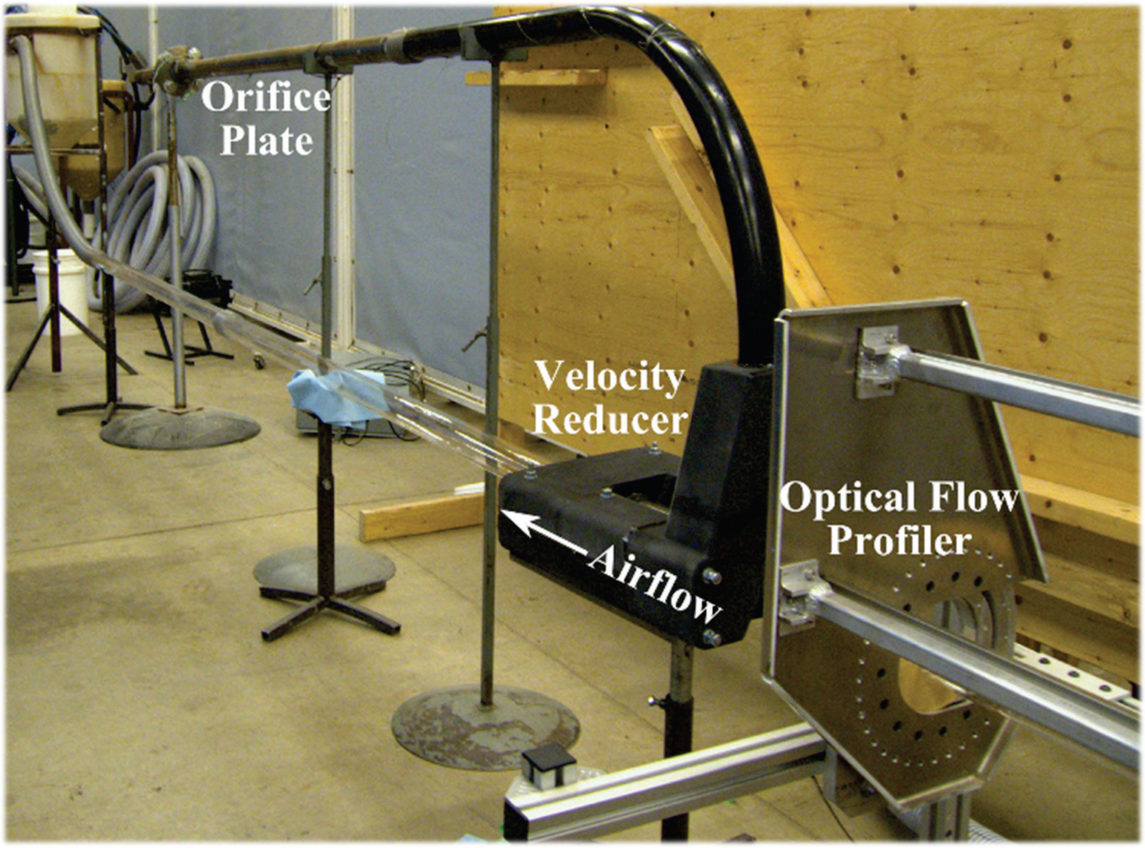

Figure 4.4: Velocity Reducer as oriented during preliminary testing.

The velocity reducer system worked as intended, but the desired differential between upstream and downstream velocity was not attainable using the horizontal and passive gas extraction line. Therefore, the system needed to be further developed to include a powered exhaust vent to achieve a greater velocity differential between the upstream and downstream sections.

Figure 4.5 shows a schematic of the velocity reducer with the powered gas extraction system. A vertical orientation was chosen to simplify the lab layout as well as remove one 90^o bend. The bleed-off air is routed through the reducer in the same manner as the previous iteration but the powered vent and the vertical orientation allowed a larger volume of air to be extracted, which in turn created a lower downstream air velocity. The refined system included an automated servo-motor controlled butterfly valve to adjust the air velocity. The control loop used an orifice plate to measure the volume of air that was bled off, which was then subtracted from the measured upstream flow rate to determine the downstream velocity.

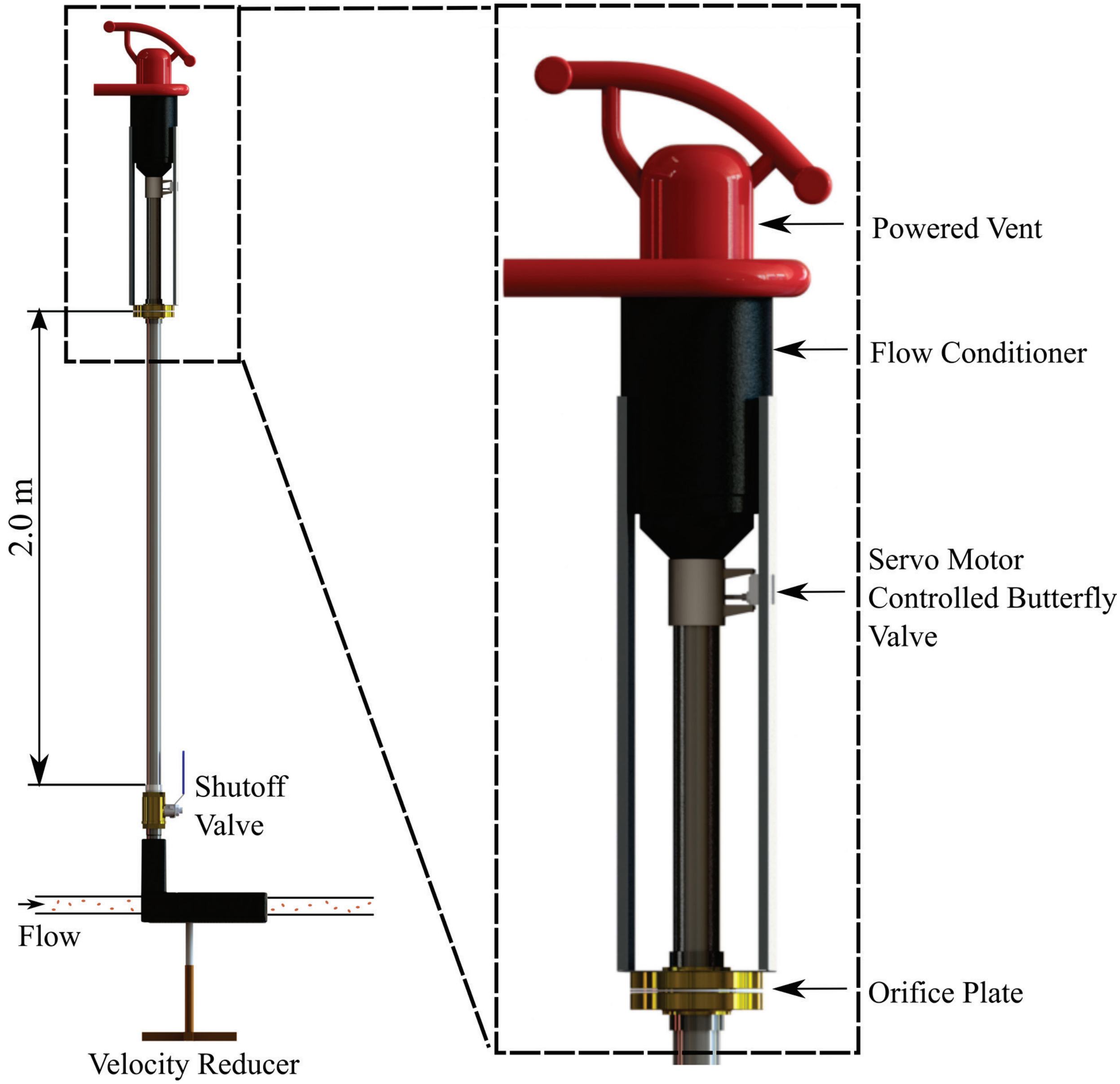

Figure 4.5: Velocity Reducer with Power Vent

All conditions were tested using a dilute phase conveying system that is shown in Figure 4.6. The prime mover consisted a centrifugal fan powered by a 5 HP, three-phase motor and variable frequency drive. It also included a venturi velocity meter section, wye splitter and shut-off valves, upstream entrainment section, grain cart and metering system, downstream conveying section, imaging system, and product collection bin. To investigate the impact of the velocity reducing apparatus on particle flow and entrainment an optical flow profiling imager was used (Keep and Noble 2015).

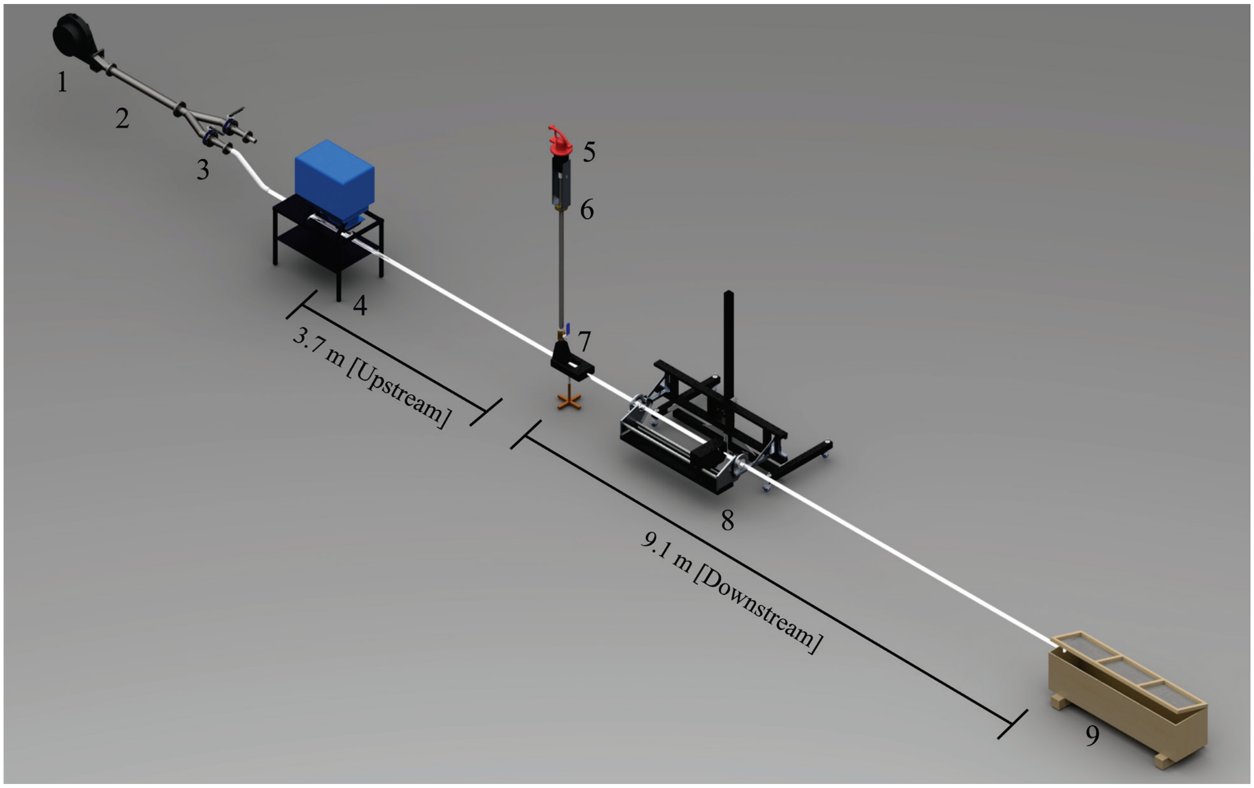

Figure 4.6: Bird's-eye view of the conveying system with the optical flow profiling apparatus downstream of the velocity reducer. [1: Centrifugal Fan, 2: Upstream Venturi, 3: Wye-Splitter, 4: Air Cart and Metering System, 5: Powered Vent, 6: Orifice Plate, 7: Velocity Reducer, 8: Optical Flow Profiler, and 9: Product Collection Box.]

4.3 RESULTS AND DISCUSSION

The effect of implementing a gas extraction system to reduce conveying velocity downstream of product induction was be explored in two parts: (1) a velocity reducing system and apparatus used without gas being extracted and (2) the final implementation of a powered gas extraction system.

4.3.1 Impact of the Velocity Reducer Without Gas Extraction

To test the effect of adding the velocity reducer to the pneumatic conveying system, the entrainment level was compared upstream of the velocity reducer (Condition 1), and 300 cm downstream of the velocity reducer location with the velocity reducer inserted (Condition 2) or an equivalent length of acrylic tubing in its place (Condition 3). These conditions are illustrated alongside the results in Figure 4.8. The tests were performed with a wheat mass flow rate of 0.088 kg/s and a superficial air velocity that ranged from 14 to 24 m/s in increments of 2 m/s. Conditions

1 and 3 consisted of three randomized trials of each air velocity. Condition 2 consisted of two randomized trials of each velocity; the third trial was removed due to a system positioning error.

Using the flow profiling system described by Keep and Noble (2015), the cross-sectional particle distributions were recorded and centre of mass (C.o.M.) calculated for each condition and trial. These C.o.M. trials are plotted in Figure 4.8. A linear correlation was observed between the centre of product distribution and the system velocity for Conditions 1 and 2 (with the velocity reducer in the system but not bleeding off air-flow). The centres of the distributions ranged from approximately 24 mm to 7 mm for Condition 1 and approximately 15 mm to 6 mm for Condition 2. Condition 2 was lower than Condition 1 as the particles tended to settle out the further they travel from the metering system.

Distributions for Condition 3 had a lower centre of mass than either 1 or 2. The centre of mass of condition 3 also displayed a non-linear trend with the overall system velocity. This could be attributed to effects introduced by the velocity reducer and/or the product separation screen that appear to encourage product entrainment in the air stream for longer distances. Figure 4.7 shows a cross-section of the acrylic conveying line with inner and outer diameters noted. An example location of the vertical Centre of Mass (C.o.M.) in mm measured from the inside bottom wall of the conveying pipe is shown.

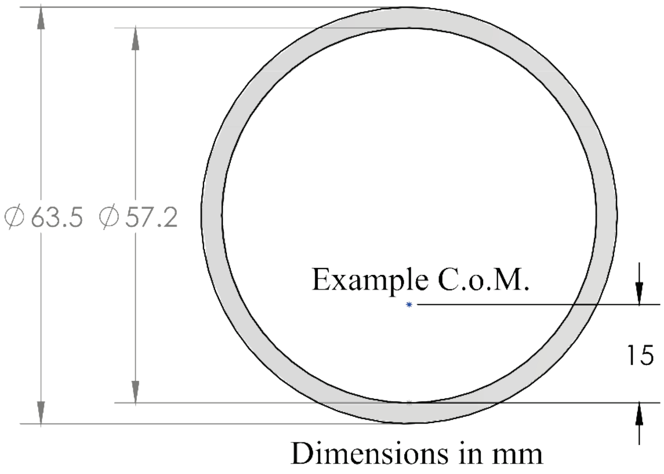

Figure 4.7: Cross-section of the conveying line with an example centre of mass shown. The C.o.M. is noted as a distance in mm from the bottom of the conveying line.

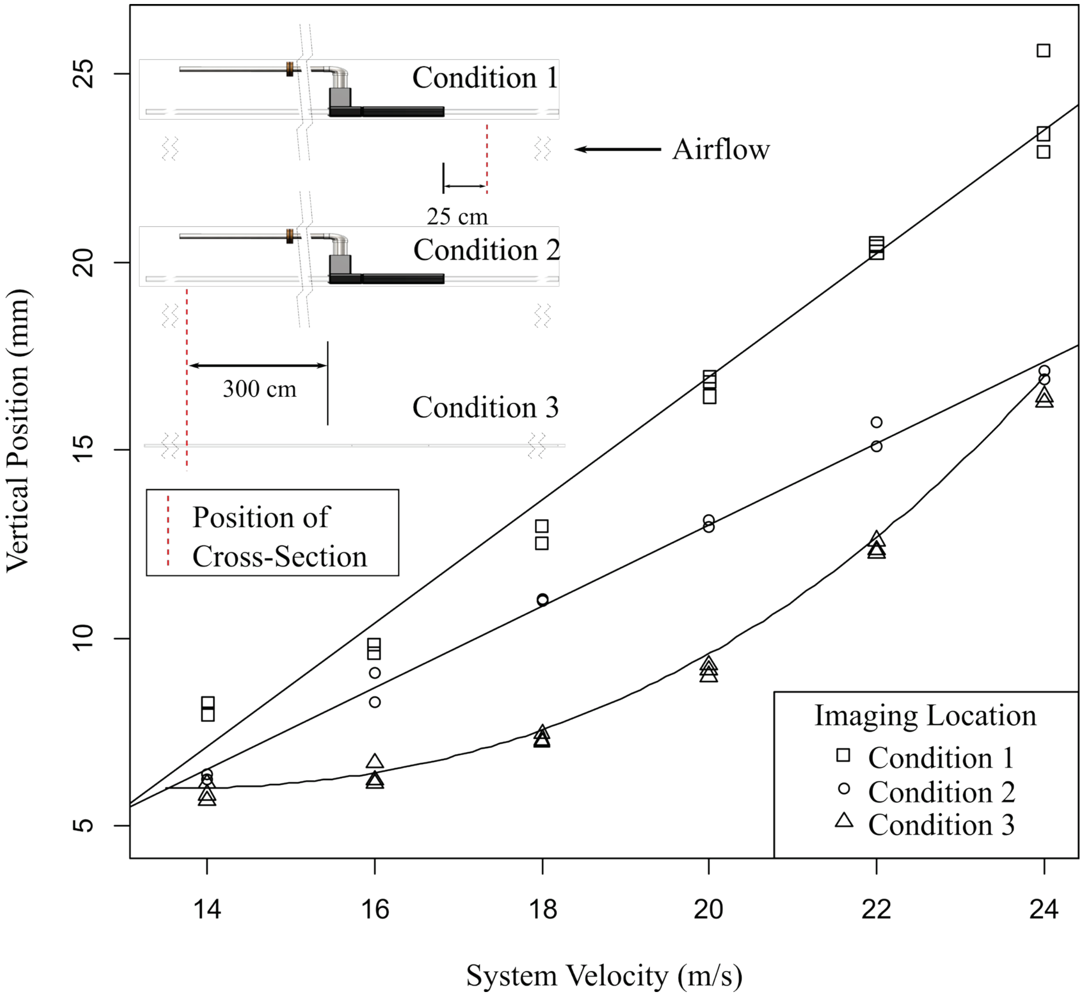

Figure 4.8: Centre of Mass of product distribution for all Conditions at set system velocities ranging from 14-24 m/s. No air bled off through velocity reducer.

4.3.2 Impact of Gas Extraction on Entrainment

A similar set of experiments were completed using the same imaging method as described above with the velocity reducer removing air from the conveying stream. The centre of mass of the particle distribution was calculated using the optical flow profiling method of Keep and Noble (2015) at various locations along the conveying system. Wheat seed mass flow rates of 0.0205, 0.0620, and 0.1020 kg/s (which correspond to meter roller speeds of 10, 30, and 50 RPM on this system) were tested. Upstream conveying velocities of 30, 25, 20, 18, 16, and 14 m/s were the starting point for varying the downstream velocity. At each upstream velocity set point, the downstream velocity was set at a variety of set points by bleeding off air volume as shown in Table 4.1

To simplify comparisons across conveying velocities and product flow rates, the mass loading ratio ϕ (also known as the mass flow ratio and is sometimes denoted as μ in some literature) was calculated as:

$$\phi = \frac{\dot{m}_p}{\dot{m}_f} \tag{4.1}$$

where

$\dot{m}_p$ is the mass flow rate of the solid (wheat) and

$\dot{m}_f$ is the mass flow rate of the fluid (conveying air).

Table 4.1: Gas Bleed-off test conditions

Upstream Velocity [m/s] ± 0.05	**Downstream Velocity [m/s] ± 0.05 ***	**ϕ at 0.0205 kg/s $\phi \pm 0.001$**	**ϕ at 0.0620 kg/s $\phi \pm 0.001$**	**ϕ at 0.1020 kg/s $\phi \pm 0.001$**
30	30	0.22	0.66	1.09
	25	0.26	0.80	1.31
	20	0.33	1.00	1.64
	15	0.44	1.33	2.19
	10	0.66	1.99	3.28
25	25	0.26	0.80	1.31
	20	0.33	1.00	1.64
	15	0.44	1.33	2.19
	10	0.66	1.99	3.28
	5	1.32	3.99	6.56
20	20	0.33	1.00	1.64
	15	0.44	1.33	2.19
	10	0.66	1.99	3.28
	5	1.32	3.99	6.56
18	18	0.37	1.11	1.82
	16	0.41	1.25	2.05
	14	0.47	1.42	2.34
	12	0.55	1.66	2.73
	10	0.66	1.99	3.28
	8	0.82	2.49	4.10
	6	1.10	3.32	5.47
16	16	0.41	1.25	2.05
	14	0.47	1.42	2.34
	12	0.55	1.66	2.73
	10	0.66	1.99	3.28
	8	0.82	2.49	4.10
14	14	0.47	1.42	2.34
	12	0.55	1.66	2.73
	10	0.66	1.99	3.28

** Variation in the downstream velocity depended on operating conditions and potential for plugging. Even with the powered vent the amount of air bled off was not large enough to achieve all downstream velocities for all upstream conditions.*

The centre of mass for five different locations were calculated. These imaging locations are shown in Figure 4.9 relative to the velocity reducer.

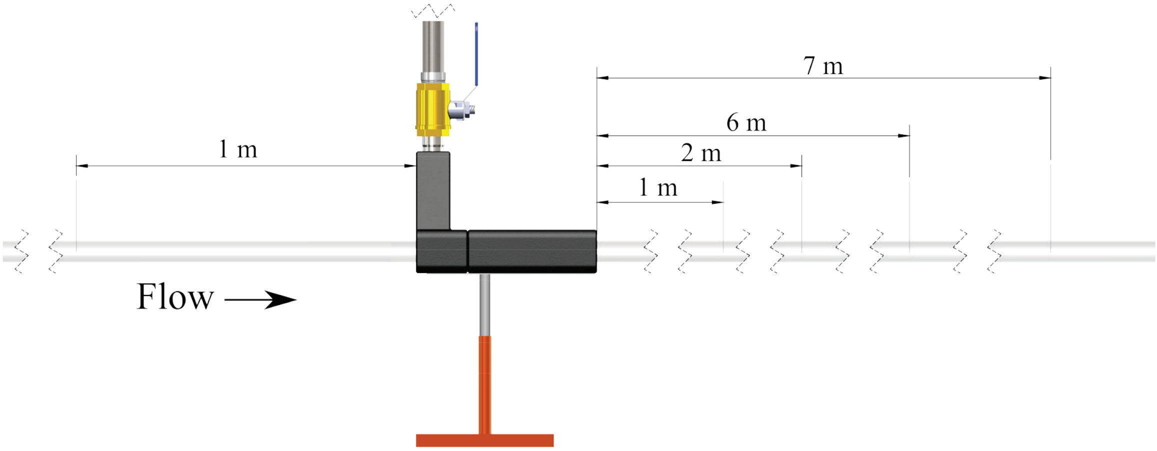

Figure 4.9: Imaging locations, referenced to the velocity reducer, where the particle centre of mass images were collected.

Figures 4.10 to 4.15 show a plot of the vertical C.o.M. in mm at varying values of ϕ for the three experimental solid mass flow rates with respect to the downstream mass loading ratio. In each upstream velocity series, the mass flow ratio had an inverse relationship to the downstream conveying velocity. As the mass flow rate increased, the system was unable to convey product at some of the lower upstream/downstream velocity conditions and as such data for these combinations could not be captured.

The data used to create Figure 4.10 were obtained one metre upstream of the velocity reducer. As expected, the reduction in downstream velocity did not significantly affect the centre of mass. The lower upstream velocities at the two higher mass flow rates did not fully entrain the particles before reaching the imaging plane. This resulted in some slug flow and piling in the bottom of the pipe which was the cause of the higher centre of mass for the lower upstream velocities and higher product rates when compared to the 0.0205 kg/s trials.

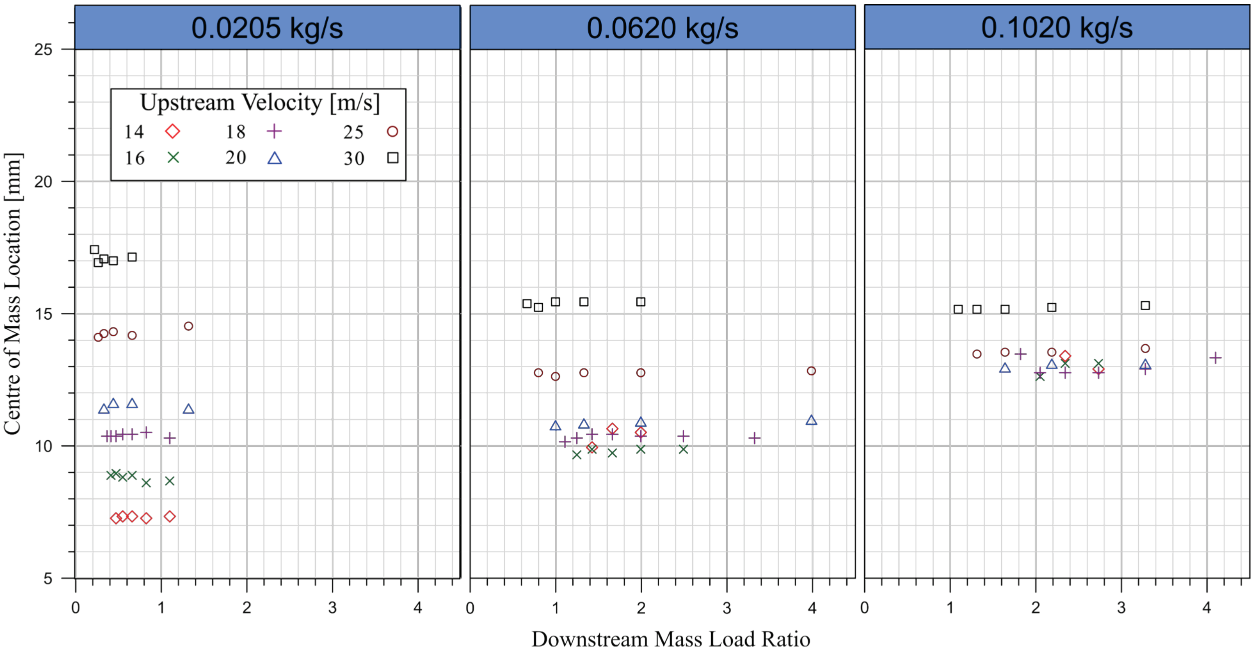

Figure 4.10: Centre of Mass acquired one metre upstream of velocity reduction

Flow profile and C.o.M. data were obtained one metre downstream of the velocity reducer. These data were plotted in Figure 4.11 and changes in the centre of mass were observed. Most noticeably the C.o.M. was higher for all conditions as compared to one metre upstream. This indicated that the insertion of the velocity reducer and/or product separation screen increased the entrainment level of the conveyed particles. Comparing 20 m/s upstream and downstream of velocity reduction for example gives a difference in C.o.M. of about 5mm. At the same velocity the test outlined in Figure 4.8 (with and without the velocity reducer) gives approximately the same change in C.o.M. From this it would appear that just the addition of the velocity reducer gives an increase in C.o.M. of a similar magnitude as reducing the velocity through gas extraction. Additionally, a slight reduction in C.o.M. occurred as more air volume was bled off (higher ϕ due to lower downstream velocity).

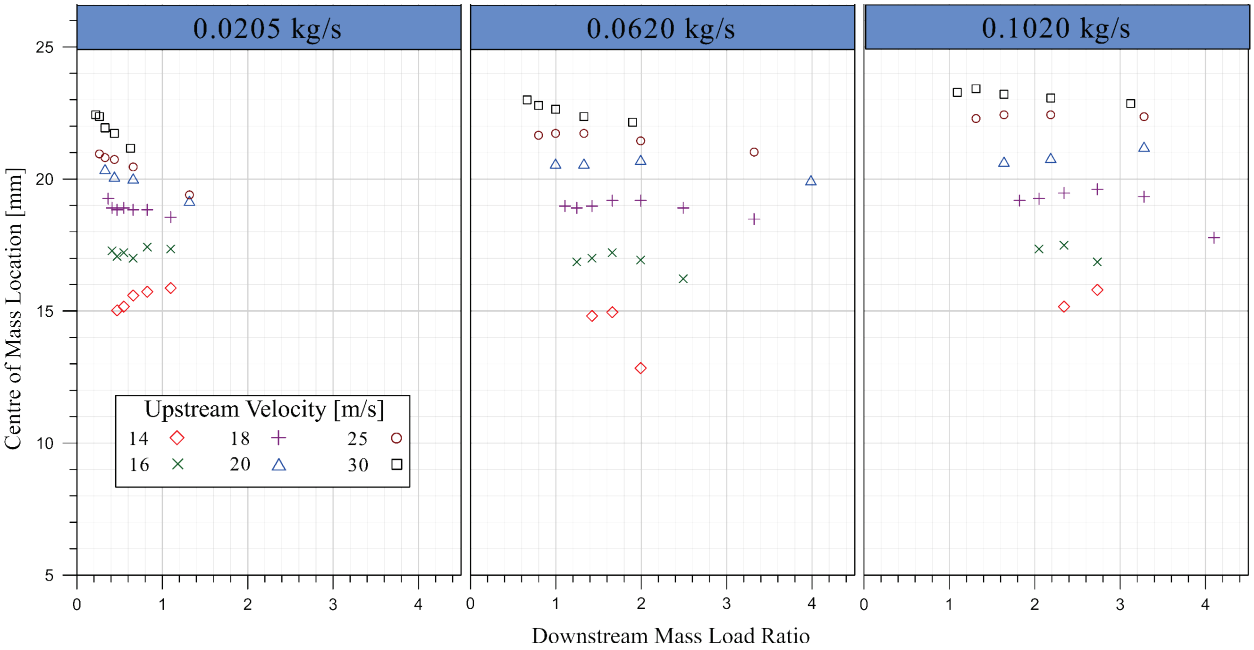

Figure 4.11: Centre of Mass as imaged one metre downstream of velocity reduction

Images were obtained two metres downstream of the velocity reducer and the results are shown in Figure 4.12. The general behavior is similar to those from one metre downstream, but the centre of mass is lower. This indicates that the particles obtain a boost to their entrainment level after the velocity reducer. This effect peaks somewhere between the reducer and this test location.

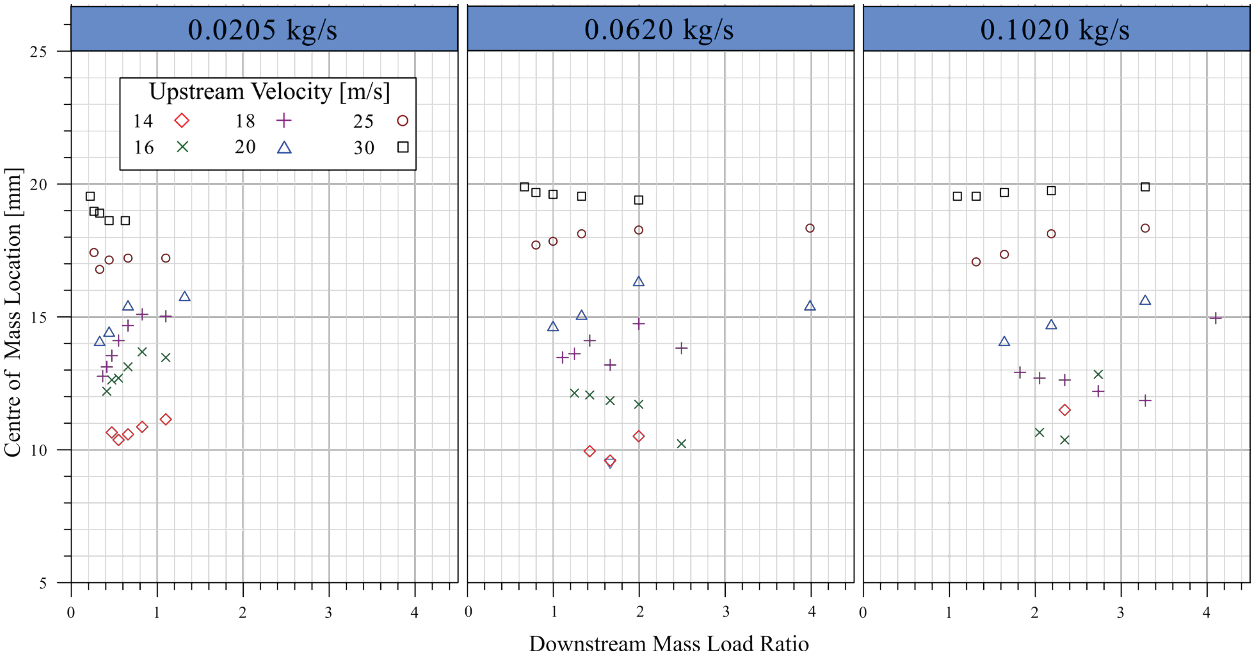

Figure 4.12: Centre of Mass taken two metres downstream of velocity reduction

An interesting trend between the vertical centre of mass and the downstream conveying velocity was seen for the three highest upstream velocities. The vertical position of the centre of mass was better correlated with upstream velocity than downstream velocity. This suggested that if the product was entrained at a high initial velocity, it could then be conveyed downstream at a much lower velocity with minimal effect on the distribution centroid. While data were limited, lower initial entrainment velocities did not appear to afford the same advantage to lower downstream velocities.

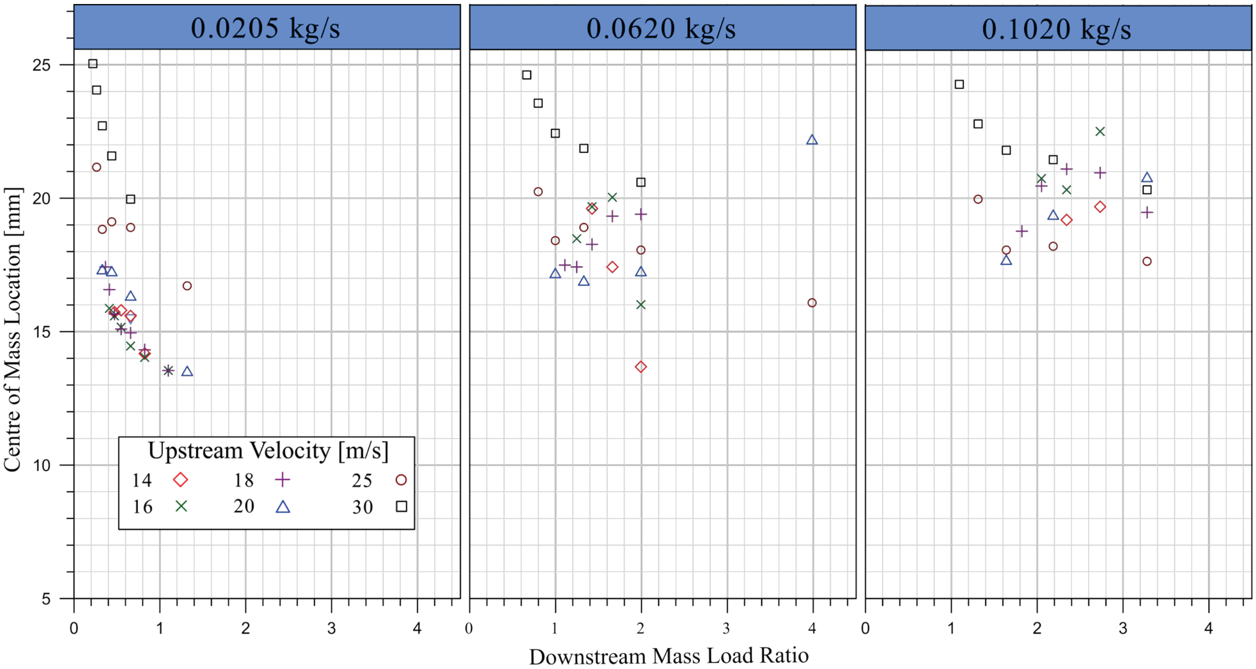

Figure 4.13: Centre of Mass imaged six metres downstream of velocity reduction

Data for Figure 4.13 and Figure 4.14 were taken at six and seven metres downstream respectively. As the velocity was lowered the centre of mass dropped off quickly for these locations. For higher bleed-off rates the entrainment of the particles was very low with the majority of the product being conveyed along the bottom of the pipe. Additionally, many of the lower upstream velocity test conditions had some form of plugging taking place at these locations. Generally, a slugging flow would develop, and static dunes would form as the velocity was lowered. This is seen to a greater extent with the two higher product mass flow rates where some of the centres of mass (especially for lower downstream velocities) increased with increasing loading ratios due to the effect of the piling on the C.o.M. measurements.

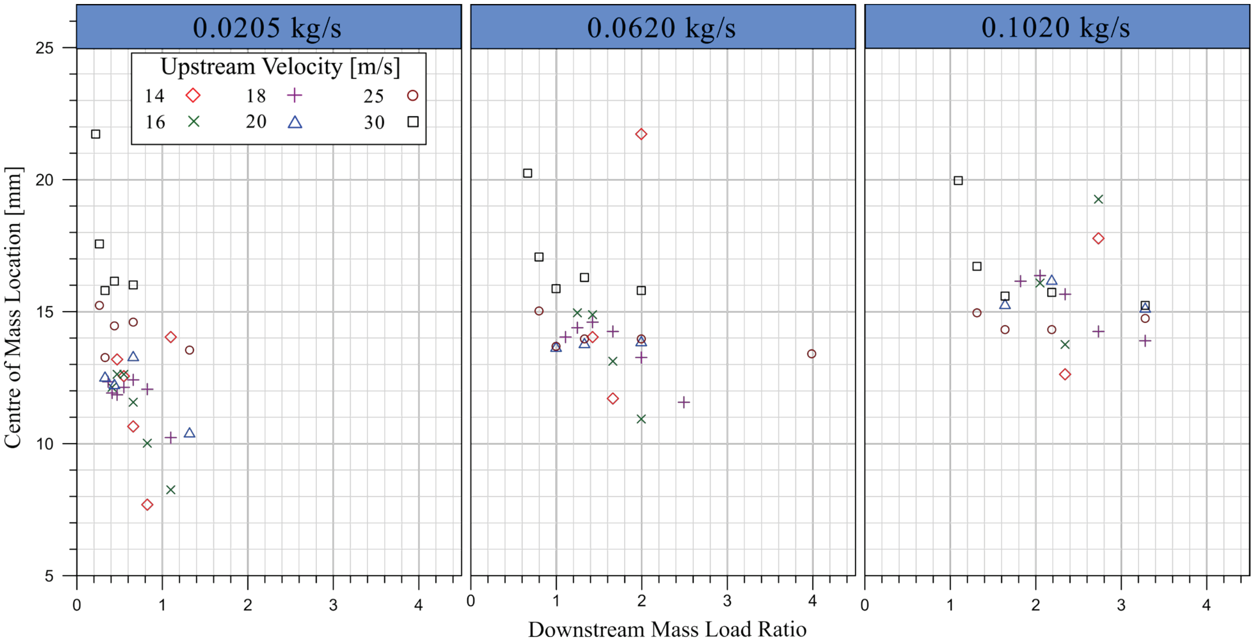

Figure 4.14: Centre of Mass seven metres downstream of velocity reduction

4.4 CONCLUSIONS

A functional velocity reducer was designed, built, and tested to provide for downstream velocity reduction. The passive venting scenario did not allow for the desired range of use which lead to the implementation of a powered gas extraction system.

The reducer had a noticeable effect on the product entrainment versus the test conditions with no reducer apparatus installed. The addition of a screen and/or the effect of a large dead space around the screen when no air is bled off is hypothesized to have a small beneficial entrainment effect.

For many of the tested conditions, operating the system at the same downstream velocity but with two different entrainment velocities did have an affect on the centre of mass of the conveyed particles. Therefore, the hypothesis that upstream velocity has no effect on downstream conveying must be rejected as there was a difference in particle centre of mass between operating at an initially high entrainment velocity and then conveying at a lower velocity when compared to operating the entire system at this lower velocity.

4.5 RECOMMENDATIONS

After successfully designing, building, implementing a velocity reducing apparatus, the following recommendations are put forward for future work.

- Further testing to quantify the effect of the velocity reducer should be undertaken and any future use of the velocity reducer should take this effect into account
- Further explore the effect of a velocity reduction downstream of an initially higher local velocity
- While entraining at an initially high velocity and conveying at a lower velocity does change the centre of mass of the conveyed particles there is a breaking point where this is no longer the case. This is likely correlated with the minimum conveying velocity of the particles but more work needs to be done to confirm this hypothesis.

CHAPTER 5: THE EFFECT OF VARYING ENTRAINMENT AND CONVEYING VELOCITY ON SPECIFIC PRESSURE DROP, ENERGY, AND PARTICLE ENTRAINMENT CHARACTERISTICS

To further explore the effect of gas extraction on particle entrainment characteristics, specifically the effect on pressure drop and conveying power, the gas extraction velocity reducer that was outlined in the previous chapter was used to collect pressure and velocity data.

Instrumentation and calibration of the air handling system was completed by myself with advice from Dr. Noble. I performed all data collection and analysis along with writing the manuscript. Dr. Noble provided editing and suggested content revisions.

THE EFFECT OF VARYING ENTRAINMENT AND CONVEYING VELOCITY ON SPECIFIC PRESSURE DROP, ENERGY, AND PARTICLE ENTRAINMENT CHARACTERISTICS

Tyrone Keep and Scott D. Noble

Department of Mechanical Engineering, University of Saskatchewan, Saskatoon, Saskatchewan, Canada S7N 5A9

e-mail: tyrone.keep@usask.ca, scott.noble@usask.ca

ABSTRACT

The effects of using different entrainment and conveying velocities for the dilute-phase pneumatic conveying of wheat were tested. Entrainment level, conveying quality, and energy required for transport were the primary comparison metrics. An air bleed-off system was used to create downstream conveying air velocities that were lower than the entrainment velocities. For non-vented conditions (velocity ratio=1) the system agreed with Gasterstadt's equation relating specific pressure drop and mass loading ratio along with the results of others including Cabrejos and Klinzing (1992). The K-value [slope] for the downstream conveying section was 0.17 with no air bleed-off. K-values decreased linearly with decreasing velocity ratios with a zero K-value occurring at a velocity ratio of 0.65.

When plotting specific pressure drop versus mass loading ratio, a slope of zero indicates that the pressure drop due to the air and the product is equal to the pressure drop of air only. This would occur when the slip velocity is near zero, meaning the product and conveying gas velocities are the same. Eventually the product would decelerate due to wall effects and other forces, but for short distance conveying these results indicate there is a stable set of velocity conditions that would not normally be attainable in a conventional pneumatic conveying system. Under these conditions, the product is accelerated over a small entrainment section and over a short conveying length there is potential for a net power savings.

Keywords: air seeder; pneumatic conveying; seed transport; dilute phase flow; gas extraction; minimum conveying velocity, specific pressure drop; mass loading ratio; specific energy; power

5.1 INTRODUCTION

Agricultural products such as seed and granular fertilizer are commonly transported using dilute-phase, low-pressure pneumatic conveying due to the flexibility of product placement and multiple inlet/outlet combinations. The conveyance of large particles in dilute-phase flow presents a unique set of challenges such as higher power required per unit mass, increased pipe wear, and greater product damage (Klinzing, Rizk et al. 2010). Agricultural products typically have an approximate equivalent diameter range of 1 to 10 mm, which is larger than most commonly conveyed products represented in the literature. Wheat seed was used in this work as it is a very common agricultural product that is of medium size.

A research group at Yamagata University have published multiple papers exploring the power and pressure relationships of large particles conveyed in the dilute phase while modifying the flow and/or entrainment characteristics of the particles (Rinoshika and Suzuki 2010, Yan and Rinoshika 2011, Yan, Rinoshika et al. 2012, Yan and Rinoshika 2013, Yan and Rinoshika 2013, Rinoshika 2014). One such method that showed substantial power savings was the insertion of a dune-shaped object just downstream of the product metering location. This object was able to reduce the power required for stable conveying by 34% and decreased the minimum conveying velocity by 19%.

The use of a similar device or process to enable comparable power savings is desired in an agricultural air-seeder. However, it is not clear why this device provided such substantial savings. In an attempt to explain this effect, the following hypotheses were developed:

- Increased velocity in the entrainment zone due to reduced cross-sectional area accelerates the particles to the steady state conveying velocity quickly and therefore allows the system to operate at a lower overall velocity (dune forms an eccentric venturi).
- The dune creates an upward mixing force that increases the entrainment level of the particles.
- Impact off the face of the dune launches the particle into a higher velocity portion of the flow with a trajectory that avoids impacts with the pipeline for greater distances, thereby facilitating entrainment and conveying.

In this work, the role of dissimilar air velocities in the upstream and downstream conveying sections of the pipeline was considered. The effect of this velocity difference was explored to determine its role on product entrainment level, pressure drop, and power consumption.

To simplify comparisons across conveying velocities and product flow rates, the mass loading ratio[2] was used. This is shown in Equation 5.1 where $\dot{m}_p$ and $\dot{m}_f$ are the mass flow rate of the particle (wheat) and the fluid (conveying gas) respectively.

$$\phi = \frac{\dot{m}_p}{\dot{m}_f} \tag{5.1}$$

Specific pressure drop (α) is the ratio of the pressure drop per unit length of the mixture of gas and solid (Δp_{s+g}) and the pressure drop per unit length of the gas only (Δp_g) at the same gas flow rate.

$$\alpha = \frac{\Delta p_{s+g}}{\Delta p_g} \tag{5.2}$$

Gasterstadt (1924) first proposed a link between specific pressure drop and the mass loading ratio. For developed flow and at equal superficial gas velocities (i.e. the same conditions both with and without product in the airflow), the specific pressure drop is related to the mass loading ratio by the following equation.

$$\alpha = K\phi + 1 \tag{5.3}$$

where α is the specific pressure drop,

ϕ is the mass loading ratio, and

K is the slope of the linear relationship.

In addition to the above parameters, this study requires a description of the relationship between entrainment and conveying velocity. The ratio of the downstream (conveying) to the upstream (entrainment) velocity, the velocity ratio (δ), is defined as:

$$\delta = \frac{Conveying\ Superficial\ Velocity}{Entrainment\ Superficial\ Velocity} \tag{5.4}$$

The results of Farbar (1949), Hinkle (1953), and Cabrejos and Klinzing (1992) were in agreement with Gasterstadt's original findings. Cabrejos and Klinzing (1992) used this relationship and the published data of those before them to propose a non-intrusive method to determine mass flow rates in fully accelerated horizontal conveying. The K-value varied between

---

[2] Sometimes called the mass flow ratio or the solids loading ratio and can be denoted as μ

datasets due to pipe diameter, system configuration (vertical or horizontal), particle properties, and pipe style but it can be determined for each conveying system and then used to predict mass flow rate of the product knowing the conveying gas velocity, so long as fully-developed flow can be assumed.

Figure 5.1 shows a sample of data from Cabrejos and Klinzing (1992) for 450 μm diameter glass beads conveyed in a 50 mm diameter pipe at various velocities. The data agreed well with Equation 5.3 and were used to develop a model that predicted the solid mass flow rate for other air velocities. The authors recommended the following two conditions for accurate prediction of mass flow rate using their developed model:

1) Fully developed flow is required and
2) Air velocity must be maintained at 50% above saltation velocity for the K-value to be independent of conveying gas velocity.

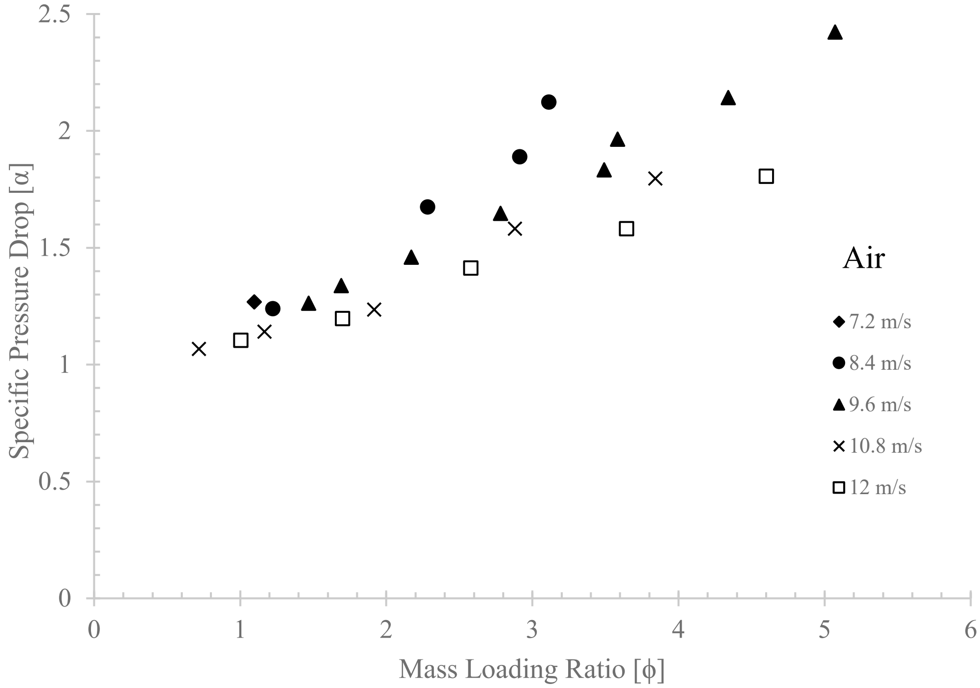

Figure 5.1: Specific pressure drop for glass beads (D=450 μm, ρ_p= 2480 kg/m^3 [type of density not given]) in a 50 mm I.D. horizontal conveying line. Adapted from Cabrejos and Klinzing (1992).

In the present case of varying entrainment and conveying velocities it was hypothesised that there would be differences from the standard Gasterstadt relationships. Additionally, a higher upstream velocity might increase the entrainment level of the product and therefore allow the system to be operated at a lower overall velocity. Working through the possible effects of having different entrainment and conveying velocities led to the following three hypothesized operating conditions:

1) A standard pneumatic conveying system where upstream and downstream superficial-velocities are equal. This would give a velocity ratio of one and would follow Gasterstadt's equation with a positive slope (K-Value) as demonstrated by many previous works and within the limits proposed by Cabrejos and Klinzing (1992). A generic case is shown as Line A in Figure 5.2.
2) A gas extraction system with a high entrainment velocity and a much lower conveying velocity. This would give a very small velocity ratio and was hypothesized to have a negative slope (K-Value) due to the difference between velocities being very large. The product would be going faster than the remaining conveying air and experience a significant negative drag force. This would act to resist the motion of these particles and slow them down. The relationship is shown as Line B in Figure 5.2.
3) Assuming continuous data there should be at least one condition between the two extremes where a slope (K-Value) of zero exists. (Line C in Figure 5.2). This would indicate a stable set of entrainment and conveying velocities where no extra pressure is required to convey the air plus product versus the air only case.

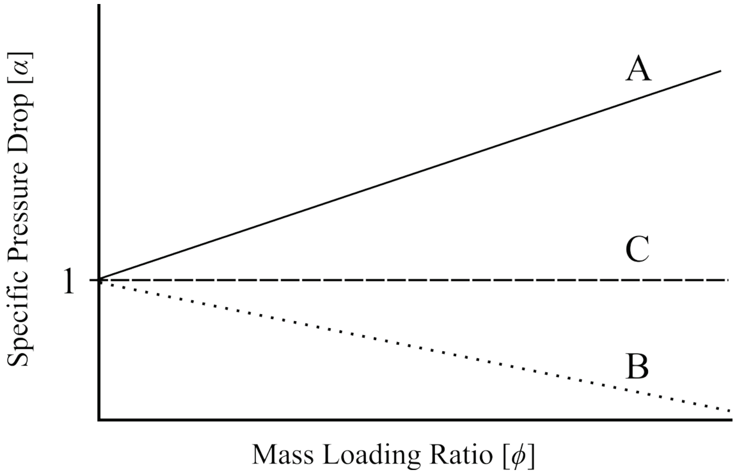

Figure 5.2: Generic relationship hypothesized between specific pressure drop and solids loading ratio at 3 different velocity ratios. $\delta_A=1$, $\delta_B<1$, and $\delta_A>\delta_C>\delta_B$.

5.2 METHODS AND MATERIALS

To explore the relationship between specific pressure drop and solids loading ratio, product needed to be metered into a conveying pipe at various mass flow rates with provisions for enabling differing air velocities in the entrainment (upstream) and conveying (downstream) zones of the pipeline.

To enable variation between upstream entrainment and downstream conveying velocity there are two feasible options: stepped conveying line and air extraction. Conveying systems with stepped pipe diameters are commonly used in industry to maintain velocities over very long (>100 m) conveying distances. A periodic increase in pipe diameter mitigates the increase in velocity due to gas expansion (Wypych 1999). Air extraction accomplishes the same goal by removing air from the system which reduces the conveying air velocity. The air extraction method was implemented in this work due to the following benefits: ease of measurement of downstream velocity (volumetric flow rate of gas extracted is known), simplified physical system design, and most importantly, flexibility in varying the velocity ratio.

In their previous work Keep and Noble (2015) used an air extraction and velocity reducing system was built and tested to explore the effect of entraining the particles at a higher velocity than in the downstream conveying section. The location of the conveyed particles in the air stream was quantified using the imaging system that was outlined in the previous chapters.

The conveying system was instrumented to collect air velocity, mass flow rates, pressure drop, and other system parameters. The schematic of the conveying system including centrifugal fan, grain cart, velocity reducer, catch box, and sensor locations can be seen in Figure 5.3. Labels and descriptions of the various sensors are listed in Table 5.1.

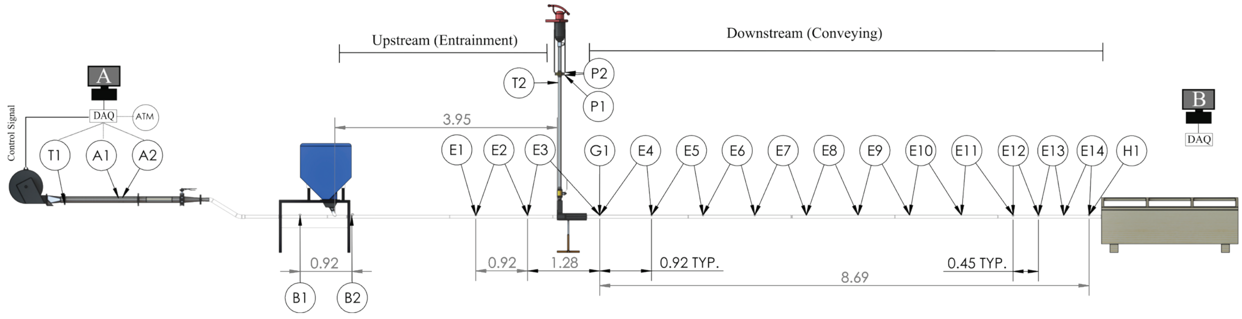

Figure 5.3: Sensor layout and pneumatic conveying system schematic. Dimensions in metres. (Larger format available in Appendix D)

Table 5.1: Sensor labels, location, and description

Sensor	Description
A1	Venturi Gauge Pressure
A2	Venturi Differential Pressure
B1	Metering Gauge Pressure
B2	Metering Differential Pressure
E1	Upstream Gauge Pressure
E2	Upstream Differential Pressure
E3	Velocity Reducer Differential Pressure
E4-E14	Downstream Differential Pressure
G1	Downstream Gauge Pressure
H1	Downstream Gauge Pressure (outlet)
P1	Orifice Plate Gauge Pressure
P2	Orifice Plate Differential Pressure
T1	Venturi Air Temperature
T2	Orifice Temperature
ATM	Atmospheric Pressure, Temperature, and Humidity

The venturi provides feedback to the centrifugal fan controller, which maintains the set air flow rate and consequently the superficial air velocity. A calibrated airlock-style metering system coupled with a stepper motor controls the product flow rate. The upstream section is located directly after product metering but before the gas extraction system. The downstream section is between the gas extraction device and the pipe outlet.

Wheat seed with properties shown in Table 5.2 was metered into the airflow at mass flow rates of 0.0205, 0.0620, and 0.1020 kg/s (meter roller speeds of 10, 30, and 50 RPM respectively). The upstream velocities were 30, 25, 20, 18, 16, and 14 m/s. The downstream velocities for a given trial were equal to or less than the corresponding upstream velocity (i.e. $\delta \leq 1$). A selection of the conveying conditions are shown in Table 5.3, with the full test matrix in Appendix F: The system was set to the test condition of interest and was run for approximately one minute to allow the system to stabilize before data were acquired for 60 seconds. The raw data were then averaged over this 60 second window. Three sets of data were collected in randomized order over multiple weeks.

Table 5.2: Average properties of the wheat used

1000 Seed Count Mass [g]	36.5 ± 0.1
Bulk Density [kg/m^3]	812 ± 3
Particle Density [kg/m^3] *	1424.9 ± 0.7
Equivalent Spherical Diameter [mm] *	3.66 ± 0.01
Sphericity [%]	60 ± 3
Geldart Classification	Group D

** Particle Density and Equivalent Diameter were calculated from the average kernel volume determined using a gas pycnometer.*

Table 5.3: Test conditions for 30 m/s upstream. Mass loading ratio given for the three product mass flow rates at 10, 30, and 50 RPM. Full table in Appendix F.

Upstream Velocity [m/s]	Downstream Velocity ± 0.05 [m/s]	Velocity Ratio ± 0.01	0.0205 kg/s at 10 RPM	0.0620 kg/s at 30 RPM	0.1020 kg/s at 50 RPM
			$\phi \pm 0.001$	$\phi \pm 0.001$	$\phi \pm 0.001$
30 ± 0.05	30	1.00	0.22	0.66	1.09
	29	0.97	0.23	0.69	1.13
	28	0.93	0.24	0.71	1.17
	27	0.90	0.24	0.74	1.21
	26	0.87	0.25	0.77	1.26
	25	0.83	0.26	0.80	1.31
	24	0.80	0.27	0.83	1.37
	23	0.77	0.29	0.87	1.43
	22	0.73	0.30	0.91	1.49
	21	0.70	0.31	0.95	1.56
	20	0.67	0.33	1.00	1.64
	19	0.63	0.35	1.05	1.73
	18	0.60	0.37	1.11	1.82
	17	0.57	0.39	1.17	1.93
	16	0.53	0.41	1.25	2.05
	15	0.50	0.44	1.33	2.19
	14	0.47	0.47	1.42	2.34
	13	0.43	0.51	1.53	2.52
	12	0.40	0.55	1.66	2.73
	11	0.37	0.60	1.81	2.98
	10	0.33	0.66	1.99	3.28

**Excerpt. Test conditions for the other upstream velocities [25, 20, 18, 16, 14, 12, 10, and 8 m/s] follow a similar pattern with the lowest downstream velocity dependant on operating conditions and potential for plugging. Even with the powered vent the amount of air bled off was not large enough to achieve equal downstream velocities for all upstream velocities.*

5.3 RESULTS AND DISCUSSION

Specific pressure drops and mass loading ratios were calculated for each test condition. Models of the form of Equation 5.3 were fit to these data. Specific pressure drop is length-dependent and was calculated individually for the upstream and downstream sections. The downstream section was further subdivided into five parts, summarized in Table 5.4, to explore any location dependant changes in pressure drop.

Table 5.4: Pressure drop groupings, sensors used, and length of test section.

Location	Pressure Sensors Used	Test Section Length [m]
Upstream	E2	0.92
Downstream	E4-E14	9.18
D1	E4, E5	1.84
D2	E6, E7	1.84
D3	E8, E9	1.84
D4	E10, E11	1.84
D5	E12, E13, E14	1.35

Data were grouped into velocity ratio bins with a span of 0.05 to facilitate comparison. Three representative plots of the downstream section are shown in Figure 5.4 and the curve fit slope (K-value) for all the cases is plotted in Figure 5.5.

Specific pressure drop was calculated using the differential line pressures at each section and Equation 5.2. A linear relationship between the specific pressure drop and the mass loading ratio was observed. A bi-square weighted regression technique was used to determine the following linear fit equations for the three data sets plotted in Figure 5.4 . This was chosen specifically to remove the effect of very large outliers and minimize the weighting of smaller outliers on the curve fit (NIST 2012). These outliers were due to large pressure spikes that occurred at very low system velocities and high mass flow rates right before plugging.

$$\alpha_{0.95-1.00} = 0.170\phi + 1.04 \qquad 5.5$$

$$\alpha_{0.60-0.65} = 0.002\phi + 0.94 \qquad 5.6$$

$$\alpha_{0.30-0.35} = -0.065\phi + 0.61 \qquad 5.7$$

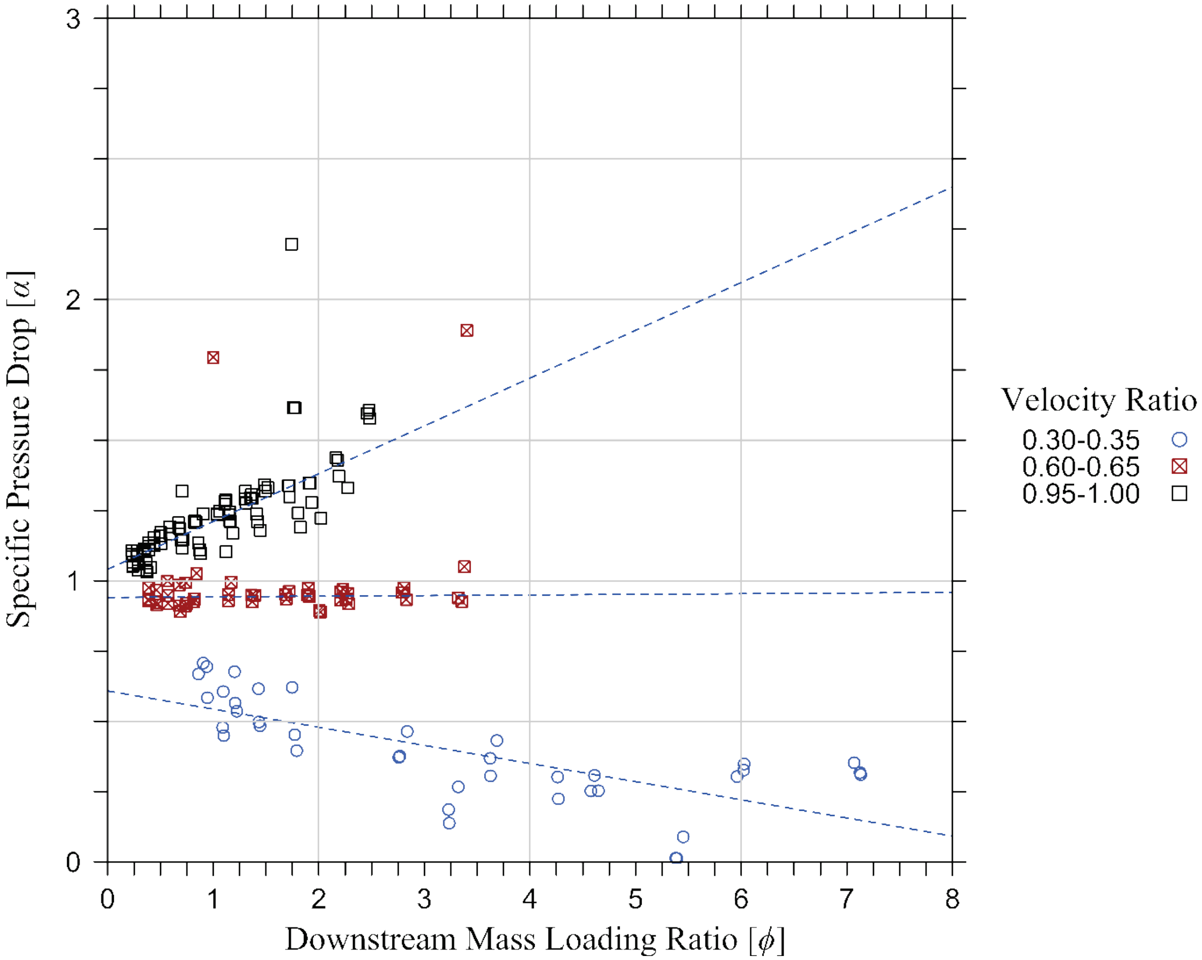

Figure 5.4: Specific pressure drop vs mass loading ratio at the following velocity ratio ranges: 0.30-0.35, 0.60-0.65, and 0.95-1.00.

Figure 5.4 displays the relationship between specific pressure drop in the entire downstream section and mass loading ratio, plotted in velocity ratio bands of 0.30-0.35, 0.60-0.65, and 0.95-1.00. For the 0.95-1.00 velocity ratio band, which coincides with no gas extraction, the relationship observed is in agreement with Gasterstadt's equation. Using Equation 5.5, a K-value of 0.17 is obtained in the downstream conveying section.

The slope of the curve fit to data for a velocity ratio of 0.6 to 0.65 gave a much different result compared to larger velocity ratios. The curve fit of Equation 5.6 gave a slope of 0.002. A slope of zero indicates that the specific pressure drop in this section of the conveying system is independent of mass loading ratio, and therefore conveying velocity at this ratio. The zero slope condition is interesting as it shows that the product can be conveyed at a much lower velocity than it was entrained at regardless of mass flow rate. This indicates a potential for velocity reduction and therefore power savings downstream of entrainment. The data show there is no additional pressure drop in the downstream section over the air-only case when the velocity ratio is approximately 0.6 to 0.7.

The remaining velocity ratio band of 0.30-0.35 shows a negative relationship between specific pressure drop and mass loading ratio. Equation 5.7 gives a slope of -0.06 and an intercept of 0.6. This indicates that small velocity ratios do not follow Gasterstadt's equation as the conveying velocity is approaching the saltation velocity. Visual observations of the product behaviour at these low velocity ratios determined the product was over accelerated as they were essentially being fired out of the conveying line at a higher velocity than the conveying air. This would indicate they were experiencing a negative drag force and that power was wasted accelerating the product to a higher velocity than needed to convey them through the pipeline.

To bring together the behaviour of all tested conditions, the slope (K-value) for each of the locations of interest in Figure 5.5 were plotted against the velocity ratio. The velocity ratios were plotted in bands as there were too many velocity ratios to show all the plots and there are more than one combination of velocities that would give similar velocity ratios. The velocity ratio bands are indicated by the upper bound to simplify the figure, with the lower bound being 0.05 less.

The downstream conditions have some variation between locations but aside from D1 are relatively consistent. It is assumed that stable conveying conditions were not attained in this section due to its proximity to the gas extraction system. K-Values converge between bands 0.6 and 0.65 at a value of 0. A zero slope indicates that the specific pressure drop is independent of the mass loading ratio, and therefore downstream velocity, at a given velocity ratio. Given that this is consistent at all downstream locations it appears that at a velocity ratio between 0.6 to 0.7 will allow for the greatest reduction in downstream conveying velocity. Stated differently, at this velocity ratio the product requires no additional downstream pressure drop to convey when compared to the air only pressure drop.

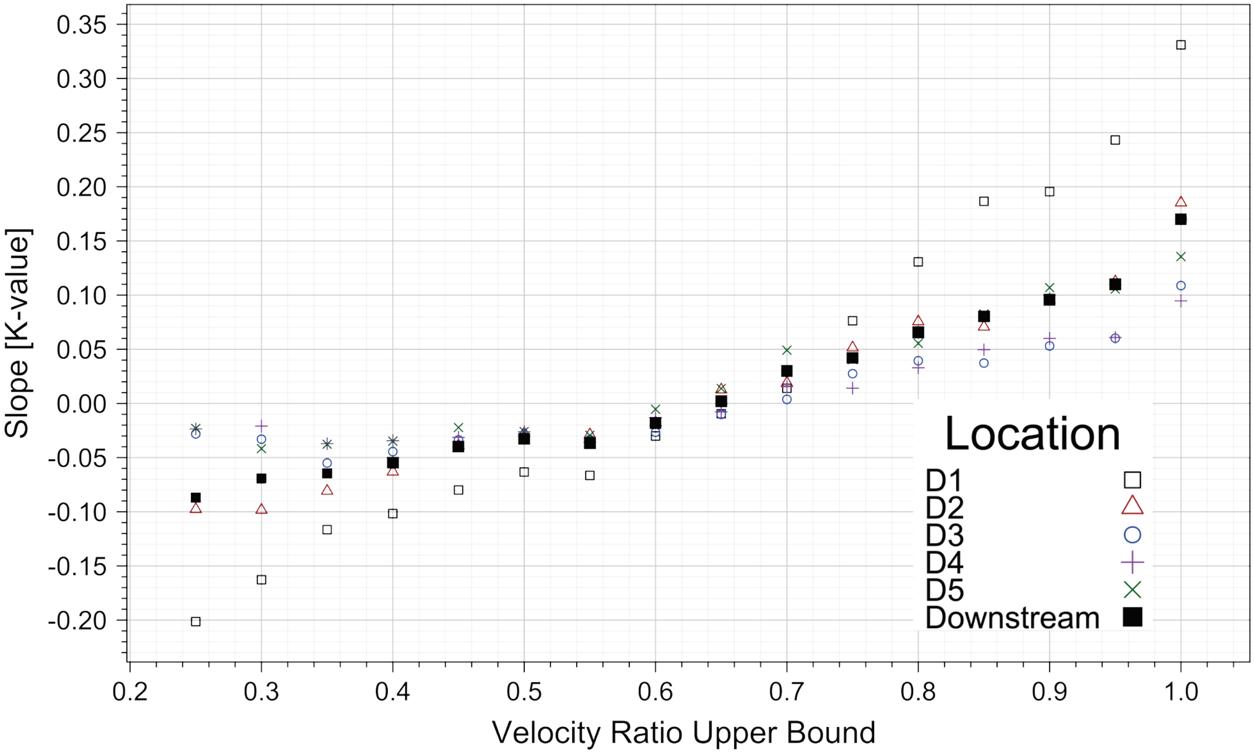

Figure 5.5: Slopes of the specific pressure drop plotted against the mass loading ratio for all velocity ratio bands. Grouped by location.

Downstream power was calculated as shown in Equation 5.8 using the total downstream pressure drop and the volumetric flow rate of air. The value for power was then normalized by the solids mass flow rate and the conveying length to obtain specific energy as shown in Equation 5.9.

$$P=\Delta p\cdot\dot{V}=[Pa]\left[\frac{m^3}{s}\right]=\left[\frac{N}{m^2}\right]\left[\frac{m^3}{s}\right]=\frac{N\cdot m}{s}=\frac{J}{s}=W \qquad 5.8$$

$$E_{Specific}=\frac{P}{\dot{m}_s\cdot l}=\frac{\left[\frac{J}{s}\right]}{\left[\frac{kg}{s}\right][m]}=\frac{J}{kg\cdot m} \qquad 5.9$$

Figure 5.6 shows the relationship between specific energy and velocity ratio, organized by upstream air velocity. Because upstream velocity was held constant, a velocity ratio <1 indicates that gas was extracted and the product is conveyed at a lower velocity downstream. This figure shows that it takes less energy in the downstream conveying section for any velocity ratio less than 1.

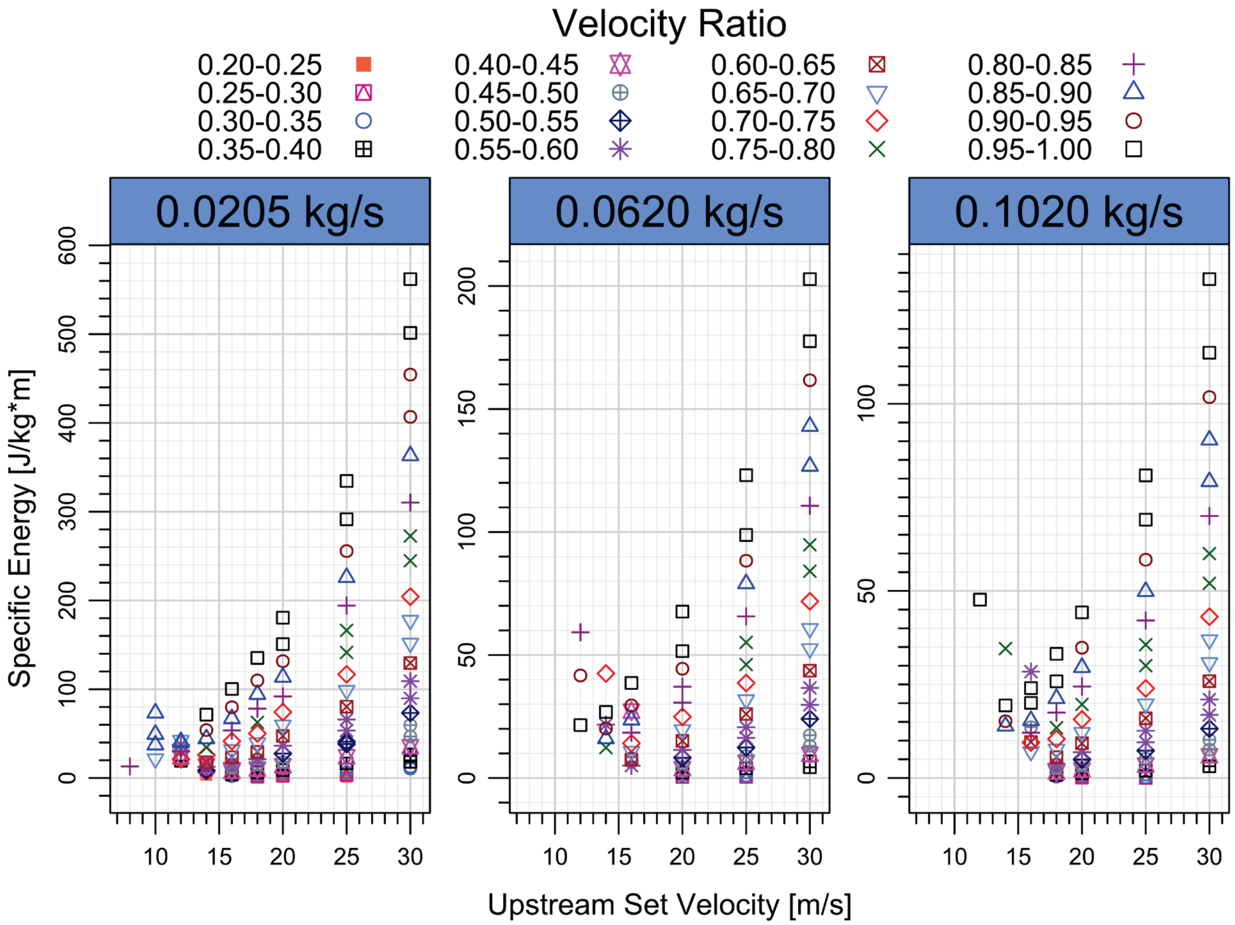

Figure 5.6: Average specific energy plotted by upstream air velocity. Each panel is a plot of a different mass flow rate (set meter roller RPM of 10, 30, and 50 from left to right respectively). One trial is shown for clarity as the values between trials are very similar. A figure with all trials is located in Appendix G:

Based on results from Figure 5.5, a K-value of 0 occurred nearest to a velocity ratio of 0.6-0.65. Looking at the difference between no gas extraction (velocity ratio of 1.0) and this point in Figure 5.6: Panel 1 (0.0205 kg/s) gives an energy difference of 74% for 18 m/s, 75% for 20 m/s, 78% for 25 m/s, and 78% for 30 m/s upstream. Compared to entraining and conveying at 18 m/s, there is a savings of approximately 10, 8, and 5 J/kg m for 0.205, 0.0625, and 0.1020 kg/s respectively when entraining at 30 m/s and conveying at 18 m/s. Therefore, a conveying length and mass flow-rate dependant energy savings is achieved by operating at a lower velocity downstream while entraining at a higher velocity.

Panel 2 of Figure 5.6 depicts the specific energy at a mass flow rate of 0.062 kg/s. The overall trend is very similar to the previous plot but the specific energy per unit mass and length is lower due to the higher product mass flow rate. The energy difference between the no bleed-off condition and a K-value of zero is approximately 79% for the three highest upstream velocities.

The specific energy required to convey wheat at 0.1020 kg/s is displayed in Figure 5.6: Panel 3. Again, the overall trend is similar with less energy required to convey per kilogram at the higher mass flow rate. The difference between no gas extraction and a K-value of zero is approximately 80% for the four highest upstream set velocities.

It was initially hypothesized that there would exist three conditions when the specific pressure drop was plotted against the mass loading ratio: A positive K-Value at a velocity ratio of one that follows Gasterstadt's equation and the results of other work, a negative K-Value if the velocity ratio was much less than one, and a condition in-between where the K-Value was zero. From the data collected and shown in the above figures all three of these conditions were observed using a gas extraction system in an agricultural pneumatic conveying setup.

For this to be useful from an industry perspective a few conditions would need to be satisfied, namely the benefit of using a differential velocity must be greater than the extra power required to accelerate the particles in the entrainment zone. A system with similar conditions to those used in this analysis would need to be designed to create a velocity ratio of approximately 0.6 to 0.7 with the least amount of extra power required. Whether this design would be a long venturi, eccentric venturi, or a stepped pipe would depend on individual conveying requirements of the system and the type of product conveyed.

5.4 CONCLUSIONS

A gas extraction system was used to explore the effect of varying upstream and downstream conveying air velocity ratios on the specific pressure drop and specific energy required to convey wheat at three mass flow rates. For a velocity ratio of one ($u_{g\ down} = u_{g\ up}$), the system agreed with Gasterstadt's equation with a K-value of 0.17 for the downstream section.

A K-value of approximately zero occurred at a velocity ratio of 0.60-0.65. This indicates that at this condition, the pressure required to convey the air and the product was equal to the pressure drop of air only. While data are not currently available, it is hypothesised that the slip velocity at this condition is essentially zero, meaning that the particle velocity would be equal to the conveying gas velocity. The over-accelerated product is able to maintain this velocity for the short conveying distance of the studied system. Eventually the product would decelerate back to normal slip velocities due to wall and particle interactions, but for the tested operating conditions and short conveying lengths, the effect was stable. This indicated that a set of conditions exist that allow for accelerating wheat over the entrainment section and recovering the pressure drop over a relatively short conveying length.

Conveying wheat at a velocity ratio of 0.60-0.65 had a specific energy approximately 75 to 80% lower than if it was conveyed at the entrainment velocity for the entire length. While this was a substantial difference, it is more realistic to compare 0.60-0.65 velocity ratio trials with the same downstream conveying velocity with a velocity ratio of 1. For these scenarios, the specific energy of entraining at a ratio of 0.6-0.65 is 8-16% lower than conveying at the same entrainment and downstream velocity.

Further investigation is recommended as slip velocity likely plays a large role in the behaviour seen in this experiment. When these data were collected, a system for recording the particle velocity was not available, but a particle tracking system is being built that would allow the actual velocity of the particles to be determined under these test conditions. Additionally, it was assumed that the particles were traveling at the average downstream air velocity when the K-value is zero. This indicates that the pressure drop of air only is the same as that of air plus product. Further testing is needed to determine the origin of the energy savings that enables the product to be conveyed using the same energy as air only. The working theory is that the presence of particles in the air stream work to suppress turbulence and over the short conveying distances, this balances out the extra friction effects of the particles in the airstream.

A gas extraction system implemented as used in this work did appear to add some benefit to the energy required to convey but it must be acknowledged that the initial particle acceleration to a higher entrainment velocity does come with an energy penalty. Therefore, the power saved in the conveying section must be greater than that which was initially required. From the data presented an overall energy savings can result if the particles can be accelerated for less than approximately 10, 8, or 5 J/kg m (for 0.02, 0.062, 0.102 kg/s respectively).

CHAPTER 6: SUMMARY AND RECOMMENDATIONS

The main objective of this research was to explore the effect of entrainment velocity on conveying quality (as defined by the entrainment level of the particles) and the energy required to convey a given amount of wheat, a very commonly conveyed agricultural product. Efficiencies are desired in agricultural pneumatic conveying systems as they typically operate in the dilute phase, which uses higher power per unit mass of product conveyed then other conveying methods.

An imaging method using a laser to illuminate a cross-section of the flow was developed to create probability distribution maps of the conveyed particles in the pipeline. This system was built to allow for multiple imaging positions, ease of calibration, and was designed for both horizontal and vertical installations in dilute phase pneumatic conveying systems. Additionally, there are provisions for future work in implementing a particle tracking velocimetry system that would be able to determine the velocities of the particles.

To enable conveying at multiple entrainment and conveying velocities, modifications were made to a lab-scale pneumatic conveying system. A gas extraction system was developed that was used to vent conveying air, which in turn lowered the downstream conveying velocity independently of the entrainment velocity. This system was used alongside the imager to quantify the statistical location of the particles in the flow. These images were used to determine the centroid of the particle distribution at various locations in the conveying system.

The gas extraction system was used to explore the relationship between entrainment velocity and conveying velocity on the specific pressure drop at varying mass loading ratios. The slope of this relationship indicated the stability of the system. Typical published results of this relationship show a positive slope that is particle and conveying-line diameter dependant. A positive slope occurs because it requires more pressure to convey particles in the air flow than it does air alone. In this work a velocity ratio of approximately 0.6-0.65 had a slope of zero, which indicated that the same pressure drop was required for both product and conveying air as was required in the air-only case.

Outcomes of the research:

1. The development of a novel cross-sectional imager was completed and tested that obtained qualitative images of the product's behavior perpendicular to the direction of

flow. Additionally, these images were used to create a quantitative location of the centre of mass of the conveyed particles.

2. The imager was used to show that particles conveyed at one downstream velocity but entrained at different velocities, had different entrainment levels.
3. The slope of the specific pressure drop vs mass loading ratio line was zero at a velocity ratio of 0.6-0.65.

From the above outcomes it was concluded that for a given conveying velocity downstream a higher upstream entrainment velocity produced two results when compared to operating the system at a single velocity. An increased entrainment level and a decrease in the specific energy required to convey particles in the downstream section were both observed.

6.1 RECOMMENDATIONS AND FUTURE WORK

The main recommendations for further work are:

- While the gas extraction system was chosen for its flexibility, it does have a small but significant effect on the particles' behavior. If future work is undertaken, it is recommended that a stepped pipe configuration be explored. Multiple ratios could be tested, but at a minimum, a velocity ratio of approximately 0.6-0.7 should be used to see if the results are similar to those found in this work. The abrupt enlargement will also have an affect on the conveying characteristics as indicated in a numerical simulation by Marjanovic, Levy et al. (1999). Further testing should be completed to be determined whether the effect would be positive or negative in this conveying regime.
- The effect of particle velocity was not explored in this work. The imaging platform has been further developed and can now perform particle tracking velocimetry parallel to the fluid flow. In future testing, collecting the particle velocity would be invaluable in drawing meaningful conclusions into the conveying behaviour.
- The conveying length of the test setup was a longer straight horizontal run than found in agricultural pneumatic systems but quite a bit shorter than in many in published literature. It is possible that the zero slope of the specific pressure drop versus mass loading ratio occurs at a velocity ratio of 0.6-0.65 due the particles having enough momentum to continue through the pipe. While this might not be a stable condition on longer systems it does imply the possibility of designing a system to operate at the lowest possible velocity.

Further work is needed to describe the particle velocity compared to the conveying air velocity after gas extraction to explore this effect.

REFERENCES

Adrian, R. J. (1991). "Particle-Imaging Techniques for Experimental Fluid Mechanics." Annual Review of Fluid Mechanics 23(1): 261-304.

Adrian, R. J. and J. Westerweel (2011). Particle Image Velocimetry. Cambridge; New York, Cambridge University Press.

Adrian, R. J. and C.-S. Yao (1985). "Pulsed laser technique application to liquid and gaseous flows and the scattering power of seed materials." Applied Optics 24(1): 44-52.

ASTM (2006). Standard Test Method for Sieve Analysis of Fine and Coarse Aggregates. West Conshohocken, PA, ASTM International. C136: 1-5.

Barbosa, P. R. and P. Seleghim Jr. (2003). "Improving the power consumption in pneumatic conveying systems by adaptive control of the flow regime." Journal of the Brazilian Society of Mechanical Sciences and Engineering 25(4): 373-377.

Cabrejos, F. and G. Klinzing (1992). Solids mass flow rate measurements in pneumatic conveying. Winter Annual Meeting, November 8, 1992 - November 13, 1992, Anaheim, CA, USA, Publ by ASME.

Cabrejos, F. J. and G. E. Klinzing (1992). "Incipient motion of solid particles in horizontal pneumatic conveying." Powder Technology 72(1): 51-61.

Cabrejos, F. J. and G. E. Klinzing (1994). "Minimum conveying velocity in horizontal pneumatic transport and the pickup and saltation mechanisms of solid particles." Bulk Solids Handling 14(3): 541-550.

Cabrejos, F. J. and G. E. Klinzing (1994). "Pickup and saltation mechanisms of solid particles in horizontal pneumatic transport." Powder Technology 79(2): 173-186.

Case IH. (2012). "Precision Hoe Air Drills." Retrieved June 4, 2012, from http://www.caseih.com/en_us/products/plantingseeding/pages/precision-hoe-800.aspx.

Drew, D. (1976). "Two-phase flows: Conservative equations for lift and brownian motion and some basic flows." Archive for Rational Mechanics and Analysis 62.

Fan, L. S. and C. Zhu (2005). Principles of Gas-Solid Flows. Cambridge, UK, Cambridge University Press.

Farbar, L. (1949). "Flow Characteristics of Solids-Gas Mixtures in a Horizontal and Vertical Circular Conduit." Industrial & Engineering Chemistry 41(6): 1184-1191.

Flexi-Coil (1997). Flexi-Coil 20 Series Seed Cart GH-001V9. Saskatoon, Sask, CNH Canada Ltd. Tech Publications & Tools.

Flexi-Coil (2011). Air-Cart Assembly Instructions. Saskatoon, Sask, CNH Canada Ltd. Tech Publications & Tools.

Gasterstadt, J. (1924). "Experimental Investigation of the Pneumatic Conveying Process." Ingenieur Wesens(265): I924.

Giddings, D., B. J. Azzopardi, A. Aroussi and S. J. Pickering (2011). "Optical investigation of a long throated venturi conveying inert spherical particulate with size range similar to pulverised coal." Powder Technology 207(1–3): 370-377.

Güner, M. (2007). "Pneumatic conveying characteristics of some agricultural seeds." Journal of Food Engineering 80(3): 904-913.

Hinkle, B. L. (1953). Acceleration of particles and pressure drops encountered in horizontal pneumatic conveying. (Ph.D. Thesis), Georgia Institute of Technology.

Hubert, M. and H. Kalman (2003). "Experimental determination of length-dependent saltation velocity in dilute flows." Powder Technology 134(1–2): 156-166.

Hubert, M. and H. Kalman (2004). "Measurements and comparison of saltation and pickup velocities in wind tunnel." Granular Matter 6: 159-165.

Kalman, H., A. Satran, D. Meir and E. Rabinovich (2005). "Pickup (critical) velocity of particles." Powder Technology 160(2): 103-113.

Keep, T. and S. Noble (2013). Exploration of Product Flow Behavior and Entrainment through Downstream Velocity Reduction. Proceedings of CANCAM 2013-the 24th Canadian Congress of Applied Mechanics, Saskatoon, Saskatchewan, University of Saskatchewan.

Keep, T. and S. D. Noble (2015). "Optical flow profiling method for visualization and evaluation of flow disturbances in agricultural pneumatic conveyance systems." Computers and Electronics in Agriculture 118: 159-166.

Klinzing, G., F. Rizk, R. Marcus and L. S. Leung (2010). Pneumatic Conveying of Solids: A Theoretical and Practical Approach, Springer.

Klinzing, G. E. and S. Dhodapkar (1993). Apparatus for facilitating solids transport in a pneumatic conveying line and associated method. USPTO. 5,252,007.

Kraus, M. N. (1991). Pneumatic Conveying Systems for Bulk Materials, Prentice Hall.

Link, W. H., G. A. Jama, J. O. Thorn and G. E. Klinzing (2000). "Increase of system capacity by using a flow enhancer." Powder Handling and Processing 12(1): 7-10.

Maas, H. G., A. Gruen and D. Papantoniou (1993). "Particle tracking velocimetry in three-dimensional flows." Experiments in Fluids 15(2): 133-146.

Marjanovic, P., A. Levy and D. J. Mason (1999). "An investigation of the flow structure through abrupt enlargement of circular pipe." Powder Technology 104(3): 296-303.

Mehta, R. D. (1985). "Aerodynamics of Sports Balls." Annual Review of Fluid Mechanics 17: 151-189.

Mills, D. (2004). Handbook of Pneumatic Conveying Engineering. Handbook of Pneumatic Conveying Engineering, CRC Press.

Mills, D. (2006). "Pneumatic conveying - Before stepping the line, look into air extraction." Chemical Engineering 113(2): 40-47.

NIST. (2012). "Bisquare weighting." NIST/SEMATECH e-Handbook of Statistical Methods Retrieved October 12, 2016, from http://www.itl.nist.gov/div898/handbook/.

Pahk, J. B. and G. E. Klinzing (2010). "Voidage measurement for a moving plug in dense phase pneumatic conveying using two different methods." Particulate Science & Technology 28(6): 511-519.

Rinoshika, A. (2014). "Dilute pneumatic conveying of a horizontal curved 90° bend with soft fins or dune model." Powder Technology 254(0): 291-298.

Rinoshika, A. and M. Suzuki (2010). "An experimental study of energy-saving pneumatic conveying system in a horizontal pipeline with dune model." Powder Technology 198(1): 49-55.

Saffman, P. G. (1965). "The lift on a small sphere in a slow shear flow." Journal of Fluid Mechanics 22(02): 385-400.

Santos, S. M., E. B. Tambourgi, F. A. N. Fernandes, D. Moraes Júnior and M. S. Moraes (2011). "Dilute-phase pneumatic conveying of polystyrene particles: pressure drop curve and particle distribution over the pipe cross-section." Brazilian Journal of Chemical Engineering 28: 81-88.

Shamlou, P. A. (1988). Handling of bulk solids, theory and practice. Stoneham, MA, Rutterworths.

Smits, A. J. and J. P. Dussauge (2005). Turbulent Shear Layers in Supersonic Flow, Springer.

Turton, R. and O. Levenspiel (1986). "A short note on the drag correlation for spheres." Powder Technology 47: 83-86.

Westerweel, J. (1997). "Fundamentals of digital particle image velocimetry." Measurement Science and Technology 8(12): 1379.

Wypych, P. W. (1999). "Pneumatic conveying of powders over long distances and at large capacities." Powder Technology 104(3): 278-286.

Yan, F. and A. Rinoshika (2011). "Application of high-speed PIV and image processing to measuring particle velocity and concentration in a horizontal pneumatic conveying with dune model." Powder Technology 208(1): 158-165.

Yan, F. and A. Rinoshika (2013). "High-speed PIV measurement of particle velocity near the minimum air velocity in a horizontal self-excited pneumatic conveying of using soft fins." Experimental Thermal and Fluid Science 44(0): 534-543.

Yan, F. and A. Rinoshika (2013). "Particle fluctuation velocity of a horizontal self-excited pneumatic conveying near the minimum pressure drop. (sic)." Powder Technology 241(0): 115-125.

Yan, F., A. Rinoshika and H. Nonaka (2012). "An experimental study on a horizontal energy-saving pneumatic conveying system with soft fins." Powder Technology 217(0): 516-522.

Appendix A: Lab-Scale Pneumatic Conveying System Images and Schematic

The following figures outline the air handling laboratory and the layout of the conveying equipment in greater detail then was necessary in the thesis.

Figure A-1:Air handling system components from top-left to bottom-right: product collection box, downstream conveying line, horizontal bleed-off, upstream conveying-line, product tank and metering system.

Figure A-2: Powered gas-extraction system as seen from the top of the product tank.

Product Tank and metering system

The test tank was modified by CNH R+D Saskatoon as shown in the following figure for portability. It was originally a third tank add-on for an older generation of a Flexi-coil air cart.

Figure A-3: Product holding tank and metering box before conversion to stepper motor drive.

Stepper Motor

The metering roller was converted from the standard 12-volt electric motor with hydraulic torque converter in the original implementation, to a programmable stepper motor. This change was made to allow for simple adjustment of shaft speeds, ease of setting the desired number of revolutions, and the option to vary the torque output. The stepper motor chosen was the IMS MDrive 42. The stepper motor was coupled with a 10:1 reduction APEX Dynamics gear head shown in Figure A-4 for speed reduction and torque amplification. This gear box has less than 8 arc minutes of backlash and is below 56 decibels.

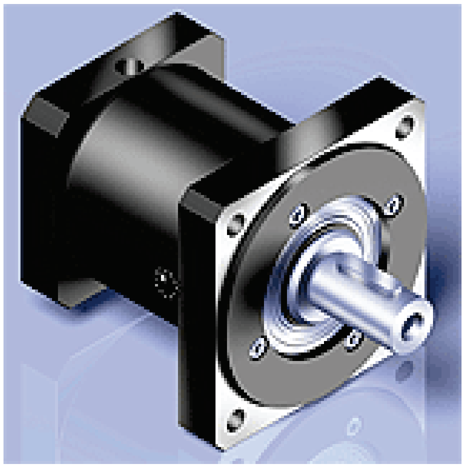

Figure A-4: APEX Dynamics High Precision Planetary Gearbox (APEX Dynamics 2010)

The stepper motor was mounted to the test cart with a custom built three axis adjustable mounting system shown in Figure A-5. This allowed for full adjustment of the motor positioning for flexibility in coupler choice, shaft length, and allowed for ease of roller change.

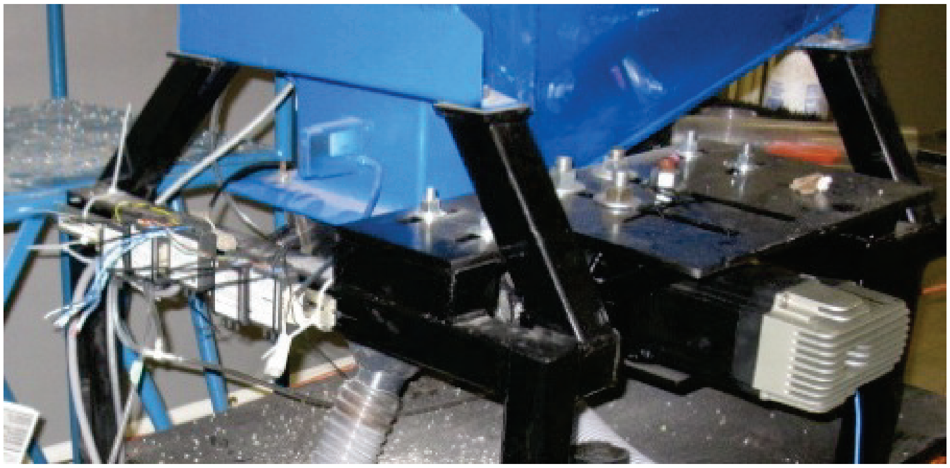

Figure A-5: Stepper Motor with a custom, fully adjustable mount and quick coupler.

The fan used for testing is a production CNH air cart fan and is shown in Figure A-6. It has been converted to run off three phase power and be controlled by an input current. This allows fan speed control with the use of LabVIEW and also allows for automation with the use of a feedback loop.

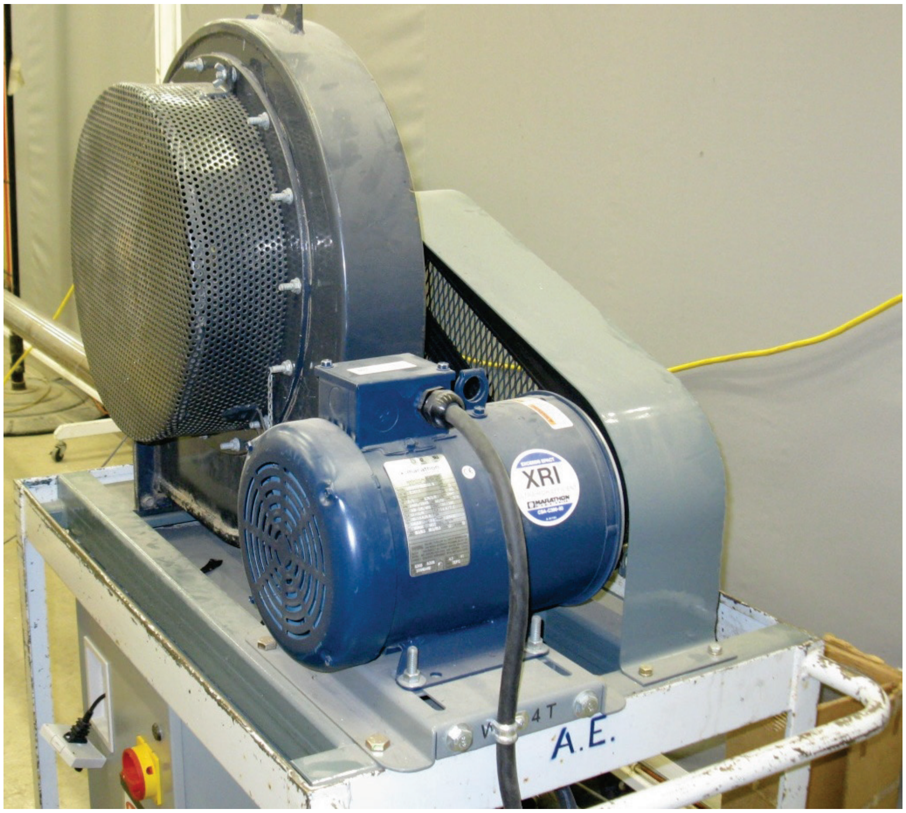

Figure A-6: Converted 3 Phase Electric Drive CNH fan

Figure A-7: Inside of Test Cart tank

Figure A-7 shows the inside of the air cart and the top of the metering box can be seen.

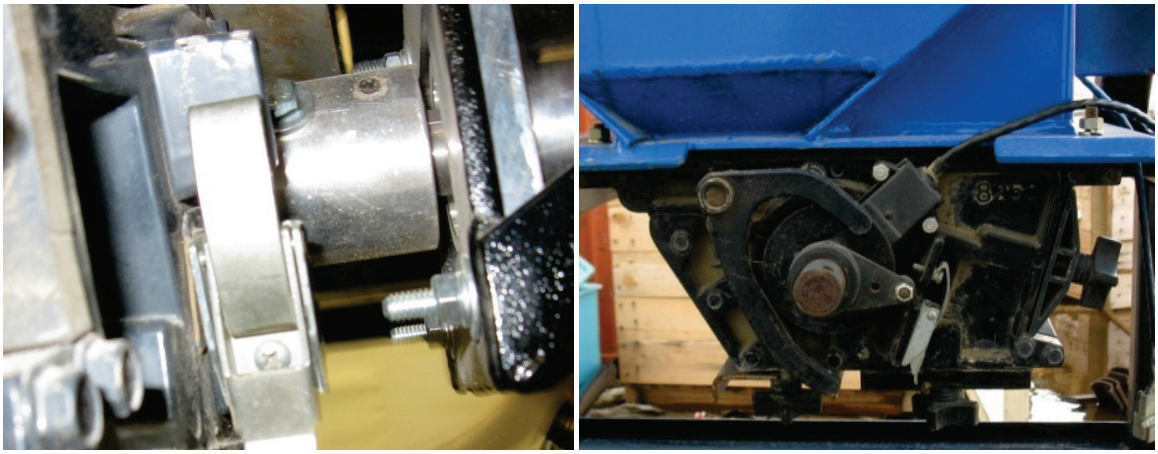

Figure A-8: Motor coupler and side view of metering box.

In the left-hand photo of Figure A-8 the quick connect coupler is shown mounted to the shaft and the stepper motor. The cam which controls the agitator bar (aids in preventing bridging and plugging of the product over the meter box) and the shaft sensor can be seen in the right-hand photo.

ITEM	PART NUMBER	DESCRIPTION	QTY.
1	Fan and Diverter Assembly	Includes: 3-phase Centrifugal Fan, Venturi Assembly, Wye Splitter, Diverter Valves, and Flexible Hose	1
2	Air Cart and Metering System	Mock up of Lab Scale Air Cart and Metering System	1
3	Product Insertion Assembly	Flow Conditioner in upstream air-only line. Downspout and Product Insertion Pipe	1
4	Upstream Conveying Line	2 Acrylic Pipe: Sections: 57 mm I.D.x1835 mm long	1
5	Velocity Reducer Assembly	Velocity Reducer includes: Velocity Reducer, Orifice Plate, Servo Valve, Flow Straighteners, and Power Vent	1
6	_Optical Flow Profiling Apparatus	Includes: Optical Sled, Rails, Cable Tray, and Adjustable Frame.	1
7	Downstream Convyeying Line	5 Acrylic Pipe Sections: 57 mm I.D. x 1835 mm long	1
8	Product Collection Box	Vents conveying air. Slows down, stops, and contains product.	1

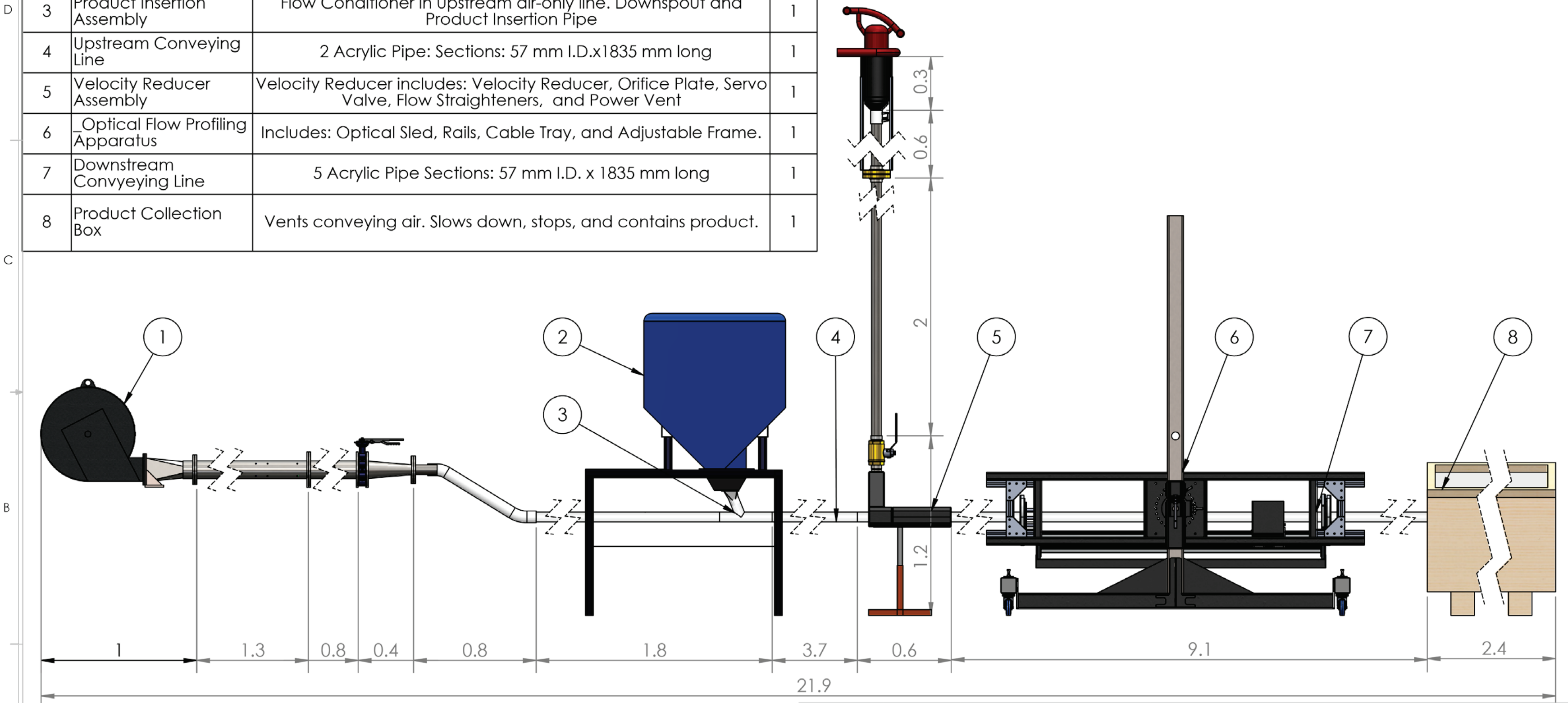

PROPRIETARY AND CONFIDENTIAL
THE INFORMATION CONTAINED IN THIS DRAWING IS THE SOLE PROPERTY OF THE U of S. ANY REPRODUCTION IN PARTOR AS A WHOLE WITHOUT THE WRITTEN PERMISSION OF THE U of S IS PROHIBITED.

NEXT ASSY
USED ON
APPLICATION

UNLESS OTHERWISE SPECIFIED:
DIMENSIONS ARE IN: METRES
TOLERANCES:
FRACTIONAL ±
ANGULAR: MACH ± BEND ±
TWO PLACE DECIMAL ±
THREE PLACE DECIMAL ±
INTERPRET GEOMETRIC TOLERANCING PER:
MATERIAL
Various
FINISH
DO NOT SCALE DRAWING

	NAME	DATE
DRAWN	tyk524	May-15-14
CHECKED	tyk524	December-18-15
ENG APPR.		
MFG APPR.		
Q.A.		

COMMENTS:

University of Saskatchewan
TITLE:
Lab Scale Air Handling System
SIZE B
DWG. NO. _Air Handling System
REV 3
SCALE 1 : 25
WEIGHT:
SHEET 1 OF 2

Figure A-9: Pneumatic Conveying System Schematic

Appendix B: Venturi Calibration and Pitot Tube Traverse

The following figure shows the fan and the section that contains the venturi meter which is used to measure the air mass flow rate and therefore the air speed. The computer shown runs a LabVIEW program that monitors the resulting air speed and adjusts the control setting in a PID loop that outputs a 4-20mA signal to the VFD drive attached to the three-phase fan.

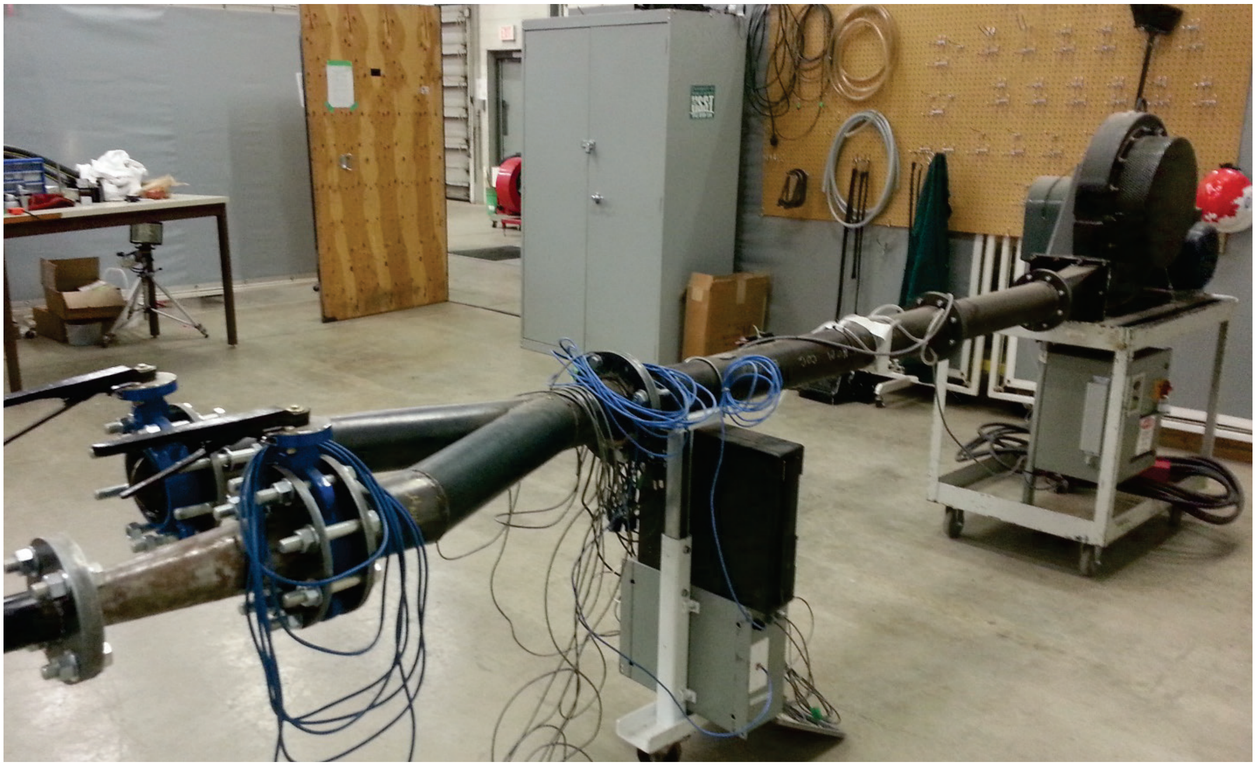

Figure B-1: Centrifugal fan, venturi (inside pipe), wye-splitter, control valves, variable frequency drive (VFD), and data acquisition system (DAQ).

Figure B-2 shows the Venturi meter drawing with the pressure taps. The venturi was rapid prototyped by CNH Canada Ltd and installed under the middle section of pipe (the air-lines can be seen running to the pressure taps).

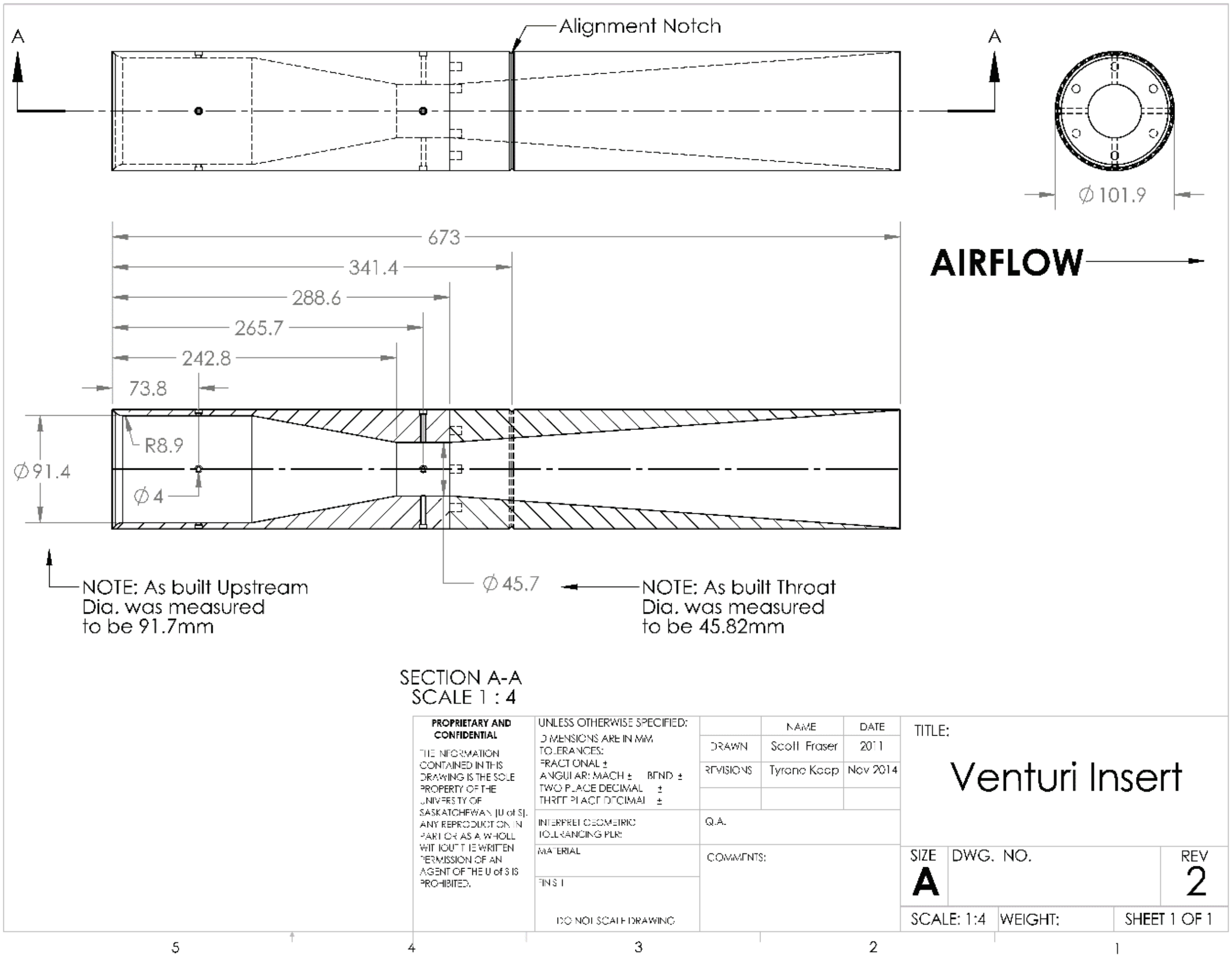

Figure B-2: Venturi Meter production drawing.

While the venturi was modeled after a ISO 5167 standard venturi it was modified to fit our size constraints. Because of this the venturi was calibrated with multiple pitot tube traverses. Three traverses were completed: Vertical, 60°, and 120° clockwise which gives 60° spacing between lines. This is shown in the following figure.

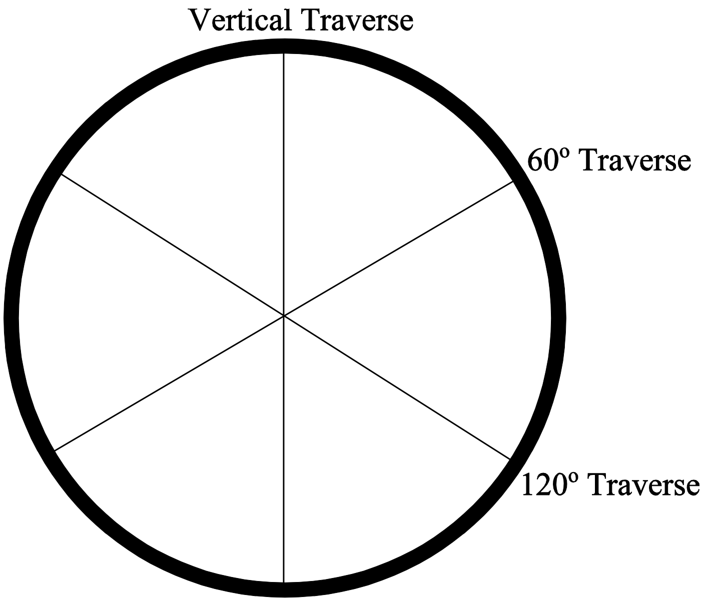

Figure B-3: Layout of pitot tube traverses.

10 pressures were taken along each line at distances shown in Table B-1. The distance was calculated using a Log-Chebyshev's approximation which is used to weight the velocities.

Table B-1: Traverse position and distance from starting point of traverse in mm

Traverse Position	Log-Chebyshev Rule Multipliers	Traverse Position (mm)
	0	0.00
1	0.019	1.14
2	0.077	4.62
3	0.153	9.17
4	0.217	13.01
5	0.361	21.65
6	0.639	38.32
7	0.783	46.95
8	0.847	50.79
9	0.923	55.35
10	0.981	58.83
	1	59.97

Table B-2 shows the averaged velocities after the separate traverse points were combined into a single velocity for that test condition.

Table B-2: Averaged velocities calculated by pitot traverse used in calibration of venturi meter.

Traverse	Set Air Speed	Venturi Velocity (m/s)	Venturi Qv [m3/s]	Venturi Qm [kg/s]	Pv (inH2O)	Pv (Pa)	Pstatic (inH2O)	Pstatic (Pa)	Barometric Pressure (Pa)	Air Density [kg/m3]	Air Temp (K)	Pitot Velocity (m/s)	Pitot Qv (m3/s)	Pitot Qm [kg/s]
Vertical Traverse	40.0	40.1	0.1	0.1	4.2	1043.3	0.1	31.0	97101.9	1.2	303.0	43.3	0.1	0.1
	38.0	38.0	0.1	0.1	3.6	907.0	0.1	25.6	97093.8	1.2	303.3	40.4	0.1	0.1
	36.0	36.0	0.1	0.1	3.2	808.2	0.1	23.0	97094.8	1.2	303.5	38.2	0.1	0.1
	34.0	34.0	0.1	0.1	2.9	715.9	0.1	19.8	97133.2	1.2	303.4	35.9	0.1	0.1
	32.0	32.0	0.1	0.1	2.5	630.5	0.1	17.3	97134.3	1.2	303.4	33.7	0.1	0.1
	30.0	30.0	0.1	0.1	2.2	553.1	0.1	15.2	97142.1	1.2	303.3	31.6	0.1	0.1
	28.0	28.0	0.1	0.1	1.9	477.6	0.1	13.4	97122.5	1.2	303.1	29.3	0.1	0.1
	26.0	26.0	0.1	0.1	1.7	411.5	0.0	11.4	97133.0	1.2	303.0	27.2	0.1	0.1
	24.0	24.0	0.1	0.1	1.4	349.4	0.0	9.4	97096.4	1.1	302.8	25.1	0.1	0.1
	22.0	22.0	0.1	0.1	1.2	292.5	0.0	8.0	97142.2	1.1	302.6	22.9	0.1	0.1
	20.0	20.0	0.1	0.0	1.0	240.7	0.0	6.5	97090.7	1.1	302.4	20.8	0.1	0.1
	18.0	18.1	0.1	0.0	0.8	196.4	0.0	5.2	97150.5	1.1	302.3	18.8	0.1	0.0
	16.0	16.1	0.0	0.0	0.6	155.0	0.0	4.0	97158.8	1.1	302.1	16.7	0.0	0.0
	14.0	14.1	0.0	0.0	0.5	118.9	0.0	3.0	97192.8	1.1	302.0	14.6	0.0	0.0
	12.0	12.1	0.0	0.0	0.4	87.7	0.0	2.1	97237.6	1.1	301.9	12.5	0.0	0.0
	10.0	10.1	0.0	0.0	0.2	61.5	0.0	1.4	97238.3	1.1	301.8	10.5	0.0	0.0
	8.0	8.1	0.0	0.0	0.2	39.7	0.0	0.7	97261.2	1.1	301.7	8.4	0.0	0.0
	6.0	6.0	0.0	0.0	0.1	23.4	0.0	0.2	97262.8	1.1	301.6	6.5	0.0	0.0
	4.0	4.0	0.0	0.0	0.0	11.3	0.0	-0.2	97243.7	1.1	301.5	4.5	0.0	0.0
60 Degree Traverse	40.0	40.0	0.1	0.1	4.0	1000.7	0.1	27.3	96250.0	1.2	303.8	42.7	0.1	0.1
	36.0	36.0	0.1	0.1	3.2	801.5	0.1	21.7	96262.4	1.2	304.1	38.2	0.1	0.1
	32.0	32.1	0.1	0.1	2.5	627.6	0.1	16.4	96289.6	1.2	304.0	33.8	0.1	0.1
	28.0	28.0	0.1	0.1	1.9	460.9	0.1	13.9	96237.9	1.1	303.7	29.0	0.1	0.1
	24.0	24.1	0.1	0.1	1.4	346.9	0.0	9.0	96310.7	1.1	303.3	25.1	0.1	0.1
	20.0	20.0	0.1	0.1	1.0	240.5	0.0	6.3	96269.0	1.1	303.2	20.9	0.1	0.1
	16.0	16.1	0.0	0.0	0.6	154.7	0.0	4.0	96281.6	1.1	302.8	16.8	0.0	0.0
	12.0	12.1	0.0	0.0	0.4	88.7	0.0	2.2	96375.8	1.1	302.6	12.7	0.0	0.0
	8.0	8.0	0.0	0.0	0.2	41.2	0.0	0.9	96435.7	1.1	302.4	8.6	0.0	0.0
	4.0	4.1	0.0	0.0	0.1	13.3	0.0	0.1	96458.0	1.1	302.3	4.9	0.0	0.0
120 Degree Traverse	40.0	40.0	0.1	0.1	4.1	1013.1	0.1	22.6	95659.5	1.2	273.6	40.9	0.1	0.1
	36.0	36.0	0.1	0.1	3.2	805.3	0.1	18.1	95654.7	1.2	273.6	36.4	0.1	0.1
	32.0	32.0	0.1	0.1	2.5	629.9	0.1	13.7	95617.8	1.1	273.6	32.2	0.1	0.1
	28.0	28.1	0.1	0.1	1.9	477.5	0.0	10.9	95652.9	1.1	273.5	28.1	0.1	0.1
	24.0	24.0	0.1	0.1	1.4	349.4	0.0	7.8	95682.3	1.1	273.5	24.0	0.1	0.1
	20.0	20.0	0.1	0.1	1.0	241.4	0.0	5.5	95679.6	1.1	273.4	19.9	0.1	0.1
	16.0	16.0	0.0	0.0	0.6	155.6	0.0	3.6	95755.8	1.1	273.4	16.0	0.0	0.0
	12.0	12.0	0.0	0.0	0.4	88.8	0.0	2.1	95817.6	1.1	273.4	12.1	0.0	0.0
	8.0	8.0	0.0	0.0	0.2	41.5	0.0	1.0	95812.1	1.1	273.5	8.3	0.0	0.0
	4.0	4.1	0.0	0.0	0.1	13.4	0.0	0.4	95841.5	1.1	273.6	4.7	0.0	0.0

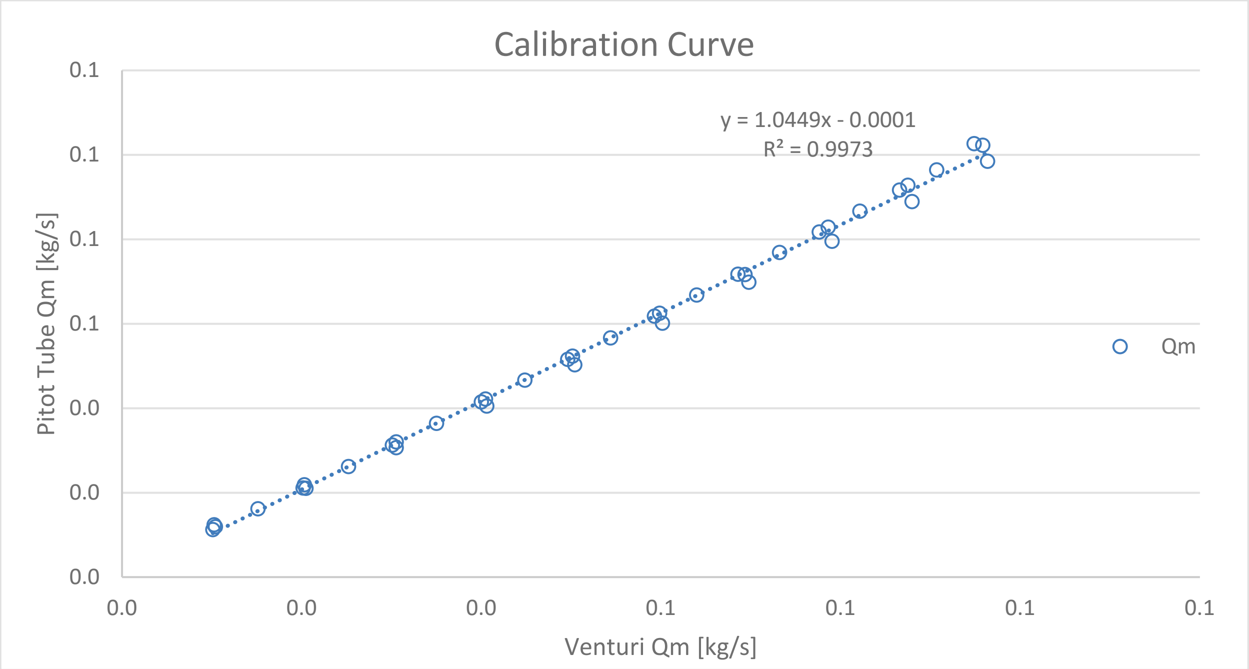

Figure B-4: Air mass flow rate when calculated by pitot tube and venturi meter. The equation of the line was used to correct the venturi meter.

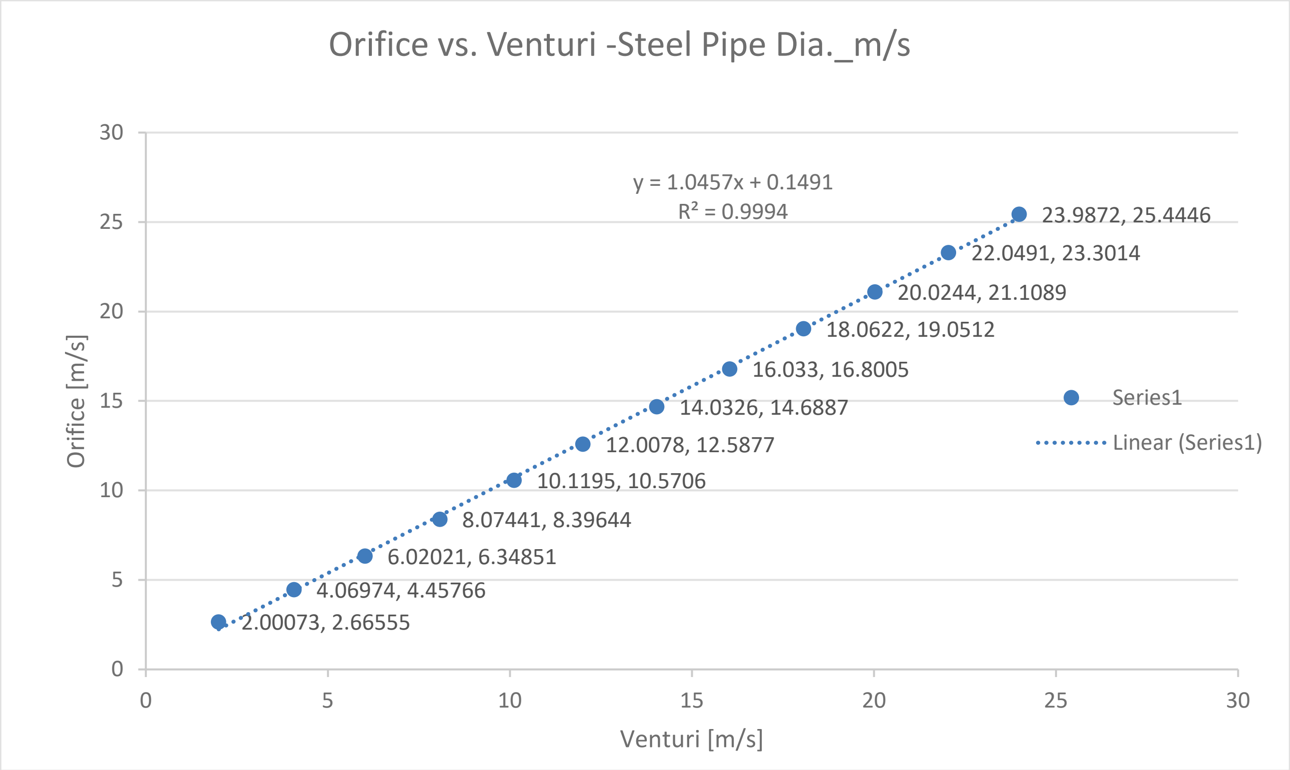

Figure B-5: Air velocity when calculated by pitot tube and venturi meter. Data was retaken on a subsequent day to create this curve which is why the correction factor is slightly different.

Appendix C: Image Processing, Using ENVI, and IDL Code

To obtain particle entrainment images and centre of mass (C.o.M.) probability distributions Environment for Visual Images (ENVI) software and Interactive Data Language (IDL) code was used. Data analysis and image processing methodology will be detailed in this appendix along with the pertinent code.

Version 1.0: Manual Image Processing

ENVI was used manually to determine an image processing method that cleaned up laser artifacts, rotated the images, and stretched the images to compensate for camera angle to determine the best course of action.

The following commands were used within ENVI Classic:

Open Normalized file

Rotate -90 degrees-saved file

Resize Data-ENVI tool. Used the ratio of x-y to come up with a linear stretch size

- Nearest Neighbor Interpolation

Used ENVI Classic to make a Region of Interest.

Make mask using Region of Interest

- Basic Tools>Masking>Build Mask
  - Select Image-Display 1 most likely.
  - Under Options choose Import ROI’s>Choose your ROI>Apply
- Basic Tools>Masking>Apply Mask
  - Select Image
  - Under Select Mask Choose Mask created previously. Apply and Save

Then use the C.O.M file in IDL to calculate the C.O.M. and the sums. Import into excel and figure out the equivalent pixel to mm conversion. Remember that the value given is left to right and top to bottom so will need to subtract the value from the diameter of the pipe.

Version 2.0: Automated Image Processing

Once the manual processing method showed satisfactory results the process was coded in IDL (shown at the end of this appendix). This allowed for batch processing of the images and greatly simplified the calculation of the center of mass of each image. The IDL code imports the specified images, determines the largest y dimension and then uses this to normalize the x dimension. The code then computes the amount of stretch required in both the x and y dimensions to correct for the viewing angle distortion of the image. The image is then rotated 90 degrees to correct for camera mounting. The region of interest still needs to be applied manually to allow for a best judgement call on how much of the laser artifact to remove during the cropping operation.

Centre of Mass Proof of Concept Test

To test the centre of mass code I created an image file that was completely white and 501x501 pixels wide. The image was run through the C.o.M. code. There should be 250 pixels on either side of the center pixel. Since the first pixel is zero the actual center pixel will be indexed as 250 (i.e. 250 + center pixel + 250=501).

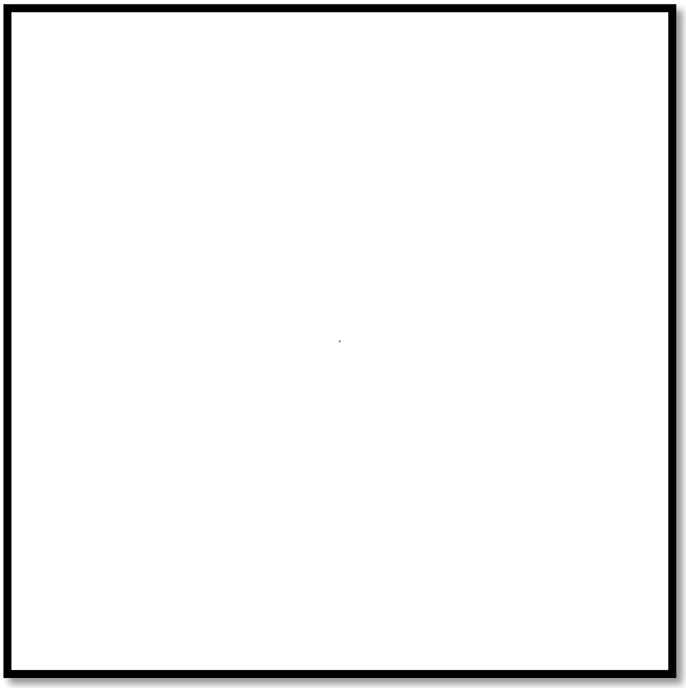

Figure C-1: Initial C.o.M. Test image

Blank white image with a single black center pixel. Black border added for visualization but was not included during the test.

Results obtained were:

```
CG XPosition
         250
CG YPosition
         250
Sum
       64005000.
Sum / 1000
       64005.000
```

Then I cropped said image randomly to obtain this.

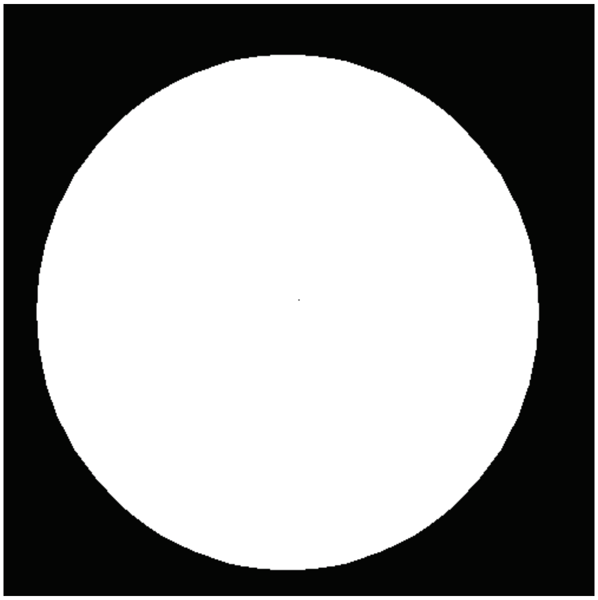

Figure C-2: Cropped C.o.M. test image

When I ran it through the C.o.M. IDL program I obtained the following results

```
% Compiled module: CENTRE_OF_MASS_THESIS.
CG XPosition
         240
CG YPosition
         260
Sum
       37182060.
Sum / 1000
       37182.060
```

Which makes sense as the crop shifted the white image to the left (therefore centre of gravity X is now 240) and down (centre of gravity Y is now 260). But the take away is the center is still referenced to the original image size. The center is 260 pixels down from the top of the original image.

The solution was to manually determine the top pixel of the mask and the bottom pixel of the mask (or left and right if the CG X is needed). Then use this and the known inner dimensions of the pipe to normalize

For the trial image above this equals 44 and 479 in the y-axis and 29 and 454 in the x-axis. If I assume an inner dimension of 50 mm (this is a manufactured image so this calculation is for demonstration purposes only) the following example calculation will eventually give the centroids y position in mm from the bottom example tubing.

y-axis

Image Y Size: 479 px-44px=435px

Pixels per mm: 435px/50mm=8.7px/mm

Adjusted Centroid: 260-44=216px -this gives the centroid location from the top of the masked image

Realigned Centroid: 435px-216px=219px -Subtracted centroid from Image Y size to give the dimension from the bottom of the image

Height in mm from bottom of pipe: 219px/8.7px/mm=25.17mm

Appendix D: Sensor Location Schematic

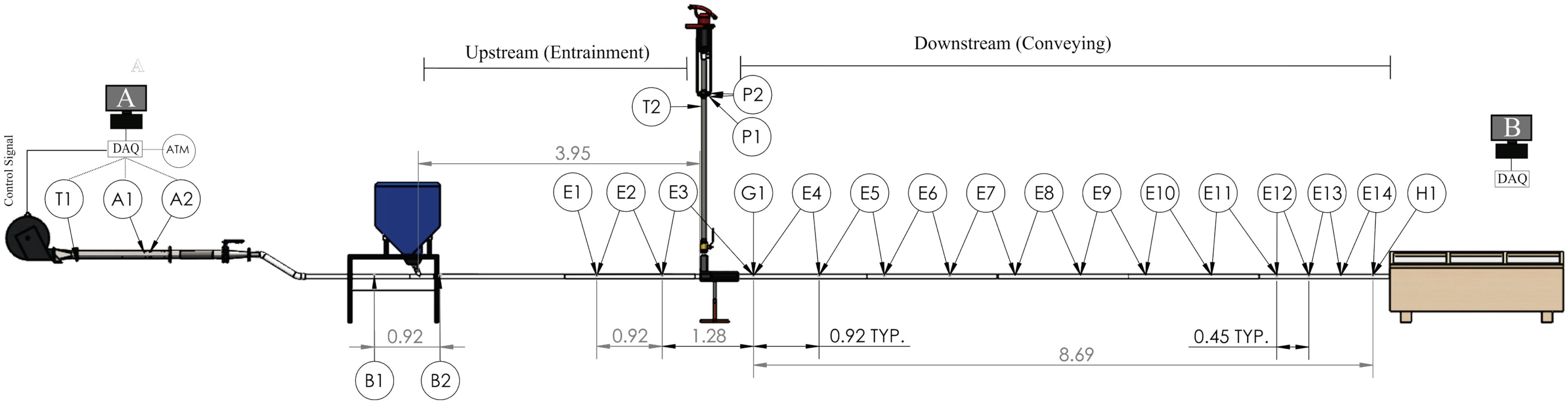

Figure D-1: Schematic of sensor and data acquisition (DAQ) locations. Showing upstream and downstream conveying sections of the system. Typical spacing listed in metres.

Appendix E: Sensors and Calibration

To measure pressure in the air handling lab a combination of Dwyer 616 and 648 differential pressure sensors were used. These sensors had a 4 to 20 mA current output. The reason for two different sensor series is due to the 616 being discontinued halfway through the project and was replaced with the 648. Both sensors have similar ranges and accuracy with the main difference being a manual zero and span on the 616 which was replaced by an automatic zeroing routine on the 648 (the span can still be adjusted manually if required).

To confirm the sensor accuracy, zero, and span a Druck DPI 605 Pressure Calibrator was used. A syringe was used to apply a static pressure to both the Druck and the sensor being calibrated. The calibration procedure is as follows.

1. Sensor and Druck are open to atmospheric pressure. The sensor is zeroed either manually or with the automatic routine depending on the sensor.
2. System is carefully pressurised using a syringe to the maximum range of the sensor. The sensor is compared to the reading on the Druck and manually spanned if needed.
3. Return the system to atmospheric pressure. Zero again if needed.
4. Complete steps 2 and 3 until satisfied with the sensor calibration.

Figure D-2 and Figure D-3 are the manufacturer (Dwyer) supplied specification sheets for the two differential pressure transducers used in this work.

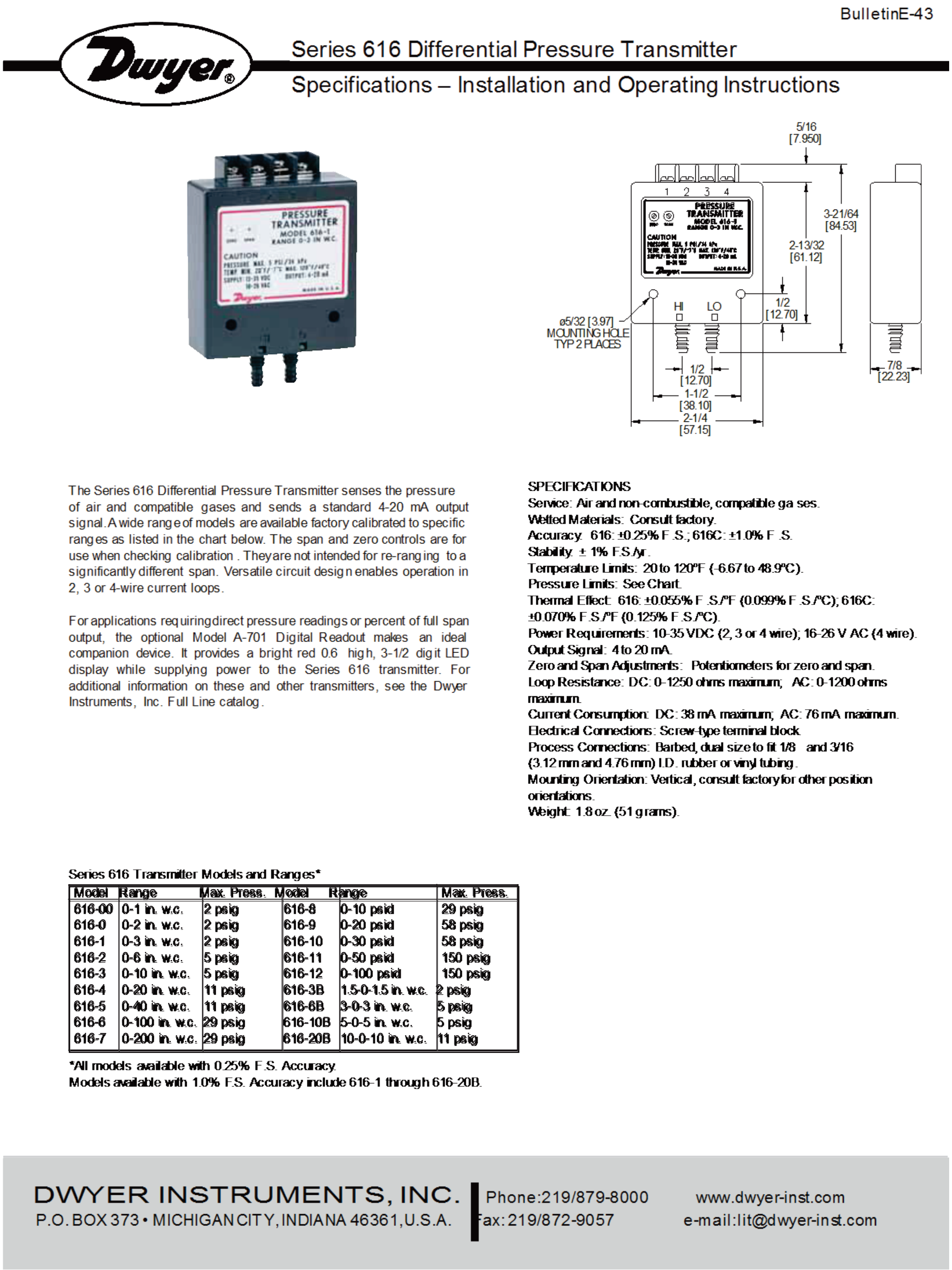

Bulletin E-43

Series 616 Differential Pressure Transmitter

Specifications – Installation and Operating Instructions

The Series 616 Differential Pressure Transmitter senses the pressure of air and compatible gases and sends a standard 4-20 mA output signal. A wide range of models are available factory calibrated to specific ranges as listed in the chart below. The span and zero controls are for use when checking calibration. They are not intended for re-ranging to a significantly different span. Versatile circuit design enables operation in 2, 3 or 4-wire current loops.

For applications requiring direct pressure readings or percent of full span output, the optional Model A-701 Digital Readout makes an ideal companion device. It provides a bright red 0.6 high, 3-1/2 digit LED display while supplying power to the Series 616 transmitter. For additional information on these and other transmitters, see the Dwyer Instruments, Inc. Full Line catalog.

SPECIFICATIONS

Service: Air and non-combustible, compatible gases.
Wetted Materials: Consult factory.
Accuracy: 616: ±0.25% F.S.; 616C: ±1.0% F.S.
Stability: ± 1% F.S./yr.
Temperature Limits: 20 to 120°F (-6.67 to 48.9°C).
Pressure Limits: See Chart.
Thermal Effect: 616: ±0.055% F.S./°F (0.099% F.S./°C); 616C: ±0.070% F.S./°F (0.125% F.S./°C).
Power Requirements: 10-35 VDC (2, 3 or 4 wire); 16-26 V AC (4 wire).
Output Signal: 4 to 20 mA.
Zero and Span Adjustments: Potentiometers for zero and span.
Loop Resistance: DC: 0-1250 ohms maximum; AC: 0-1200 ohms maximum.
Current Consumption: DC: 38 mA maximum; AC: 76 mA maximum.
Electrical Connections: Screw-type terminal block.
Process Connections: Barbed, dual size to fit 1/8 and 3/16 (3.12 mm and 4.76 mm) I.D. rubber or vinyl tubing.
Mounting Orientation: Vertical, consult factory for other position orientations.
Weight: 1.8 oz. (51 grams).

Series 616 Transmitter Models and Ranges*

Model	Range	Max. Press.	Model	Range	Max. Press.
616-00	0-1 in. w.c.	2 psig	616-8	0-10 psid	29 psig
616-0	0-2 in. w.c.	2 psig	616-9	0-20 psid	58 psig
616-1	0-3 in. w.c.	2 psig	616-10	0-30 psid	58 psig
616-2	0-6 in. w.c.	5 psig	616-11	0-50 psid	150 psig
616-3	0-10 in. w.c.	5 psig	616-12	0-100 psid	150 psig
616-4	0-20 in. w.c.	11 psig	616-3B	1.5-0-1.5 in. w.c.	2 psig
616-5	0-40 in. w.c.	11 psig	616-6B	3-0-3 in. w.c.	5 psig
616-6	0-100 in. w.c.	29 psig	616-10B	5-0-5 in. w.c.	5 psig
616-7	0-200 in. w.c.	29 psig	616-20B	10-0-10 in. w.c.	11 psig

*All models available with 0.25% F.S. Accuracy.
Models available with 1.0% F.S. Accuracy include 616-1 through 616-20B.

DWYER INSTRUMENTS, INC.
P.O. BOX 373 • MICHIGAN CITY, INDIANA 46361, U.S.A.
Phone: 219/879-8000
Fax: 219/872-9057
www.dwyer-inst.com
e-mail: lit@dwyer-inst.com

Figure D-2: Dwyer 616 Differential Pressure Transducer

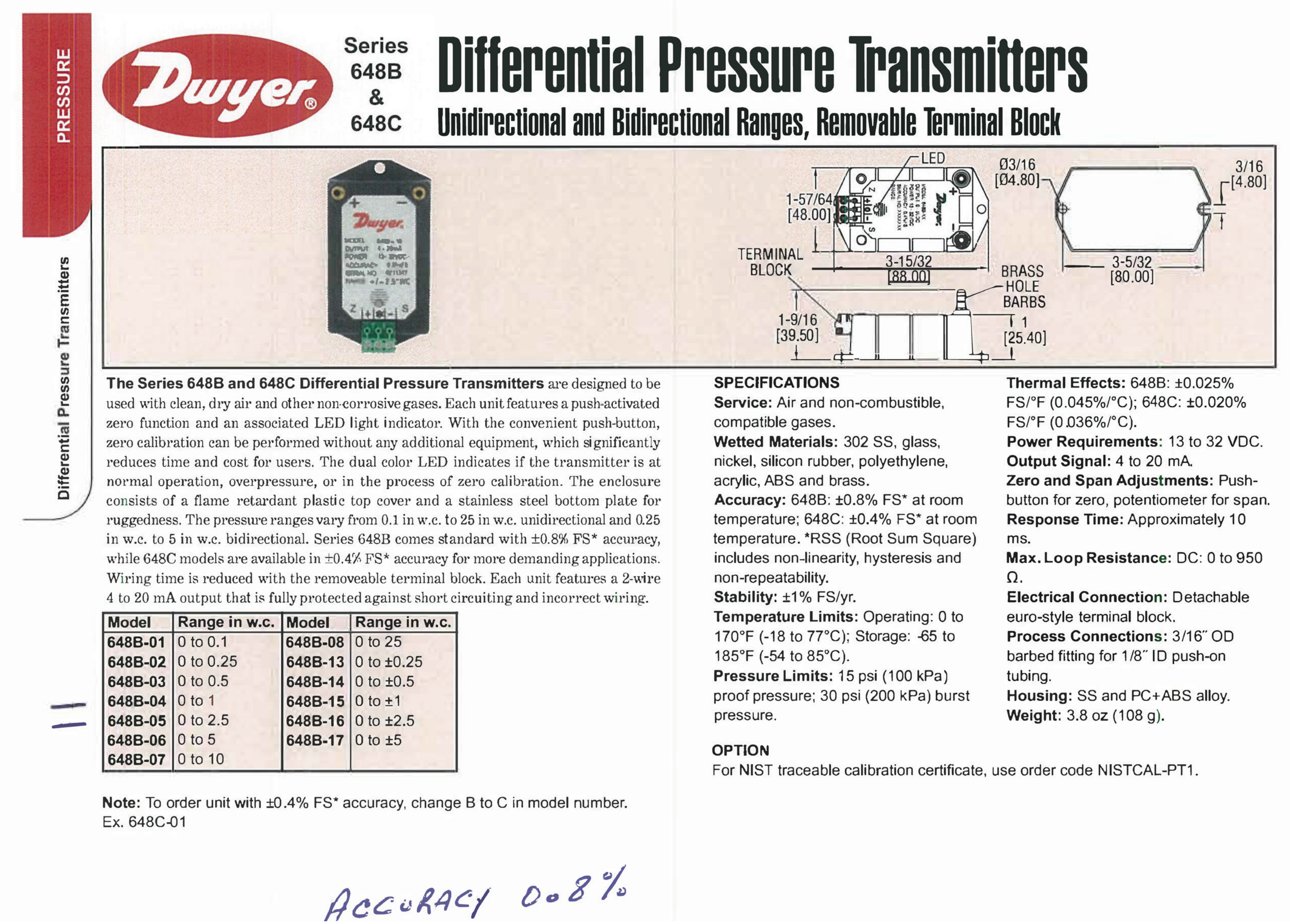

PRESSURE

Differential Pressure Transmitters

Dwyer®

Series
648B
&
648C

Differential Pressure Transmitters

Unidirectional and Bidirectional Ranges, Removable Terminal Block

The Series 648B and 648C Differential Pressure Transmitters are designed to be used with clean, dry air and other non-corrosive gases. Each unit features a push-activated zero function and an associated LED light indicator. With the convenient push-button, zero calibration can be performed without any additional equipment, which significantly reduces time and cost for users. The dual color LED indicates if the transmitter is at normal operation, overpressure, or in the process of zero calibration. The enclosure consists of a flame retardant plastic top cover and a stainless steel bottom plate for ruggedness. The pressure ranges vary from 0.1 in w.c. to 25 in w.c. unidirectional and 0.25 in w.c. to 5 in w.c. bidirectional. Series 648B comes standard with ±0.8% FS* accuracy, while 648C models are available in ±0.4% FS* accuracy for more demanding applications. Wiring time is reduced with the removeable terminal block. Each unit features a 2-wire 4 to 20 mA output that is fully protected against short circuiting and incorrect wiring.

Model	Range in w.c.	Model	Range in w.c.
648B-01	0 to 0.1	**648B-08**	0 to 25
648B-02	0 to 0.25	**648B-13**	0 to ±0.25
648B-03	0 to 0.5	**648B-14**	0 to ±0.5
648B-04	0 to 1	**648B-15**	0 to ±1
648B-05	0 to 2.5	**648B-16**	0 to ±2.5
648B-06	0 to 5	**648B-17**	0 to ±5
648B-07	0 to 10		

Note: To order unit with ±0.4% FS* accuracy, change B to C in model number.
Ex. 648C-01

SPECIFICATIONS

Service: Air and non-combustible, compatible gases.

Wetted Materials: 302 SS, glass, nickel, silicon rubber, polyethylene, acrylic, ABS and brass.

Accuracy: 648B: ±0.8% FS* at room temperature; 648C: ±0.4% FS* at room temperature. *RSS (Root Sum Square) includes non-linearity, hysteresis and non-repeatability.

Stability: ±1% FS/yr.

Temperature Limits: Operating: 0 to 170°F (-18 to 77°C); Storage: -65 to 185°F (-54 to 85°C).

Pressure Limits: 15 psi (100 kPa) proof pressure; 30 psi (200 kPa) burst pressure.

Thermal Effects: 648B: ±0.025% FS/°F (0.045%/°C); 648C: ±0.020% FS/°F (0.036%/°C).

Power Requirements: 13 to 32 VDC.

Output Signal: 4 to 20 mA.

Zero and Span Adjustments: Push-button for zero, potentiometer for span.

Response Time: Approximately 10 ms.

Max. Loop Resistance: DC: 0 to 950 Ω.

Electrical Connection: Detachable euro-style terminal block.

Process Connections: 3/16″ OD barbed fitting for 1/8″ ID push-on tubing.

Housing: SS and PC+ABS alloy.

Weight: 3.8 oz (108 g).

OPTION

For NIST traceable calibration certificate, use order code NISTCAL-PT1.

ACCURACY 0.8%

Figure D-3: Dwyer 616-C Differential Pressure Transducer

Figure D-4 and Figure D-5 show the Druck Pressure Calibrator in use. Additionally, the pressure sensors in the downstream conveying section can be seen in Figure D-4.

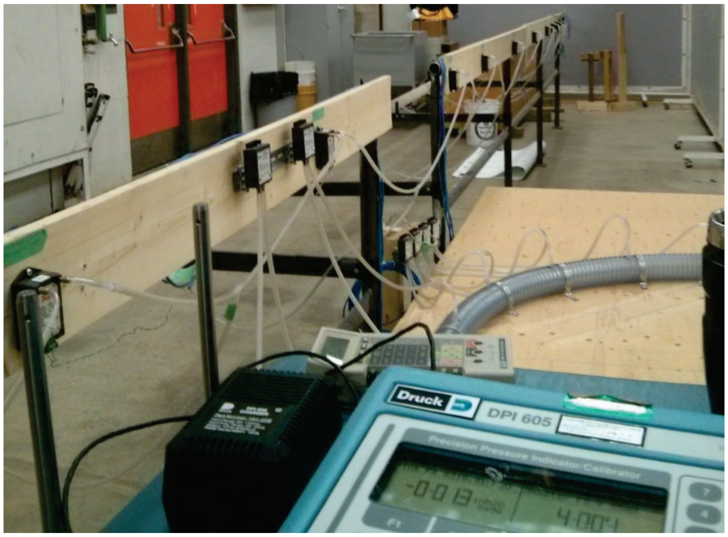

Figure D-4: Druck Pressure Calibrator with the differential pressure sensors in the background.

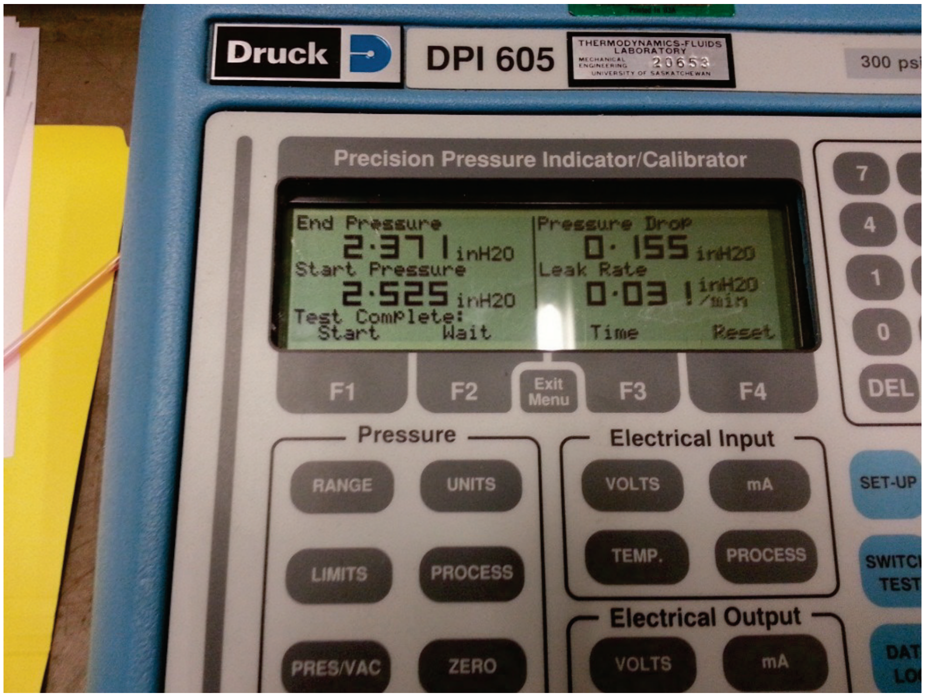

Figure D-5: Druck Pressure Calibrator in use.

Table D-1 is a schematic of the laboratory wiring for data acquisition and control. DIN rail mounted wiring blocks and components were used and each table line indicates a wiring layer as seen facing the wiring cabinet.

Table D-1: Wiring Schematic for the data acquisition and control cabinet.

Rail 1: Sensor Inputs			
In	**Description**	**Out**	**DAQ Channel**
Orange	A1 sensor	Red	daqmod1-p0
Orange/White	power	Red	
Green	A2 sensor	Green	daqmod1-p1
Green/White	power	Red	
Green	B1 sensor	White	daqmod1-p2
Green/White	power	Red	
Orange	B2 sensor	Red	daqmod1-p3
Orange/White	power	Red	
Green	C1 sensor	Green	
Black	power	Red	
Yellow	C2 sensor	Yellow	
Black	power	Red	
Yellow	D1 sensor	Blue	
Black	power	Red	
Shielding	ground	NC	
Orange	D2 sensor	Yellow	
Black	power	Red	
~~Blue~~	~~D3 sensor~~	~~Blue~~	
Black	power	Red	
Green	E1 sensor	Blue	daqmod1-p4
Green/White	power	Red	
Orange	E2 sensor	Green	daqmod1-p5
Orange/White	power	Red	
Green	E3 sensor	Brown	daqmod1-p6
Green/White	power	Red	
Orange	E4 sensor	Red	daqmod1-p7
Orange/White	power	Red	
Green	E5 sensor	White	daqmod2-p0
Green/White	power	Red	
Orange	E6 sensor	Orange	daqmod2-p1
Orange/White	power	Red	
	ground	NC	
Green	E7 sensor	Green	daqmod2-p2
Green/White	power	Red	
Orange	E8 sensor	Black	daqmod2-p3
Orange/White	power	Red	
Green	E9 sensor	Brown	daqmod2-p4
Green/White	power	Red	
Orange	E10 sensor	Blue	daqmod2-p5

Rail 2: External Controls and Patch Bay(Sensors E-F)			
In		**Description**	**Out**
1k Resistor		Power in for Manual Control	Ref
		Power to Manual Control Pot	Orange
Red		Control Switch to AMM	Purple
Red		AMM to Local Kill Switch	Black
Green		Local to Remote Kill Switch	Black
Green/White		Kill Switch to Signal Out	NC
Orange/White			NC
Orange		Sig Return to Common	White
NC		Gnd for Shielding	NC
		Holder	
	Patch Bay*		
	Port	Sensor	
Green	1	E1 sensor	Green
Green/White		power	Green/White
Orange		E2 sensor	Orange
Orange/White		power	Orange/White
Green	2	E3 sensor	Green
Green/White		power	Green/White
Orange		E4 sensor	Orange
Orange/White		power	Orange/White
Green	3	E5 sensor	Green
Green/White		power	Green/White
Orange		E6 sensor	Orange
Orange/White		power	Orange/White
Green	4	E7 sensor	Green
Green/White		power	Green/White
Orange		E8 sensor	Orange
Orange/White		power	Orange/White
Green	5	E9 sensor	Green
Green/White		power	Green/White
Orange		E10 sensor	Orange
Orange/White		power	Orange/White
Green	6	E11 sensor	Green
Green/White		power	Green/White
Orange		E12 sensor	Orange
Orange/White		power	Orange/White

Orange/White	power	Red	
Green	E11 sensor	Green	daqmod2-p6
Green/White	power	Red	
Orange	E12 sensor	White	daqmod2-p7
Orange/White	power	Red	
Green	E13 sensor	Orange	daqmod3-p0
Green/White	power	Red	
Orange	E14 sensor	Black	daqmod3-p1
Orange/White	power	Red	
	ground	NC	
Green	E15 sensor	Brown	daqmod3-p2
Green/White	power	Red	
Green	F1 sensor	Blue	daqmod3-p3
Green/White	power	Red	
Orange	F2 sensor	White	daqmod3-p4
Orange/White	power	Red	
Blue	F3 sensor	Orange	daqmod3-p5
Blue/White	power	Red	
Brown	F4 sensor	Green	daqmod3-p6
Brown/White	power	Red	
Green	F5 sensor	Black	daqmod4-p0
Green/White	power	Red	
Orange	F6 sensor	White	daqmod4-p1
Orange/White	power	Red	
Blue	F7 sensor	Blue	daqmod4-p2
Blue/White	power	Red	
Brown	F8 sensor	Orange	daqmod4-p3
Brown/White	power	Red	
Green	F9 sensor	Black	daqmod4-p4
Green/White	power	Red	
Orange	F10 sensor	Blue	daqmod4-p5
Orange/White	power	Red	
Blue	F11 sensor	Green	daqmod4-p6
Blue/White	power	Red	
Brown	F12 sensor	Blue	daqmod4-p7
Brown/White	power	Red	
Spare	Spare	Spare	Spare

Green	7	E13 sensor	Green
Green/White		power	Green/White
Orange		E14 sensor	Orange
Orange/White		power	Orange/White
Green	8	E15 sensor	Green
Green/White		power	Green/White
Green	9	F1 sensor	Green
Green/White		power	Green/White
Orange		F2 sensor	Orange
Orange/White		power	Orange/White
Blue		F3 sensor	Blue
Blue/White		power	Blue/White
Brown		F4 sensor	Brown
Brown/White		power	Brown/White
Green	10	F5 sensor	Green
Green/White		power	Green/White
Orange		F6 sensor	Orange
Orange/White		power	Orange/White
Blue		F7 sensor	Blue
Blue/White		power	Blue/White
Brown		F8 sensor	Brown
Brown/White		power	Brown/White
Green	11	F9 sensor	Green
Green/White		power	Green/White
Orange		F10 sensor	Orange
Orange/White		power	Orange/White
Blue		F11 sensor	Blue
Blue/White		power	Blue/White
Brown		F12 sensor	Brown
Brown/White		power	Brown/White
Green	12	B1 sensor	Green
Green/White		power	Green/White
Orange		B2 sensor	Orange
Orange/White		power	Orange/White
Blue		Spare**	Blue
Blue/White			Blue/White
Brown			Brown
Brown/White			Brown/White

Rail 3: Power		
In	**Description**	**Out**
	24 V Power Rail	
	Power Common Rail	
	10 V Regulator	
	10V Rail	
	10V Return	

Appendix F: Specific Pressure Drop and Velocity Ratio Testing Set Points

Table F-1 is the full outline of the test conditions analyzed in Chapter 5.

Table F-1: Specific Pressure Drop and Velocity Ratio Testing Set Points. Full Table

Upstream Velocity (m/s)	Downstream Velocity (m/s)	Velocity Ratio	μ at 0.0205 kg/s	μ at 0.0620 kg/s	μ at 0.1020 kg/s
30	30	1.00	0.22	0.66	1.09
	29	0.97	0.23	0.69	1.13
	28	0.93	0.24	0.71	1.17
	27	0.90	0.24	0.74	1.21
	26	0.87	0.25	0.77	1.26
	25	0.83	0.26	0.80	1.31
	24	0.80	0.27	0.83	1.37
	23	0.77	0.29	0.87	1.43
	22	0.73	0.30	0.91	1.49
	21	0.70	0.31	0.95	1.56
	20	0.67	0.33	1.00	1.64
	19	0.63	0.35	1.05	1.73
	18	0.60	0.37	1.11	1.82
	17	0.57	0.39	1.17	1.93
	16	0.53	0.41	1.25	2.05
	15	0.50	0.44	1.33	2.19
	14	0.47	0.47	1.42	2.34
	13	0.43	0.51	1.53	2.52
	12	0.40	0.55	1.66	2.73
	11	0.37	0.60	1.81	2.98
	10	0.33	0.66	1.99	3.28
25	25	1.00	0.26	0.80	1.31
	24	0.96	0.27	0.83	1.37
	23	0.92	0.29	0.87	1.43
	22	0.88	0.30	0.91	1.49
	21	0.84	0.31	0.95	1.56
	20	0.80	0.33	1.00	1.64
	19	0.76	0.35	1.05	1.73
	18	0.72	0.37	1.11	1.82
	17	0.68	0.39	1.17	1.93
	16	0.64	0.41	1.25	2.05
	15	0.60	0.44	1.33	2.19
	14	0.56	0.47	1.42	2.34
	13	0.52	0.51	1.53	2.52
	12	0.48	0.55	1.66	2.73
	11	0.44	0.60	1.81	2.98
	10	0.40	0.66	1.99	3.28
	9	0.36	0.73	2.21	3.64
	8	0.32	0.82	2.49	4.10
	7	0.28	0.94	2.85	4.69
	6	0.24	1.10	3.32	5.47

Upstream Velocity (m/s)	Downstream Velocity (m/s)	Velocity Ratio	μ at 0.0205 kg/s	μ at 0.0620 kg/s	μ at 0.1020 kg/s
20	20	1.00	0.33	1.00	1.64
	19	0.95	0.35	1.05	1.73
	18	0.90	0.37	1.11	1.82
	17	0.85	0.39	1.17	1.93
	16	0.80	0.41	1.25	2.05
	15	0.75	0.44	1.33	2.19
	14	0.70	0.47	1.42	2.34
	13	0.65	0.51	1.53	2.52
	12	0.60	0.55	1.66	2.73
	11	0.55	0.60	1.81	2.98
	10	0.50	0.66	1.99	3.28
	9	0.45	0.73	2.21	3.64
	8	0.40	0.82	2.49	4.10
	7	0.35	0.94	2.85	4.69
	6	0.30	1.10	3.32	5.47
18	18	1.00	0.37	1.11	1.82
	17	0.94	0.39	1.17	1.93
	16	0.89	0.41	1.25	2.05
	15	0.83	0.44	1.33	2.19
	14	0.78	0.47	1.42	2.34
	13	0.72	0.51	1.53	2.52
	12	0.67	0.55	1.66	2.73
	11	0.61	0.60	1.81	2.98
	10	0.56	0.66	1.99	3.28
	9	0.50	0.73	2.21	3.64
	8	0.44	0.82	2.49	4.10
	7	0.39	0.94	2.85	4.69
	6	0.33	1.10	3.32	5.47
16	16	1.00	0.41	1.25	2.05
	15	0.94	0.44	1.33	2.19
	14	0.88	0.47	1.42	2.34
	13	0.81	0.51	1.53	2.52
	12	0.75	0.55	1.66	2.73
	11	0.69	0.60	1.81	2.98
	10	0.63	0.66	1.99	3.28
	9	0.56	0.73	2.21	3.64
	8	0.50	0.82	2.49	4.10
	7	0.44	0.94	2.85	4.69
	6	0.38	1.10	3.32	5.47
14	14	1.00	0.47	1.42	2.34
	13	0.93	0.51	1.53	2.52
	12	0.86	0.55	1.66	2.73
	11	0.79	0.60	1.81	2.98
	10	0.71	0.66	1.99	3.28
	9	0.64	0.73	2.21	3.64
	8	0.57	0.82	2.49	4.10
	7	0.50	0.94	2.85	4.69
	6	0.43	1.10	3.32	5.47

Upstream Velocity (m/s)	Downstream Velocity (m/s)	Velocity Ratio	μ at 0.0205 kg/s	μ at 0.0620 kg/s	μ at 0.1020 kg/s
12	12	1.00	0.55	1.66	2.73
	11	0.92	0.60	1.81	2.98
	10	0.83	0.66	1.99	3.28
	9	0.75	0.73	2.21	3.64
	8	0.67	0.82	2.49	4.10
	7	0.58	0.94	2.85	4.69
	6	0.50	1.10	3.32	5.47
10	10	1.00	0.66	1.99	3.28
	9	0.90	0.73	2.21	3.64
	8	0.80	0.82	2.49	4.10
	7	0.70	0.94	2.85	4.69

Appendix G: Specific Energy vs. Upstream Set Velocity. All Trials

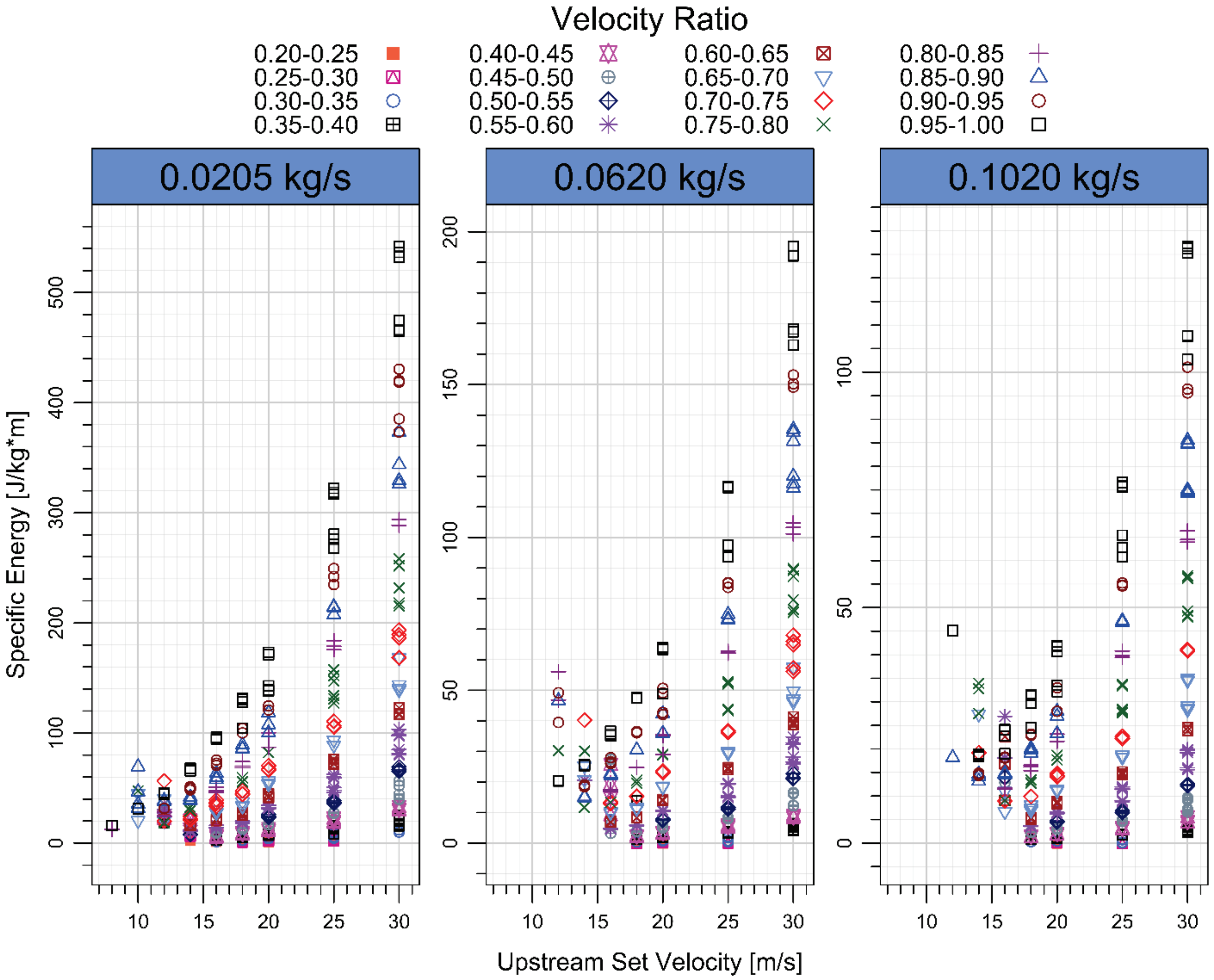

Figure G-1: Average specific energy plotted by upstream air velocity. Each panel is a plot of a different mass flow rate (set meter roller RPM of 10, 30, and 50 from left to right respectively). All Trials